ENGINEERING SENSITIVITY: AN OPTICAL OPTIMIZATION OF RING RESONATOR ARRAYS FOR LABEL-FREE WHOLE BACTERIAL SENSING

by

Justin C. Wirth

A Dissertation

Submitted to the Faculty of Purdue University

In Partial Fulfillment of the Requirements for the degree of

Doctor of Philosophy

School of Electrical & Computer Engineering

West Lafayette, Indiana

December 2019

THE PURDUE UNIVERSITY GRADUATE SCHOOL
STATEMENT OF COMMITTEE APPROVAL

Dr. Minghao Qi, Chair

Department of Electrical and Computer Engineering

Dr. Peter Bermel

Department of Electrical and Computer Engineering

Dr. Alexandra Boltasseva

Department of Electrical and Computer Engineering

Dr. Andrew M. Weiner

Department of Electrical and Computer Engineering

Dr. Yi Xuan

Department of Electrical and Computer Engineering

Approved by:

Dr. Pedro Irazoqui

Dedicated to my loving wife and family.

ACKNOWLEDGMENTS

The author would like to thank Prof. Minghao Qi and Prof. Andrew Weiner for teaching, discussion, and guidance throughout his time here at Purdue. Further thanks go to Prof. Peter Bermel, Prof. Alexandra Boltasseva, and Prof. Yi Xuan for their helpful suggestions and advising as committee members. Group members in Prof. Qi's group have been significantly helpful to the efforts subsequently described. Many thanks go to both Prof. Yi Xuan and Dr. Kyunghun Han, who fabricated the SOI microrings measured in the cellular simulant chapter and provided much useful discussion and fabrication assistance before and afterwards. Dr. Ben Niu performed ellipsometry for ma-N, provided Matlab layout generation code that was modified by the author to generate all EBL layouts, and provided helpful discussion with respect to attempts at removing HSQ cellular simulants. Thanks go to the staff of the Birck Nanotechnology Center, and particularly Bill Rowe, Dan Hosler, and Sean Rinehart for helpful discussions on fabrication, and Joon Park and Dr. Tim Kwok for discussions on cells and biosensing.

Many thanks go to the collaborators at AFRL/RY, and especially the principal investigator, Dr. Brett Wenner. Additional thanks go to Drs. Monica S. Allen and Jeffery W. Allen, who provided direction and many helpful discussions, particularly regarding COMSOL Multiphysics. Dr. Jeffery Allen also provided the tools to 3D print the grating coupler mounting arm. Thanks also go to Dr. Camilla Mauzy (AFRL/RHDJ) for providing the *E. Coli* cells used in the experimental proof of concept, along with values for the initial cellular concentration.

The author is thankful for the funding support through AFOSR Lab Task 13RY12COR (PO: Dr. Hugh De Long). He also acknowledges support from the Air Force Research Laboratory (AFRL/RY), through the Advanced Materials, Manufacturing and Testing Information Analysis Center (AMMTIAC) contract with Alion Science and Technology Contract FA4600-06-D-0003 DO#0048, and Defense Threat Reduction Agency grant HDTRA1-10-1-0106.

PREFACE

The work contained herein was a collaboration between the author as a member of Prof. Qi's research group, and the Air Force Research Laboratory Sensors Directorate (AFRL/RY) at Wright-Patterson Air Force Base near Dayton, OH. The overall goal was to explore microcavity resonators for the detection of biological cells, and to:
"*develop theoretical models, fabrication processes, and characterization techniques to demonstrate microcavity resonators for a chemical/biological sensing platform that is: (i) sensitive, (ii) selective, (iii) robust, (iv) amenable to multiplexing (i.e., multiple analyte) sensing, and (v) adaptable to a variety of sensing applications*."

The goals of sensitivity, multiplexing, and adaptability were chosen as the high-level motivation and focus for this work, as they can be provided by the ring resonator itself as an optical sensing element.

Simulation and experimental characterization were done by the author on site at AFRL, with fabrication taking place at Purdue's Birck Nanotechnology Center and occasionally by the author at the Notre Dame Nanofabrication Facility. With notable exclusions presented in the Acknowledgements, the author has developed/performed the totality of work described herein, including: theoretical framework, simulations, EBL fabrication and AFM/SEM characterization of cellular simulants, layout of SOI rings, design and simulation of SOI grating couplers (partially and fully etched), assisted/guided selection of and performed setup of NIR fiber characterization equipment, and fabrication of SOI devices for theoretical proof of concept experiments.

TABLE OF CONTENTS

LIST OF TABLES

LIST OF FIGURES

ABSTRACT

The quick, reliable, and sensitive detection of bacterial contamination is desired in areas such as counter bioterrorism, medicine, and food/water safety as pathogens such as *E. coli* can cause harmful effects with the presence of just a few cells. However, standard high sensitivity techniques require laboratories and trained technicians, requiring significant time and expense. More desirable would be a sensitive point-of-care device that could detect an array of pathogens without sample pre-treatment, or a continuous monitoring device operating without the need for frequent operator intervention.

Optical microring resonators in silicon photonic platforms are particularly promising as scalable, multiplexed refractive index sensors for an integrated biosensing array. However, no systematic effort has been made to optimize the sensitivity of microrings for the detection of relatively large discrete analytes such as bacteria, which differs from the commonly considered cases of fluid or molecular sensitivity. This work demonstrates the feasibility of using high finesse microrings to detect whole bacterial cells with single cell resolution over a full range of potential analyte-to-sensor binding scenarios. Sensitivity parameters describing the case of discrete analyte detection are derived and used to guide computational optimization of microrings and their constituent waveguides, after considering a range of parameters such as waveguide dimension, material, modal polarization, and ring radius. The sensitivity of the optimized 2.5 μm radius silicon TM O-band ring is experimentally demonstrated with photoresist cellular simulants. A multiplexed optimized ring array is then shown to detect *E. Coli* cells in an experimental proof of concept.

1. INTRODUCTION

1.1. Sensing of bacterial pathogens

The contamination of food or liquids by, or the exposure of humans or livestock to, unwanted bacteria is a real and present threat even in modern life. For example, in 2018, two nationwide outbreaks of *Escherichia coli* O157:H7 associated with romaine lettuce led to 269 cases, 119 hospitalizations, and 5 deaths across 42 states [1] [2]. The presence of *E. coli* in drinking water is characteristic of fecal contamination, which carries significant health risks [3]. The spread of MRSA and other increasingly antibiotic resistant bacteria in hospitals is a growing concern [4]. Anthrax (*bacillus anthracis*) can be inhaled with high chance of mortality, leading to a concern over potential bioterrorism in the wake of numerous mailings in 2001 [5]. And even in non-pathogenic cases, unwanted growth of bacteria can have significantly negative effects. *Psuedomonas aurigenosa* is one of hundreds of bacteria that can grow in jet fuel, leading to decay and failure of plastic, rubber, and metal aircraft fuel line components [6].

However, current techniques for identifying the presence of bacteria take significant time, money, human effort, or large amounts of analytes. Standard lab techniques such as enzyme-linked immunosorbent assay (ELISA), and the more sensitive polymerase chain reaction (PCR) can take hours for trained technicians operating in a lab environment, or weeks if samples must be sent off, and still require thousands of bacteria per mL [7]. Commercial surface plasmon resonance (SPR) based sensors can be compact and inexpensive but require large quantities of bacteria for detection [8]. Many research stage sensitive techniques require multiple chemical processing steps to label the analytes, resulting in sensitivity but still requiring significant time and human effort [8]. It would be much more desirable to have a sensitive point-of-care device that could detect an array of bacteria without sample pre-treatment, or a continuous monitoring device operating without the need for frequent operator intervention.

1.2. Microring resonators as sensors

Microcavity resonators offer the ability to confine near infrared (NIR) light in a small area, and the low loss achievable by dielectric waveguides such as silicon (Si) or silicon nitride (SiN) on

silicon dioxide (SiO_2) substrates leads to very high quality (Q) factors and narrow resonance line widths [9] [10] [11] [12] [13] [14]. In particular, microring resonators allow for a small footprint, easy fabrication, and relatively simple designs [9] [12] [15]. These structures are used in a variety of applications, including many optical devices that previously required large bulk optical setups [9]. While predominantly designed to have a tight confinement of light to minimize propagation loss and work at a polarization that matches the waveguide geometry [10] [16] [17] [18] [19] [20], with mild tweaking, microrings can be designed to operate with less well confined resonant modes and still retain their low loss characteristics. This mode delocalization, combined with the narrow line width and high environmental sensitivity of the microcavity, can be utilized for refractive index difference based sensing [21] [22] [23]. Baseline behavior of the resonator is measured and then compared to the behavior of the cavity when an object with a different refractive index is introduced near the cavity. For ring resonators, this object will cause a shift in the effective mode index, and consequently change the resonant wavelength of the cavity. Compared to other travelling wave resonator geometries [24], microrings are commonly regarded as the most suitable candidates for low-cost lab-on-chip sensing platforms [25] as they offer highly scalable and integrated designs. Additionally, they can be mass produced on conventional foundry production lines and use relatively low optical powers.

Ring resonators have been explored for the detection [16] [17] [18] [19] [20] [21] [25] [26] [27] [28] [29] [30] of refractive index changes in a cladding liquid and sensing the concentration of proteins, antibodies, and other biomolecules bound to a microring. Many of these demonstrations use rings from the start-up company Genalyte, which was founded in 2007 and has raised more than $90 million in funding since [31]. Bulk liquid refractive index sensing [19], evanescent field characterization and detection of saturated molecular monolayers [27], multiplexed molecular detection [29], and multiplexed immunoassays [30] have all been demonstrated on the Genalyte "Maverick" platform, or on chip components that go into the Maverick platform. The backbone of the platform is a 4 mm by 6 mm silicon chip with 136 silicon microrings, 15 μm in radius [30], with waveguides 200 nm x 500 nm [32]. The rings operate in the C-band (1560 nm) at the TE mode, which give a 1/*e* electric field intensity of 52 nm [32]. Each chip is divided into 32 clusters of 4 rings multiplexed onto a single waveguide in an all-pass fashion [30]. The chips are coated with a fluoropolymer 1-2 μm thick, and windows on 128 rings on each chip are opened, with 8

remaining covered as thermal controls [30]. Measurement is done by an external cavity diode laser, which is swept across the 32 input-couplers (grating couplers) with 250 ms time resolution [32]. The laser performs a 12 nm wavelength sweep (approximately one free spectral range) around 1560 nm to measure the 4 resonances of each 4-ring array [32]. The results of each 4-ring array are then averaged, and outliers of more than 3 standard deviations removed [30]. An on-chip Fabry-Perot etalon is used as a wavelength reference to give a 0.1 pm noise floor, as the majority of noise in such a setup is due to wavelength uncertainty in the input laser [30] [32]. The meaningful signal output is the rate of change of the resonance peaks during the transition period between the start of analyte binding (or change in cladding index) and saturation, which is used to correlate to a particular analyte concentration (or cladding index change) [33].

These chips have been used by a number of researchers for research scale applications [19] [27] [29] [32] of cladding sensing. An integrated setup designed for point-of-care blood testing is also being pursued, though the Maverick platform is not (as of June 25, 2018 [34]) FDA approved for specific tests. This consists of 12 chips, with each 4-ring array functionalized (through the native oxide on silicon) by an automated spotter towards particular analytes of interest [30].

1.3. Label-free whole cell detection

Like other designs of ring resonator biosensors [17] [18], the Maverick platform is specifically designed [19] around cladding sensitivity, the sensitivity of a microring to a uniform change in the refractive index of a fluid covering it, or the binding of many molecular scale biological analytes uniformly coating the ring. This is rightly justified in the context of molecular detection in blood, where the size of the analytes is miniscule compared with the size of the detecting ring. However, a careful analysis presented in this work will show that a design based on cladding sensitivity does not account for important considerations that apply to the case of detecting larger discrete biological analytes, such as viruses and bacterial cells. Given the motivation for sensing bacterial pathogens as described in section 1.1, it would therefore be desirable to fully consider and optimize microring resonators for the case of bacterial detection.

Few attempts at label-free sensing of larger discrete biological objects such as viruses [32] and bacterial cells [35] [36] [37] [38] have been reported in literature, with [32] [37] [38] using the

Maverick platform. Previously employed microrings have not attempted a systematic design optimization towards relatively large discrete biological analytes, including viruses and cells, which has resulted in low [35] [37] [38] or no [36] [38] sensitivity to cells. [35] used a high index glass, which compared to silicon gives low refractive contrast and low sensitivity, and did not design with discrete biological analytes in mind. A minimum concentration sensitivity of 10^5 CFU/mL was reported, which required a large number of bacteria bound to the ring to elicit this response. [36] explored a silicon racetrack resonator spiral in an attempt to increase the sensing area in a microfluidic demonstration but did not detect whole cells. [37] used the Maverick platform to detect *E. Coli* and *C. Jejuni* with unspecified sensitivity and was focused on binding chemistry rather than the optical response of the ring to the bacteria. [38] used the Maverick platform, was unable to detect *E. Coli* in the TE mode, but was able to show unspecified sensitivity with the more sensitive TM mode. Notably, all previous demonstrations have had large ring radii (150 μm for [36], 50 μm for [35], and 15 μm for [37] and [38]) which, as will be shown in this work, limits the sensitivity to discrete biological analytes.

Considering the case of an optimal ring resonator sensor for the detection of discrete biological analytes, such as bacterial cells, it would be desirable to be able to detect bacteria with maximum sensitivity, as well as modulate the sensitivity of different rings to achieve a high dynamic range. In the limiting case of maximum sensitivity, a ring would be able to detect the presence of down to a single bacterial cell bound to it, for all potential binding geometries, giving a sensor resolution of 1 cell. This is contrasted with the detection limit of the device, the number of cells in solution (typically reported as colony forming units per milliliter, or CFU/mL) required to elicit a detectable response from the sensor. The sensor resolution depends on the properties of the sensing element (the microring), its measurement, and the particulars of the analyte of interest. The detection limit additionally depends strongly on the chemical functionalization which binds the analyte to the ring, and the design of the microfluidic delivery system to get the analyte to the ring to be bound.

It would thus be useful to focus on the optical properties of the microring resonator as a sensing element in a label-free whole bacterial sensor, decoupled from the chemical functionalization and microfluidic system components, in order to optimize the performance on the ring itself. An optimized ring, capable of down to single cell sensor resolution for a particular analyte, regardless

of binding geometry, could then be integrated into a multiplexed array in order to maximize the total sensing volume of the device. The optimized optical element, as well as the general optimization approach, could then be used by other researchers in combination with optimized chemical functionalization and optimized microfluidic delivery for a more sensitive integrated device.

1.4. Overview

This work presents the design, computational simulation, experimental photoresist cellular simulation, and experimental proof of concept demonstration of a feasible ring resonator sensor structure for use in sensing discrete micron sized objects such as unicellular microorganisms, with the goal of discrete analyte sensitivity and maximizing the number of rings that can be arrayed (multiplexed) into one device. Optical detection is usually considered as a uniform effect, dependent on the wavelength shift of the cavity as well as sharpness of the resonant peak. However, chemical and biological analytes are individual objects that bind to sensors in discrete amounts. This is particularly true for biological cellular analytes, which have sizes on the order of microns. By analyzing a cavity from the perspective of discrete binding events, this work demonstrates that the sensing response to individual analytes can be greatly enhanced by reducing the cavity length. In practice, this means optimizing a cavity for both sensed analyte optical size and cavity finesse. Finesse is also seen to be the figure of merit for multiplexing, meaning that maximal finesse will both offer high sensitivity and high integration capacity.

The major results of this work are the demonstration of the large effect cavity size has on discrete analyte sensitivity, the usefulness of finesse in capturing that effect and multiplexing, a rigorous comparison between 3D computational simulations and experiment, proof of concept experimental cellular simulation, and demonstration of discrete cellular detection. The proof of concept measurements, together with simulation, strongly indicate the potential of optimized microring resonators for single cell resolution sensing. This was then confirmed through measurements of *E. coli* cells by an array of optimized sensors in an aqueous environment.

Chapter 2 begins with a review of microring resonator theory, the origins of important microring resonator figures of merit, and a derivation of the equations for cladding sensing.

Novel contributions from the author begin with chapter 3, a theoretical derivation of the response of a microring to a single bound analyte, expressed both in terms of the magnitude of resonant shift (sensitivity) and shift normalized to resonance linewidth (figure of merit). The sensitivity of a microring cavity to a single bound cell is found to be the product of sensed analyte optical size and free spectral range, and thus has strong radius dependence (though the free spectral range). To quantify the resolvability of a shift, the discrete analyte sensing figure of merit is then derived that depends simply on sensed analyte optical size and cavity finesse. The motivations for exploring microring parameters, including material, waveguide dimensions, mode polarization, wavelength, and ring radius, are then discussed.

In chapter 4, computational modeling is used to design a microring capable of robust single analyte resolution sensing, with *E. Coli* as a model analyte. A 2D model is developed to find the effective refractive index shift of the cross-section of a large ring with a single cellular analyte bound in a variety of geometries. The finesse achievable by different potential rings is also discussed. Optimized parameters from these studies are then used for a full 3D simulation of transmission spectra for critically coupled rings with and without a single bound cell. A full range of binding scenarios are considered in 3D to give a complete view of potential performance.

In chapter 5, experimental photoresist cellular simulants (referred to simply as cellular simulants) are designed with optical volume corresponding to a single bound cellular analyte to demonstrate the potential real-world sensing response of the resonator. Once deposited on silicon microrings, the resonator transmission spectrum is measured, and then the cellular simulant is removed. The wavelength shift due to the removal of the cellular simulant is measured and normalized with respect to identical rings with no deposited cellular simulant, which serve as temperature controls. The measured results demonstrate that a properly designed compact ring in TM O-Band operation can have a detectable response due to the optical path length difference of a single bound cellular analyte across a complete range of binding scenarios.

In chapter 6, optimized TM O-band rings are maximally arrayed into one sensing device. This fabricated device is then used in an experimental proof of concept to detect the presence of *E. Coli*

cells in an aqueous solution. The results demonstrate the discrete analyte resolution capability of the optimized rings and validate the work in previous chapters.

Chapter 7 offers a summary, conclusion, and future work. It is concluded that the optimization presented succeeded in designing rings capable of discrete analyte resolution sensitivity, and that the optimization process may be broadly useful for other applications of microrings sensing discrete biological analytes.

2. MICRORING RESONATOR THEORY

2.1. Overview

Microring resonator sensors, as considered in this work, consist of a dielectric waveguide loop, evanescently coupled to an input dielectric waveguide, which respond to environmental changes in refractive index. The motivations behind the optimization in this work are based on considering the microring sensor and discrete analyte as a system and optimizing both the general sensitivity of the ring and the specific sensitivity to discrete analytes. The basic underpinnings of dielectric waveguides, evanescent mode coupling, and the origin of refractive index sensing are reviewed in this chapter in order to clearly establish the importance of these component factors, and the differences between the case of bulk refractive index sensing and discrete analyte sensing.

2.2. Mechanism of dielectric waveguides

2.2.1. Refractive index

In a material, behavior of electromagnetic waves will be primarily defined by the electric permittivity ε and magnetic permeability μ [39]. Here, we consider homogenous, isotropic materials with exclusively real electrical permittivities, and magnetic permeabilities equal to that of free space $\mu = \mu_r\mu_0 = \mu_0$. Electromagnetic waves will travel with a phase velocity v_p defined as the ratio of the temporal angular frequency ω to the spatial angular frequency k:

$$v_p = \frac{\omega}{k} = \frac{2\pi f}{2\pi / \lambda_{mat}} = f\lambda_{mat} = \frac{f\lambda_0}{n} = \frac{c}{n} = \frac{1}{\sqrt{\mu\varepsilon}}, \tag{2.1}$$

where f is the frequency (cycles per second), λ_{mat} is the distance between phase peaks in the material, λ_0 is the free space wavelength, c is the speed of light in a vacuum, and n is the refractive index. The refractive index is therefore defined as the phase speed retardation relative to the free space speed of light, given as the ratio of the speed of light in a vacuum c to the phase velocity v_p of the wave in that medium. Given the material constraints previously stated, this is equivalent to:

$$n = \frac{c}{v_p} = \frac{1/\sqrt{\varepsilon_0\mu_0}}{1/\sqrt{\varepsilon\mu}} = \frac{1/\sqrt{\varepsilon_0\mu_0}}{1/\sqrt{\varepsilon_r\varepsilon_0\mu_r\mu_0}} = \sqrt{\varepsilon_r\mu_r} = \sqrt{\varepsilon_r}. \tag{2.2}$$

Free space wavelength ($\lambda_0 = c/f$) is used subsequently as simply λ and should not be confused with the spacing between wave fronts in the material ($\lambda_{mat} = \lambda_0/n$).

In general, ε and μ (for materials with $\mu_r \neq 1$, though these are not considered in this work) vary with wavelength, resulting in a v_p (and therefore n) that varies with wavelength. Attention to this important fact may be highlighted in subsequent sections by denoting n as $n(\lambda)$, but this dependence applies whether it is specifically denoted or not. It is useful then to designate the first order change in ω with respect to k (around a central value ω_0) as the wave envelope group velocity, or simply group velocity v_g:

$$v_g = \left.\frac{\partial\omega}{\partial k}\right|_{\omega=\omega_0} = \frac{1}{\frac{\partial k}{\partial\omega}} = \frac{1}{\frac{\partial}{\partial\omega}\left(\frac{\omega n(\omega)}{c}\right)} = \frac{c}{n(\omega)+\omega\frac{\partial n(\omega)}{\partial\omega}} = \frac{c}{n_g}. \tag{2.3}$$

A group velocity refractive index n_g is thus defined in terms of ω as:

$$n_g = n(\omega)+\omega\frac{\partial n(\omega)}{\partial\omega}. \tag{2.4}$$

Given $\omega = 2\pi c/\lambda$, the group index n_g may be redefined in terms of λ:

$$n_g = n(\lambda)+\omega\frac{\partial}{\partial\omega}(\lambda)\frac{\partial n(\lambda)}{\partial\lambda} = n(\lambda)+\omega^2\lambda\frac{\partial}{\partial\omega}\left(\omega^{-1}\right)\frac{\partial n(\lambda)}{\partial\lambda}. \tag{2.5}$$

Simplifying exclusively in terms of λ then gives:

$$n_g = n(\lambda)-\lambda\frac{\partial n(\lambda)}{\partial\lambda}. \tag{2.6}$$

It should be noted that the definition of n in Eq. 2.2 (which depends on the phase retardation) could potentially be written more explicitly as n_p to differentiate it from group refractive index n_g, though this is not done here.

2.2.2. Total internal reflection

Total internal reflection is used to control the behavior of light in a variety of applications, from fiber optics to binoculars. The case of a plane wave traveling in a system of dielectrics, consisting

of homogenous, isotropic materials with exclusively real electrical permittivities ε, containing no free or bound surface charges, and a magnetic permeability μ equal to that of free space $\mu = \mu_r\mu_0 = \mu_0$ may be considered.

The plane wave encounters a flat material boundary at an incident angle θ_i. The discontinuity in refractive index causes both a reflected wave and a transmitted wave to be generated. The reflected wave leaves with an angle $\theta_r = \theta_i$, while the transmitted wave is refracted. The new angle of propagation, θ_t, is determined by the refractive index change and the incident angle and can be determined by applying the boundary conditions of Maxwell's equations to the interface. This situation is seen below in Figure 2.1.

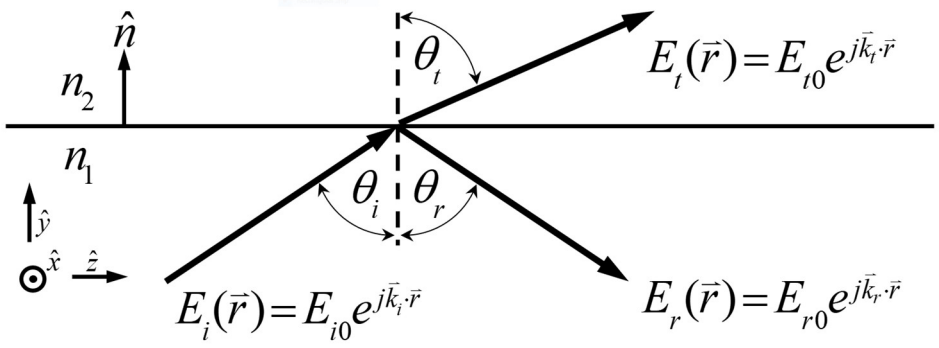

Figure 2.1. Monochromatic, sinusoidal steady state wave incidence at a dielectric boundary.

The fields are monochromatic, and sinusoidal steady state, such that the time independent electric field vector $\vec{E}(\vec{r})$ at a position $\vec{r}$ relates to the time dependent form through:

$$\vec{E}(\vec{r},t) = \mathrm{Re}\left(\vec{E}(\vec{r})e^{-j\omega t}\right) = E_o e^{j\left(\vec{k}\cdot\vec{r}-\omega t\right)}\hat{e} \tag{2.7}$$

where $j = \sqrt{-1}$ is the imaginary unit, t is time in seconds, $\vec{k}$ is the wave vector, and the polarization of the electric fields is in the arbitrary direction of $\hat{e}$. Although polarization will be generally important for considering the amplitudes of the generated waves, the derivation here only considers the case of total internal reflection, in which it does not play an important role.

In general, the electric and magnetic fields across a boundary between homogenous materials defined by the normal vector $\hat{n}$ are given by [40]:

$$\hat{n}\times\left(\vec{E}_2(\vec{r})-\vec{E}_1(\vec{r})\right)=0, \tag{2.8}$$

$$\hat{n}\cdot\left(\vec{D}_2(\vec{r})-\vec{D}_1(\vec{r})\right)=\sigma(\vec{r}), \tag{2.9}$$

$$\hat{n}\times\left(\vec{H}_2(\vec{r})-\vec{H}_1(\vec{r})\right)=0, \tag{2.10}$$

$$\hat{n}\cdot\left(\vec{B}_2(\vec{r})-\vec{B}_1(\vec{r})\right)=\vec{J}_s(\vec{r}). \tag{2.11}$$

The materials considered here are linear and isotropic (implying $\vec{D}=\varepsilon\vec{E}$ and $\vec{B}=\mu\vec{H}$), dielectric insulators (implying current density $\vec{J}_s(\vec{r})=0$), no bound charges are present ($\sigma(\vec{r})=0$), and magnetic permeability is equal to that of vacuum ($\mu=\mu_r\mu_0=\mu_0$). Separating the fields into normal and tangential components, the boundary equations then reduce to:

$$E_{1t}=E_{2t}, \tag{2.12}$$

$$\varepsilon_1 E_{1n}=\varepsilon_2 E_{2n}, \tag{2.13}$$

$$\vec{B}_1=\vec{B}_2, \tag{2.14}$$

where subscripts *t* and *n* refer to tangential and normal field components, respectively. The magnetic field $\vec{B}$ is unchanged across the boundary because magnetic permeability is assumed to be unchanged across the interface and equal to that of free space, and thus magnetic fields may be neglected for the remainder of this work.

At the interface, the incident wave, the reflected wave, and the transmitted wave must be continuous. Therefore, the electric fields at the interface must satisfy:

$$\vec{E}_i(\vec{r})+\vec{E}_r(\vec{r})=\vec{E}_t(\vec{r}), \tag{2.15}$$

$$E_{i0}e^{j\vec{k}_i\cdot\vec{r}}+E_{r0}e^{j\vec{k}_r\cdot\vec{r}}=E_{t0}e^{j\vec{k}_t\cdot\vec{r}}. \tag{2.16}$$

The wave vector $\vec{k}$ has a direction in the wave propagation direction, with a magnitude:

$$\left|\vec{k}\right|=\sqrt{k_x^2+k_y^2+k_z^2}=k=\frac{\omega}{v_p}=\frac{2\pi f}{c/n}=\frac{2\pi n}{\lambda}. \tag{2.17}$$

To maintain a constant spatial frequency across the entire interface, the exponential terms must be equal, implying for all $\vec{r} = (x, y, z)$ along the interface:

$$\vec{k}_i \cdot \vec{r} = \vec{k}_r \cdot \vec{r} = \vec{k}_t \cdot \vec{r}. \tag{2.18}$$

Spatial periodicity at the interface only exists in the *z* direction, as the fields are uniform in the *x* direction, and the value of *y* is constant and arbitrary. Thus, the *z* components must be equal for all values of *z*:

$$k_{i,z} = k_{r,z} = k_{t,z}\Big|_{-\infty \le z \le \infty}. \tag{2.19}$$

In component form, for the coordinate system defined in Figure 2.1, this implies that:

$$k_i \sin\theta_i = k_r \sin\theta_r = k_t \sin\theta_t. \tag{2.20}$$

Substituting for the values of the wavenumbers (k) from Eq. 2.17 shows:

$$\frac{2\pi n_1}{\lambda}\sin\theta_i = \frac{2\pi n_1}{\lambda}\sin\theta_r = \frac{2\pi n_2}{\lambda}\sin\theta_t. \tag{2.21}$$

As $\theta_i = \theta_r$, the reflected term adds no new information. Simplifying then gives:

$$n_1 \sin\theta_i = n_2 \sin\theta_t. \tag{2.22}$$

This result is known as Snell's law [39], and describes refraction for all incident angles:

$$\theta_t = \arcsin\left(\frac{n_1}{n_2}\sin\theta_i\right). \tag{2.23}$$

We then consider the special case of $\mathrm{Re}(\sin\theta_t) = 1$, which gives $\theta_t = \pi/2$. This only occurs if $n_1 > n_2$, and results from an incident angle:

$$\theta_i \ge \arcsin\frac{n_2}{n_1}. \tag{2.24}$$

The angle at this transition point is denoted as the critical angle, θ_c:

$$\theta_c = \arcsin\frac{n_2}{n_1}. \tag{2.25}$$

It should be noted that Snell's law (Eq. 2.22) applies above the critical angle as well. However, while $\mathrm{Re}(\theta_t) = \pi/2$ for this case, there will be an imaginary component of θ_t as θ_i continues to increase. This imaginary component is not needed for the remainder of the derivation here but could be used to alternately derive the wave vector of the transmitted wave in such a case.

For the collection of incident angles above the critical angle, the power in the incident wave will be completely transferred to the reflected wave. This result is known as total internal reflection, and in the simplified case, gives a complete reflection of the incoming power from a high refractive index to a lower refractive index material if the incident angle is greater or equal to the critical angle.

2.2.3. Evanescent wave

Referring to Figure 2.1, although no power transfer occurs for the transmitted wave, there will still be a field in region 2. As there is not power transmitted to this field, the term "transmitted" does not quite apply. It is instead referred to as the evanescent (or "vanishing") wave. The *z* component of the evanescent field still must match the spatial periodicity described in Eq. 2.19:

$$k_{e,z} = k_{i,z} = \frac{2\pi n_1}{\lambda}\sin\theta_i. \tag{2.26}$$

The magnitude of the total wavevector of the evanescent field is defined as before in Eq. 2.17:

$$\left|\vec{k}_e\right| = \frac{2\pi n_2}{\lambda} = \sqrt{{k_{e,z}}^2 + {k_{e,y}}^2} = \sqrt{\left(\frac{2\pi n_1}{\lambda}\sin(\theta_i)\right)^2 + {k_{e,y}}^2}. \tag{2.27}$$

The *y* component can then be isolated:

$$k_{e,y} = \frac{2\pi}{\lambda}\sqrt{\left(n_2\right)^2 - \left(n_1\sin(\theta_i)\right)^2}. \tag{2.28}$$

From Eq. 2.24, it is known that $n_1\sin(\theta_i) \geq n_2$, meaning $k_{e,y}$ will be imaginary. The magnitude of this imaginary part can then be redefined in terms of an intensity attenuation constant α. This is expressed as an intensity attenuation (equivalent to energy or power attenuation) rather than a field attenuation to aid in later descriptions of attenuation of optical intensity. Since $I(\vec{r}) \propto \left|\vec{E}(\vec{r})\right|^2$, this

α is a factor of 2 smaller than a similarly defined field attenuation constant would be. By substitution:

$$k_{e,y} = j\frac{\alpha_{e,y}}{2} = j\frac{2\pi}{\lambda}\sqrt{\left(n_1\sin(\theta_i)\right)^2 - \left(n_2\right)^2}. \tag{2.29}$$

Combining the *z* and *y* components, $\vec{k}_e$ will thus be complex, with the real component describing a propagation constant in the *z* direction ($\beta_{e,z}$) and the imaginary component describing the field attenuation in the *y* direction ($\alpha_{e,y}/2$):

$$\vec{k}_e = \beta_{e,z}\hat{z} + j\frac{\alpha_{e,y}}{2}\hat{y} = \left(\frac{2\pi n_1}{\lambda}\sin\theta_i\right)\hat{z} + j\left(\frac{2\pi}{\lambda}\sqrt{\left(n_1\sin(\theta_i)\right)^2 - \left(n_2\right)^2}\right)\hat{y}. \tag{2.30}$$

From Eq. 2.7, the field will then be in the form of:

$$E_t(\vec{r}) = E_{t0}e^{j\vec{k}_e\cdot\vec{r}} = E_{t0}e^{j(\beta_{e,z}z + j\alpha_{e,y}y/2)} = E_{t0}e^{j\beta_{e,z}z}e^{-\alpha_{e,y}y/2}. \tag{2.31}$$

Thus, as the incident angle increases beyond the critical angle, non-propagating fields in the *y* direction will ensure spatial periodicity is maintained without violating momentum conservation.

The exponential falloff of the field will increase as the incident angle increases beyond θ_c, and be bounded between extremes as:

$$0\Big|_{\theta_i=\theta_c} < \mathrm{Im}(\vec{k}_e) < \frac{2\pi}{\lambda}\sqrt{n_1^2 - n_2^2}\Bigg|_{\theta_i=\pi/2}. \tag{2.32}$$

The attenuation constant will therefore be largest at nearly parallel angles of incidence, and smallest near the critical angle.

2.2.4. One-dimensional dielectric waveguide

Total internal reflection may be used to construct a theoretically loss free waveguiding structure. Such a structure is seen below in Figure 2.2, with a waveguide core of height *h* and refractive index n_1 surrounded by an overcladding with index n_2 and undercladding with index n_3:

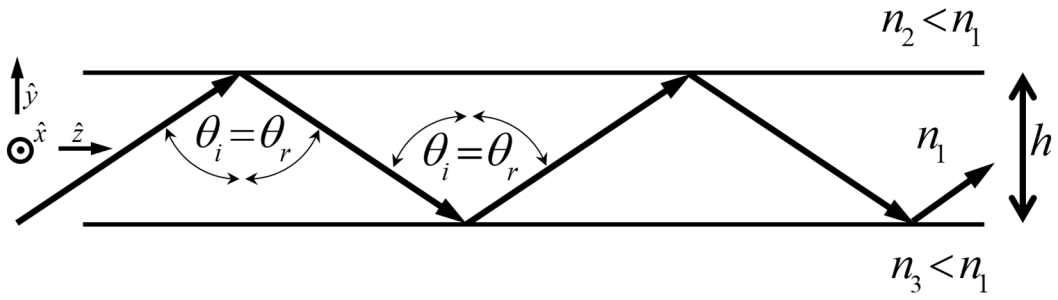

Figure 2.2. One-dimensional dielectric waveguide stack.

For total internal reflection to occur, it is required that $\theta_i \geq \arcsin(n_2/n_1)$, $\theta_i \geq \arcsin(n_3/n_1)$, $n_3 < n_1$, and $n_2 < n_1$. Letting $k_x = 0$, the wavenumber will be given by:

$$\left|\vec{k}_1\right| = k_1 = \frac{2\pi n_1}{\lambda} = \sqrt{k_y{}^2 + k_z{}^2} = \sqrt{\left(k_1 \cos\theta_i\right)^2 + \left(k_1 \sin\theta_i\right)^2}. \tag{2.33}$$

2.2.4.1. Supported modes

To propagate without loss, the propagating beam must constructively interfere with itself. The fixed height h in the y direction imposes the restriction that the round-trip phase ϕ_{RT} must be a multiple m of 2π after the light has traveled a distance $2h$ in the y direction:

$$\phi_{RT} = 2\pi m = \phi_{2h} + \phi_{12} + \phi_{13} = 2h\frac{2\pi n_1}{\lambda}\cos\theta_i + \phi_{12} + \phi_{13}, \tag{2.34}$$

where $\phi_{2h} = 2hk_y$, and ϕ_{12} and ϕ_{13} are the phase shifts due to reflections at the overcladding and undercladding, respectively. Both boundary phase shifts depend on the incident angle, refractive indices on both sides of the boundary, and the field polarization, and each will be constant for a given set of these parameters [41]. As a result, for a waveguide with fixed height and materials, only particular combinations of λ and θ_i that result in integer m values will propagate loss free. These combinations are known as waveguide modes.

For a given set of materials, the number of modes supported by a waveguide will depend on the height h. A large h will support a variety number of modes, and a smaller h will similarly decrease the number of supported modes. In the limiting case of a single mode $m = 1$ being supported, for the simplified waveguide case of $n_2 = n_3$, it will hold that $\theta_i = \theta_c$, and $\phi_{12} = \phi_{13} = 0$. Substituting

these values into Eq. 2.34, along with the definition of the critical angle in 2.25 and solving for this single mode height gives:

$$h_{sm} = \frac{\lambda}{2\sqrt{n_1^{\,2} - n_2^{\,2}}}. \tag{2.35}$$

If the structure has a high index contrast such that $n_2 << n_1$, this further reduces to the half-wave limit:

$$h_{sm}\big|_{n_2 << n_1} = \lambda / \left(2n_1\right). \tag{2.36}$$

2.2.4.2. Modal effective refractive index

In the waveguide, light will effectively propagate along the path of the waveguide more slowly than the true phase velocity $v_{p,1} = c/n_1$ in region 1 due to the inclination of the light with respect to the z axis. The z component of the propagating wave vector for a particular mode can be represented by the guided wave propagation constant β as in Eq. 2.30. This will be given by:

$$\beta = k_z = k_1 \sin\theta_i = \frac{2\pi n_1}{\lambda}\sin\theta_i = \frac{2\pi n_{eff}}{\lambda}, \tag{2.37}$$

where n_{eff} is the effective refractive index for the guided mode and satisfies $v_{p,eff} = c/n_{eff}$. From Eq. 2.37, the value of n_{eff} will be given by:

$$n_{eff} = n_1 \sin\theta_i = \frac{k_z}{k_0} = \frac{\beta}{k_0}. \tag{2.38}$$

The condition for total internal reflection seen in Eq. 2.24 implies that:

$$n_{eff} > \max\left(n_2, n_3\right), \tag{2.39}$$

or else the wave will not be totally internally reflected and will consequently have a propagation constant β that is non-real.

2.2.4.3. Modal evanescent field

The evanescent field of the propagating mode at an interface *c* (the core-overcladding or core-undercladding interface) will be given by substituting Eq. 2.38 into Eq. 2.30:

$$\vec{k}_e = \beta_{e,z}\hat{z} \pm j\frac{\alpha_{e,y}}{2}\hat{y} = \left(\frac{2\pi n_{eff}}{\lambda}\right)\hat{z} \pm j\left(\frac{2\pi}{\lambda}\sqrt{{n_{eff}}^2 - {n_c}^2}\right)\hat{y}. \tag{2.40}$$

with the sign of the imaginary component depending on the interface. The evanescent wave will therefore propagate with the same propagation constant as the field in the waveguide:

$$\mathrm{Re}(\vec{k}_e) = \beta_{e,z} = \beta, \tag{2.41}$$

and the evanescent field will decay in the *y* direction with:

$$\mathrm{Im}(\vec{k}_e) = \frac{\alpha_{e,y}}{2} = \frac{2\pi}{\lambda}\sqrt{{n_{eff}}^2 - {n_c}^2}. \tag{2.42}$$

The consequence of Eq. 2.42 is that the evanescent field will decrease most quickly for modes with large effective refractive index and surrounding materials with lowest refractive index. Conversely, minimizing this falloff requires a relatively small wavelength, a relatively small effective index, and a relatively small difference between the effective index and the cladding index.

2.2.5. Two-dimensional dielectric waveguide and modeling

For integrated optics, it is generally desirable to confine light in two dimensions, which enables a lateral routing of light on a chip. It is also desirable to design a waveguide which will only support a single waveguide mode at each wavelength to avoid otherwise identical signals propagating with different speeds. However, assuming the waveguide will not strongly act as a polarization converter, two orthogonal polarizations of light may be used without interfering with one another. The work presented here considers a strip waveguide, with a rectangular waveguide core material placed on top of an undercladding and surrounded by an overcladding material. Such a waveguide is seen below in Figure 2.3.

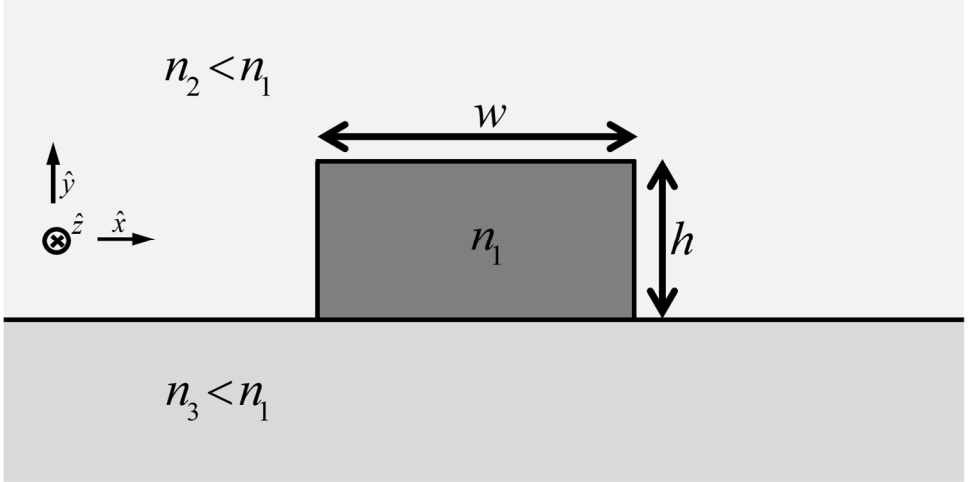

Figure 2.3. Two-dimensional dielectric waveguide cross-section.

This situation is far more complicated [42] than the ones considered in sections 2.2.2, 2.2.3, and 2.2.4. The small size of the waveguide means that the waveguide dimension and material, the waveguide cladding material, and the guided light wavelength and polarization will all strongly affect whether light will be guided, and what that guiding pattern will look like. Furthermore, it is advantageous to be able to consider waveguides that are not exactly rectangular. Fabricated waveguides may have non-ideal features such as a trapezoidal cross-section with a fixed sidewall slope.

To do this, numerical simulation [43] is required. Numerical modeling of electromagnetics problems is a field in and of itself, and this work models comparatively simple structures. As a result, the details of modeling theory will not be covered here but practical comments will be made where appropriate. The finite element method (FEM) and the electromagnetics capabilities of COMOSL Multiphysics [44] will be mainly used, owing to its ability to characterize material dispersion accurately through experimentally obtained values at a variety of wavelengths. The "Electromagnetic Waves, Frequency Domain" study was used with "Mode Analysis" and "Eigenfrequency" studies, as appropriate. Two-dimensional studies were used for approximating infinitely long waveguides, two-dimensional axisymmetric studies were used for approximating isolated waveguide rings, and three-dimensional studies were used with coupled resonators.

For two-dimensional models, briefly, a particular cross-section of a waveguide is modeled, and the situation is decomposed into an eigenvalue problem. Using a form of the Helmholtz equation:

$$\nabla \times \left(\nabla \times \vec{E} \right) + \lambda^2 \vec{E} = 0, \tag{2.43}$$

and a given set of boundary conditions, the eigenvalue λ may be solved. For loss free materials, this eigenvalue will be equal to:

$$\lambda = -j\beta \tag{2.44}$$

where β is given by Eq. 2.37, with an imaginary component present for lossy modes.

2.2.6. Evanescent wave coupling

As discussed in section 2.2.3, in the case of total internal reflection, a field extends outside the higher refractive index material (the waveguide core) into the lower index material (the waveguide cladding). The extent of this field depends on the coupling angle of incident light, and it does not transmit power. However, if another high index material is encountered by the evanescent field before it has decayed completely, it may again form a propagating wave carrying power [45]. This phenomenon is said to "frustrate" the total internal reflection because this causes a power loss and is thus known as frustrated total internal reflection. It is similarly referred to as evanescent wave coupling, as the evanescent wave is used to couple power from one material to another. However, due to the fast falloff of the evanescent wave as seen in Eq. 2.42, it requires materials close to one another, typically on the order of the wavelength of light.

2.2.7. Loss mechanisms

In contrast to the ideal cases mentioned here thus far, supported modes in real waveguides will be subject to losses from non-idealities [9] [46] [47]. These include scattering loss [13] [48] [49] [50], mode coupling loss [51], absorption loss [52] [53], bending loss [54] [55] [12], and inter-waveguide coupling loss [56].

Scattering losses may result from imperfections in the waveguide itself, as well as from scattering at the waveguide boundaries. This would be due to surface roughness at the top and bottom of the waveguide, and the waveguide sidewalls.

Mode coupling loss [57] is a result of power transferred out the mode of interest to either higher order modes [58], counter propagating modes [59] [60] [61] [62], or to modes in other polarizations [63]. Coupling to higher order modes may be reduced by working with a single mode waveguide, with a bottom cladding thick enough to prevent coupling to any substrate modes. However, coupling to counter propagating modes as a result of sidewall roughness has been seen to be a significant source of losses in real devices [64] [65] [66] [67] [68] [69] [70] [71] [72].

Absorption losses in the infrared are extremely small in crystalline silicon due to its large band gap. However, the large power buildup in optical resonators means that losses due to two photon absorption (TPA) can become significant at relatively low powers. Additionally, the losses due to the absorption of water are significant in the NIR, making the consideration of absorption loss an important consideration for aqueous sensors. Water absorption, as seen in Figure 2.4, motivates the exploration of the O-band centered around 1310 nm, as well as the more common C-band around 1550 nm. A characteristically lower absorption near 1310 nm compared to 1550 nm is also seen is non-aqueous solvents as well [73], making the O-band of general interest for sensing with liquid overcladdings.

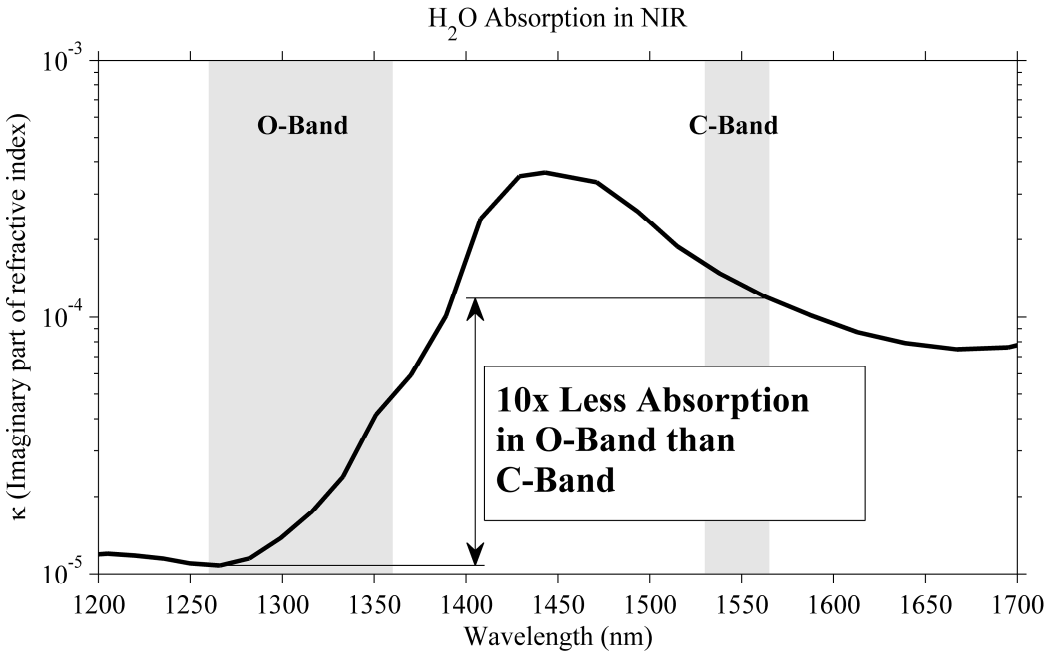

Figure 2.4. Absorption of water in the near infrared (data from [74]).

Bending losses may result from radiation or increased scattering losses due to the change in modal distribution at bends. For radiation, this is negligible for large radii, but significant as the size of a ring is minimized. Radiation loss is frequently dealt with simply by working at radii beyond the point where radiation losses would be limiting. However, for this work, a desire to maximize sensitivity means exploring the regime close to where these losses are significant.

The relative importance of these mechanisms will depend on the waveguide material, the waveguide dimension, mode polarization, mode wavelength, and bending radii. Mathematically, these loss mechanisms may be incorporated into the developed definitions of both refractive index and wavenumber through the addition of a complex component. This was done previously for wavenumber in Eq. 2.30, and may be generalized:

$$\tilde{k} = \frac{2\pi n}{\lambda} + j\frac{\alpha}{2} = k_0 n + j\frac{\alpha}{2} = \beta + j\frac{\alpha}{2} \tag{2.45}$$

For refractive index, using the constituent definition of $n = ck/\omega$ with Eq. 2.45 shows:

$$\tilde{n} = \frac{c\tilde{k}}{\omega} = n + j\frac{\alpha\lambda_0}{4\pi} = n + j\frac{\alpha}{2k_0} = n + j\kappa. \tag{2.46}$$

2.3. Traveling wave optical resonators

The use of total internal reflection based dielectric waveguides allows for low loss structures, and evanescent wave coupling allows for a low loss method of transferring power from one waveguide to another. If a waveguide structure is wrapped upon itself, such that it forms a continuous loop, a properly excited signal will circulate many times with low loss. Such a circuitous optical resonator, if it supports a single dominant propagating mode, will also be a travelling wave resonator.

This is in contrast with an optical resonator based on a single waveguide section with high reflectivity ends defining the resonator boundaries. A Fabry-Perot type resonator such as this will have a standing wave pattern, meaning optical fields will only be present for a fraction of the total cavity. In a single mode circuitous optical resonator, the travelling wave pattern will give an equal average power throughout the circumference. Such a resonator will be ideal for sensing applications, as the entire circumference will have evanescent fields that may be used for environmental sensing. The travelling wave nature of a circuitous optical resonator will, however, be degraded to a degree if the waveguide becomes multimode or contains a counter-propagating degenerate mode carrying power comparable to the forward propagating mode.

2.3.1. Circuitous optical resonators

Many circuitous structures are conceivable which would support an optical mode. These are generally separable into two categories: whispering gallery mode resonators and optical ring resonators. Whispering gallery mode resonators use total internal reflection around a curved material interface for the totality of the resonator circumference. Resonators such as microdisks, microdonuts, microtoroids, and microspheres are all whispering gallery mode devices.

Optical ring resonators, by contrast, make use of a waveguide, and feature total internal reflection at both the exterior and interior waveguide boundaries. A true ring resonator will consist of a single circular waveguide section, but microracetracks will obey largely similar principles of operation. The main difference will be different loss and mode distributions throughout a microracetrack due

to the nonuniform circumference. Additionally, it should be noted that a microring with a cross sectional width large enough to isolate the ring mode from changes in the environment of the interior of the ring are, for the purposes of this work, considered to be microdonuts rather than true microrings. A comparison of the general structure, mode profiles, and resonance shift behavior of microring resonators (representing the optical ring resonator category) and microdisk [75] resonators (representing the whispering gallery mode category) can be seen in Figure 2.5. Importantly for sensing applications, the resonance shift of a whispering gallery mode resonator inherently depends on the cavity radius, while that of an optical ring resonator does not.

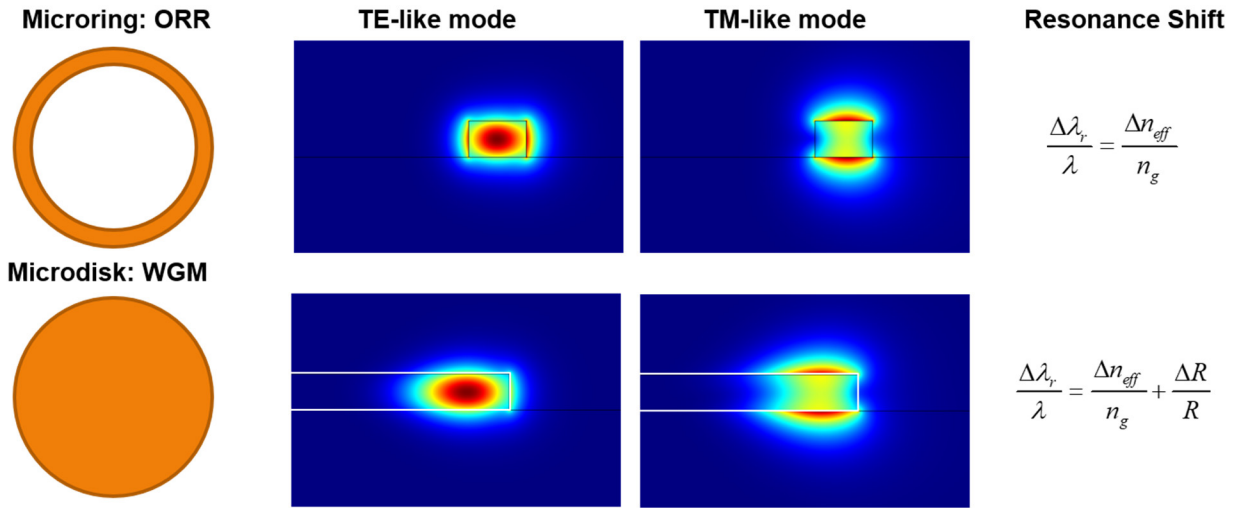

Figure 2.5. Comparison of microring (optical ring) resonator and microdisk (whispering gallery mode) resonator structures, mode profiles, and sensitivities.

2.3.2. Microring resonators

Microring resonators are optical ring resonators consisting of a closed waveguide loop and power input/output structures. The input and output structures are typically evanescently coupled waveguides, although other methods such as cascaded resonators and in-resonator grating couplers are possible. Evanescently coupled waveguide setups will be considered throughout the remainder of this work. A resonator coupled by a single waveguide is referred to as an “all pass” configuration, and a double waveguide coupled resonator is referred to as an “add-drop” configuration.

Resonance in a ring resonator is achieved through constructive interference between the excitation waveguide and the travelling mode(s) in the resonator. The basic resonance condition requires the circulating resonator mode to interfere constructively with the input waveguide mode. In this case, a high intensity mode builds up in the resonator, and saturates when the building input power balances with the power lost in the resonator due to loss factors. Off resonance, destructive interference minimizes the effect of the resonator on the input waveguide(s).

It should be emphasized that, as mentioned in section 2.2.7 and especially for relatively high Q resonators, it is atypical for radiation loss to be the main reason for resonance peak broadening and extinction ratio degradation. Mode coupling is the typical culprit [57], whether it be to higher order modes [58] (which themselves have intrinsic radiation loss) or coupling to counter propagating modes [59] [60] [61] [62]. These counter propagating modes are degenerate to the forward propagating ring mode at low power but lose this degeneracy as either power increases or surface scattering losses become more apparent. The effect of this is to couple power back into the input port, which could pose a complicated problem for cascaded resonators operating at the same resonance wavelength. Additionally, the counterpropagating mode begins to form a standing wave in the ring cavity. The intensity difference between the high and low intensity areas is determined by the strength of coupling to the counter propagating mode. In the extreme case, this could result in a standing wave cavity being formed as opposed to a travelling wave. This situation will be neglected for the purpose of this work, as relatively isolated sensors are considered here. It would, however, be significant for attempts at highly integrated devices with many sensors on the same waveguide.

The resonators considered in this work are limited to isotropic dielectric insulators/semiconductors. Additionally, it is assumed that optical power is low enough to avoid nonlinear optical effects, and experimental efforts reduced the input power to attempt to stay in the linear optical regime. Nonlinear effects in rings have been explored for a variety of interesting effects, however for this work they are considered a hindrance due to the degradation of the quality factor. Other effects such as optical trapping of particles are likewise ignored. Due to the intentionally decreased optical power, and the swept wavelength of light input into the ring, they have not been observed for this work.

2.4. Microring resonator relationships

2.4.1. Resonant wavelength

The resonance wavelength λ_m of a microring resonator for a particular integer mode number m is equal to the optical path length (OPL, the phase round trip optical length), experienced by the mode divided by that integer mode number m:

$$\lambda_m = \frac{OPL}{m} = \frac{L_m n_{eff,m}}{m}. \tag{2.47}$$

The mode number m is equal to the number of energy maxima (or minima) in the ring on resonance.

For a uniform ring, OPL is simply the product of the physical path length L_m and the effective refractive index $n_{eff,m}$ experienced by the mode, both of which vary with wavelength. The physical path length $L_m = 2\pi R_m$ is the circumference of the circle with radius R_m defined by the distance from the mode center to the ring radial center. For a true ring resonator, R_m should be quite close to the ring waveguide center R_{ring}, with a small divergence resulting from $R_m > R_{ring}$. The divergence $R_m - R_{ring}$ will increase as the waveguide dimensions are increased, the radii is decreased, and the mode is less tightly confined, resulting in an R_m shifted towards the outside edge of the ring. An R_m approaching the outer radius of the waveguide is indicative of guiding by the outer edge of the waveguide exclusively, and characteristic of a whispering gallery mode rather than a ring resonator mode. An example of a ring resonator mode and the divergence $R_m - R_{ring}$ is seen in Figure 2.6.

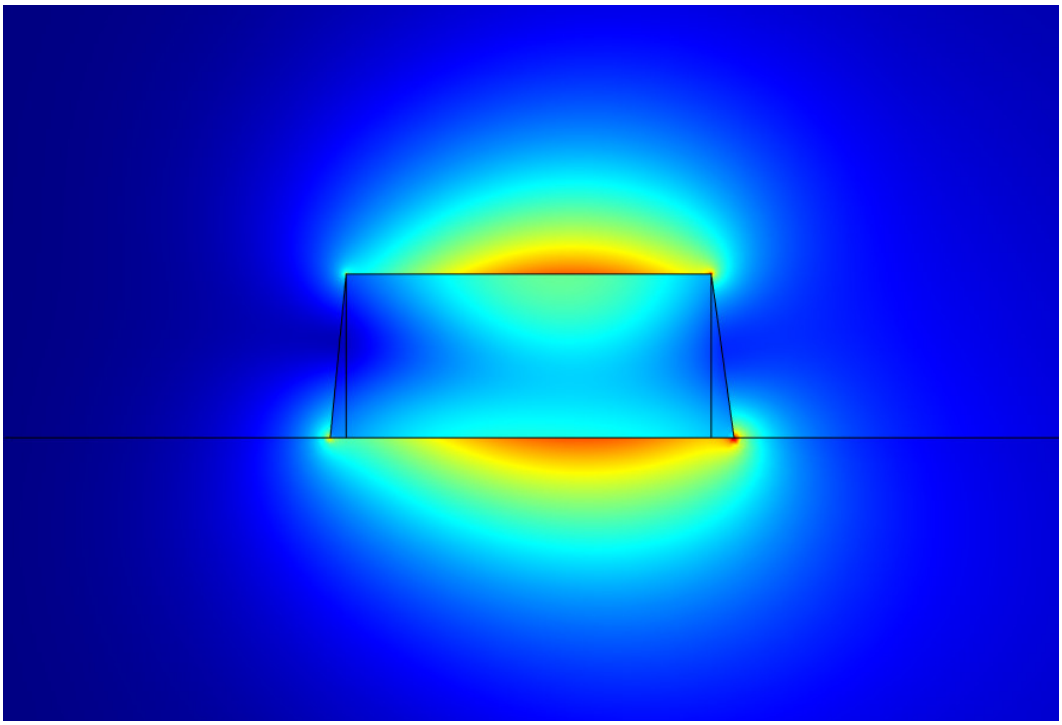

Figure 2.6. Electric field distribution of a ring resonator mode waveguide cross-section.

Assuming the resonator is structured with a waveguide dimension small enough to support true ring modes, the effect of this shift may be absorbed into a redefined n_{eff}. For subsequent use, we let $OPL = L_m n_{eff,m} = L n_{eff}$ such that:

$$L \triangleq 2\pi R_{ring}, \tag{2.48}$$

and:

$$n_{eff} \triangleq n_{eff,m} \cdot 2\pi \left(R_m - R_{ring} \right). \tag{2.49}$$

The resonant wavelength λ_m may then be expressed as:

$$\lambda_m = \frac{OPL}{m} = \frac{L n_{eff}}{m}. \tag{2.50}$$

For a given cavity L and mode number m, the resonant wavelength λ_m will depend on n_{eff}, which alone varies with the optical and ring parameters. Determining n_{eff} will require measurement or numerical simulation due to its strong dependence on waveguide and microring parameters.

2.4.2. Cavity loss

The microring cavity may be modeled as a harmonic oscillator. This situation may be described by an exponential decay in the energy $U(t)$ stored in a ring that had reached a steady state energy U_0:

$$U(t) = U_0 e^{-t/\tau} = U_0 e^{-\omega_m t/Q}, \tag{2.51}$$

with a decay rate $\tau = Q/\omega_m$, where Q [76] is the quality factor and the angular frequency center $\omega_m = 2\pi f_m = 2\pi c/\lambda_m = k_0 c$.

The total energy in the ring U may be related to the circulating power in the ring cross-section P_c by the optical pulse round trip time T_{RT} such that [77]:

$$T_{RT} = \frac{U(t)}{P_c(t)} = \frac{L_m}{v_g} = \frac{L_m n_{g,m}}{c} = \frac{L n_g}{c}, \tag{2.52}$$

with a redefinition of $n_{g,m}$ to n_g as in Eq. 2.49. The product $Ln_g = L_m n_{g,m} = cT_{RT}$ is the group round trip optical path length, and is, for a wave packet, analogous to the phase round trip optical path length OPL for a phase front.

Defining a round trip power gain G, the ratio of cross-sectional power after one round trip to the cross-sectional power prior to the round trip, we define the intensity attenuation constant (per unit distance) α such that:

$$G = \frac{P_{c,RT}}{P_{c,0}} = e^{-\omega_m T_{RT}/Q} = e^{-\alpha L}. \tag{2.53}$$

In the case of a resonator that has been brought to steady state and then the input power removed, G will be less than one to correspond to loss. Nevertheless, the relation in Eq. 2.53 still holds.

In general, α may be used to account for any relevant set of losses, including those that only occur once per round trip rather than on a per distance basis, as long as it satisfies the relation in Eq. 2.53. Values of attenuation in dB per unit distance (consistent with L) are seen to be $\alpha_{\mathrm{dB}} = \alpha \cdot 10/\ln(10) \approx 4.34\alpha$, and may be converted via $\alpha = \alpha_{dB} \cdot \ln(10)/10 \approx \alpha_{dB}/4.34$. It may also be used to account for the effect of the input waveguide.

Substituting Eq. 2.52 into Eq. 2.53, the value of Q is seen to be:

$$Q = \frac{\omega_m T_{rt}}{\alpha L} = \frac{\omega_m n_g}{\alpha c} = \frac{2\pi n_g}{\alpha \lambda_m} = \frac{k_0 n_g}{\alpha} = \frac{n_g}{2\kappa}, \tag{2.54}$$

with $\kappa = \mathrm{Im}(\tilde{n})$ from Eq 2.46.

2.4.3. Transmission spectrum

The ring is modeled as an underdamped harmonic oscillator, which is valid assuming the loss mechanisms result in homogenous broadening of the resonance width. Using the definition of the quality factor (for large Q) as:

$$Q = \frac{f_m}{\Delta f_{fwhm}} \simeq \frac{\lambda_m}{\Delta \lambda_{fwhm}}, \tag{2.55}$$

the transmission spectra of one resonant peak (with wavelength λ_m from Eq. 2.50) will be given by a modified Lorentzian function:

$$L(\lambda) = 1 - ER \cdot \frac{\left(\lambda_m / 2Q\right)^2}{\left(\lambda - \lambda_m\right)^2 + \left(\lambda_m / 2Q\right)^2}, \tag{2.56}$$

where ER is the power extinction ratio, such that $ER = P_{in}/P_{min}$ where P_{in} is the input power and P_{min} is the power at the bottom of the dip. The full width at half maximum $\Delta\lambda_{FWHM}$ ($FWHM$) is:

$$\Delta\lambda_{FWHM} = \frac{\lambda_m}{Q} = \frac{\alpha \lambda_m^{\,2}}{2\pi n_g} = \frac{2\pi\alpha}{k_0^{\,2} n_g} = 2\kappa \frac{\lambda_m}{n_g}. \tag{2.57}$$

The spacing between adjacent two peaks m and m' is defined as the free spectral range $\Delta\lambda_{FSR}$ (*FSR*). For m' = m + 1 and $\lambda_m > \lambda_{m+1}$, substitution from Eq. 2.50 and simplification with a forward difference approximation of Eq. 2.6 reveals:

$$\Delta\lambda_{FSR^+} = \lambda_m - \lambda_{m+1} = \frac{\lambda_m^2}{Ln_{g^+} + \lambda_m}. \tag{2.58}$$

Similarly, for m' = m − 1 and $\lambda_m < \lambda_{m-1}$, substitution from Eq. 2.50 and simplification with a backwards difference approximation of Eq. 2.6 reveals:

$$\Delta\lambda_{FSR^-} = \lambda_{m-1} - \lambda_m = \frac{\lambda_m^2}{Ln_{g^-} - \lambda_m}. \tag{2.59}$$

A more precise central difference definition, which uses $n_g(\lambda_m)$ as in Eq. 2.57, is then given by:

$$\Delta\lambda_{FSR} = \frac{2}{\left(\Delta\lambda_{FSR^+}\right)^{-1} + \left(\Delta\lambda_{FSR^-}\right)^{-1}} = \frac{\lambda_m^2}{Ln_g}. \tag{2.60}$$

The ring finesse F [76], defined as the ratio between the *FSR* in Eq. 2.60 and *FWHM* in Eq. 2.57, is seen to be:

$$F = \frac{\Delta\lambda_{FSR}}{\Delta\lambda_{FWHM}} = \frac{2\pi}{\alpha L} = \frac{k_0 n_{eff}}{\alpha m} = \frac{n_{eff}}{2\kappa m}. \tag{2.61}$$

The Q and F for a peak m are then related by:

$$\frac{Q}{F} = \frac{\lambda_m}{\Delta\lambda_{FSR}} = \frac{Ln_g}{\lambda_m} = f_m T_{RT} = \frac{n_g}{n_{eff}} m = \frac{n_{g,m}}{n_{eff,m}} m. \tag{2.62}$$

It is notable that Q is independent of resonator size, making it an appropriate performance measure to generally compare dissimilar sized structures. Additionally, its utility in easily characterizing the response of each resonant wavelength is apparent. The transmission spectrum of an all-pass ring will be fully determined by a Q_m, ER_m, and λ_m for each resonance m:

$$T_{AP}(\lambda) = 1 - \sum_{m=1}^{\infty} \frac{ER_m}{\left(2Q_m \cdot \frac{\lambda - \lambda_m}{\lambda_m}\right)^2 + 1}. \tag{2.63}$$

F is less easily characterized and less general. It requires characterization of multiple resonances to extract the FSR and will strongly depend on the size of the resonator through the inverse proportionality to L (or alternately, m). Unlike Q, it is nontrivial to maximize due to an increase in α for decreasing L due to bending and radiation loss. However, the inherent dependence on L reflects important physical effects related to the resonator size, motivating the focus on F later in this work.

2.5. Evanescent field sensing

2.5.1. Waveguide cladding sensitivity

A dielectric waveguide may function as a refractive index sensor if a portion of the waveguide cladding is a fluid, such as a liquid or gas. This portion is typically the entirety of the overcladding (n_2 in Figure 2.3). The effective refractive index of the propagating mode will change in response to a change in cladding material. As this response is due entirely to the evanescent fields, it is known as evanescent field sensing. For a homogeneous change in overcladding refractive index, waveguide cladding sensitivity $S_{c,WG}$ at a wavelength λ_m can be defined:

$$S_{c,WG} = \left.\frac{\partial n_{eff}}{\partial n_c}\right|_{\lambda_m}. \tag{2.64}$$

A more sensitive waveguide will respond to a change in cladding refractive index Δn_c with a corresponding larger Δn_{eff} than a less sensitive waveguide. The change Δn_{eff} will directly result from the change in the cladding index Δn_c, and thus this relation may be used from simulated or measured values if both Δn_c and Δn_{eff} are known for λ_m.

2.5.2. Effective index change

For a given waveguide cross-section, if the field distribution of given mode is known, the effective index can be calculated. For a dielectric waveguide consisting of linear, isotropic materials, and considering only a single wavelength of input light, the directional energy flux in the direction of propagation (i.e. Poynting vector) will be the product of the electromagnetic energy density and the phase velocity [39]:

$$\vec{S} = u_{EM} v_p \hat{k} = u_{EM} \frac{c}{n_{eff}} \hat{k}. \tag{2.65}$$

Integrating over a cross-section of interest reveals:

$$\int_A \vec{S} \cdot \hat{a} dA = v_p \int_A u_{EM} \hat{k} \cdot \hat{a} dA = v_p \int_A u_{EM} dA. \tag{2.66}$$

Given that the materials are linear, without a loss of generality the power flow may be normalized to unity:

$$\int_A \vec{S} \cdot \hat{a} dA = 1. \tag{2.67}$$

The effective index is then seen to be:

$$n_{eff} = c \int_A u_{EM} dA = c \int_A \frac{1}{2} \left(\vec{E} \cdot \vec{D} + \vec{B} \cdot \vec{H} \right) dA. \tag{2.68}$$

Assuming a small perturbation in relative permittivity is introduced, the change in effective index will be given by the change in electric energy density Δu_E:

$$\Delta n_{eff} = n_{eff,p} - n_{eff,a} = \int_A u_{E,p} - u_{E,a} dA = \int_A \Delta u_E dA. \tag{2.69}$$

In terms of electric fields, this is equivalent to:

$$\Delta n_{eff} = \int_A \Delta u_E dA = \frac{c}{2} \int_A \Delta n^2(\vec{r}) \left| \vec{E}(\vec{r}) \right|^2 dA = \frac{c}{2} \int_A \Delta \vec{D}(\vec{r}) \vec{E}^*(\vec{r}) dA. \tag{2.70}$$

This result shows that the sensing potential of a given waveguide mode is best visualized using the electric energy density $u_E(\vec{r}) = \left(\vec{D}(\vec{r}) \cdot \vec{E}(\vec{r}) \right) / 2$, rather than either the $\vec{E}$ or $\vec{D}$ fields alone. A comparison of $\vec{E}(\vec{r})$, $\vec{D}(\vec{r})$, and $u_E(\vec{r})$ is seen in Figure 2.7.

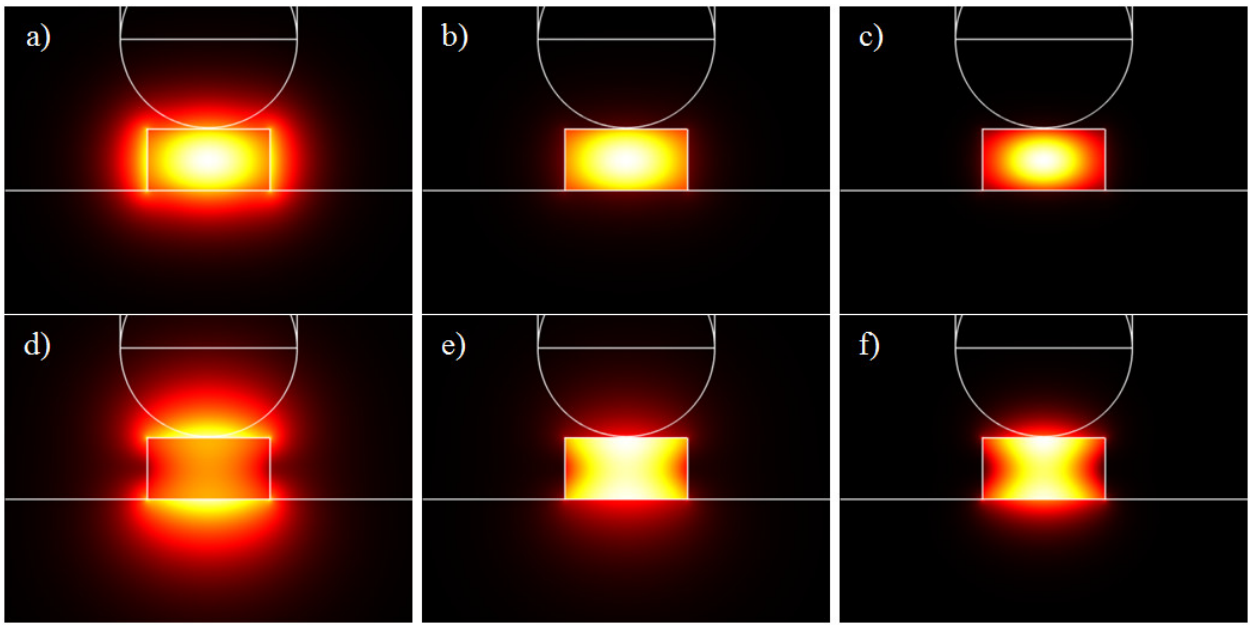

Figure 2.7. Comparison of cross-sectional mode profiles for TE (a-c) and TM (d-f) waveguide modes for electric field (a,d), electric displacement field (b,e) and electric energy density (c,f).

2.5.3. Microring cladding sensitivity

A ring resonator will respond to a change in the cladding refractive index Δn_c with a shift in the cavity wavelength $\Delta\lambda_m$, due to the change Δn_{eff} in the effective index of the propagating mode. For a given resonance m, through substitution of Eq. 2.50, the wavelength shift $\Delta\lambda_m$ will be given by:

$$\Delta\lambda_m = \lambda'_m - \lambda_m = \frac{L}{m}\left(n'_{eff}(\lambda'_m) - n_{eff}(\lambda_m)\right) = \frac{L}{m}\Delta n_{eff}, \tag{2.71}$$

where Δn_{eff} is:

$$\Delta n_{eff} = n'_{eff}(\lambda'_m) - n_{eff}(\lambda_m). \tag{2.72}$$

Using first order dispersion:

$$n'_{eff}(\lambda'_m) = n'_{eff}(\lambda_m) + \Delta\lambda_m \left.\frac{\partial n'_{eff}}{\partial\lambda}\right|_{\lambda_m}, \tag{2.73}$$

$$n'_{eff}(\lambda_m) = n_{eff}(\lambda_m) + \Delta n_c \left.\frac{\partial n_{eff}}{\partial n_c}\right|_{\lambda_m}. \tag{2.74}$$

Substitution of Eq. 2.73 and Eq. 2.74 into Eq. 2.72 reveals that:

$$\Delta n_{eff} = \Delta n_c \left.\frac{\partial n_{eff}}{\partial n_c}\right|_{\lambda_m} + \Delta\lambda_m \left.\frac{\partial n'_{eff}}{\partial \lambda}\right|_{\lambda_m}, \tag{2.75}$$

The total effective index shift is thus a result of both the refractive index change in the cladding Δn_c and the total dispersion (including both material and waveguide dispersion) experienced by the mode.

Substituting the expression for Δn_{eff} from Eq. 2.75 into Eq. 2.71 and solving for $\Delta\lambda_m$ shows:

$$\Delta\lambda_m = \frac{\Delta n_{clad} \left.\frac{\partial n_{eff}}{\partial n_c}\right|_{\lambda_m}}{\left(\frac{m}{L} - \left.\frac{\partial n'_{eff}}{\partial \lambda}\right|_{\lambda_m}\right)}, \tag{2.76}$$

and using $m/L = n'_{eff}/\lambda'_m$:

$$\Delta\lambda_m = \frac{\lambda'_m \Delta n_{clad} \left.\frac{\partial n_{eff}}{\partial n_c}\right|_{\lambda_m}}{\left(n'_{eff} - \lambda'_m \left.\frac{\partial n'_{eff}}{\partial \lambda}\right|_{\lambda_m}\right)}. \tag{2.77}$$

Recognizing the denominator as the group refractive index from Eq. 2.6 for the ring mode:

$$\Delta\lambda_m = \frac{\lambda'_m}{n'_g} \cdot \Delta n_{clad} \left.\frac{\partial n_{eff}}{\partial n_c}\right|_{\lambda_m}. \tag{2.78}$$

The ring resonator cladding sensitivity $S_{c,RR}$, or the sensitivity of the ring resonant wavelength to a homogenous change in the refractive index of the cladding, may then be defined:

$$S_{c,RR} = \frac{\Delta\lambda_m}{\Delta n_c} = \frac{\lambda'_m}{n'_g} \cdot \left.\frac{\partial n_{eff}}{\partial n_c}\right|_{\lambda_m} = \frac{\lambda'_m}{n'_g} \cdot S_{c,WG}, \tag{2.79}$$

where $S_{c,WG}$, from Eq. 2.64, is the waveguide cladding sensitivity of the curved ring waveguide.

In typical sensing applications, relatively small changes in refractive index are of interest, which will cause small changes in both wavelength and dispersion. For such a case, $\lambda_m' / n_g' \simeq \lambda_m / n_g$ and Eq. 2.79 will be equivalent to:

$$S_{c,RR} = \frac{\Delta\lambda_m}{\Delta n_{clad}} = \frac{\lambda_m}{n_g} \cdot S_{c,WG}. \tag{2.80}$$

Thus, in the case of homogeneous refractive index changes of the overcladding, the ring resonator cladding sensitivity $S_{c,RR}$ is simply the product of the ring's waveguide cladding sensitivity $S_{c,WG}$ and the ratio of the ring mode wavelength λ_m to the group index n_g of the ring mode.

3. THEORETICAL CONSIDERATIONS FOR DISCRETE ANALYTE SENSING

3.1. Motivation for discrete analyte sensitivity

Microring resonator sensors capitalize on the high sensitivity of ring resonators to small changes of and around the cavity. This motivates their exploration as sensors of discrete biological analytes, such as bacteria, viruses, protozoa, or proteins, beyond the more straightforward case of homogeneous cladding changes due to a change in cladding fluid. For the purposes of this work, "discrete" refers to individual analytes that interact with the ring inhomogeneously around the ring circumference. In the case of an excess of analytes, it describes the sensing behavior of the ring prior to the saturation of the sensing response. Once the ring is saturated around its circumference, the derivation in this chapter will become equivalent to the commonly used cladding sensitivity of Eq. 2.80.

3.2. Derivation of ring resonator discrete analyte sensitivity

Generalizing Eq. 2.50, the ring resonant wavelength in a reference (or unperturbed) case with no analytes present is given by:

$$\lambda_m = \frac{OPL}{m} = \frac{1}{m}\oint_L n_{eff,m}(\lambda_m, \varphi) d\ell = \frac{L n_{eff}(\lambda_m)}{m}, \tag{3.1}$$

where m is the number of mode wavelengths present in the ring during resonance, λ_m is the resonant vacuum wavelength of the ring at resonance m, OPL is the optical path length of the ring, $n_{eff}(\lambda_m)$ is the effective index of the guided mode at cross-section φ around the ring, and L is the ring circumference (secondary effects such as the change of effective index at the coupling region with a straight waveguide are neglected).

In the presence of an analyte, the effective index of the ring mode near the analyte will be changed due to the evanescent field of the resonant mode interacting with the analyte. For theoretical derivation, we assume b identical present analytes with uniform refractive index. In the cross-section of the ring, the analytes are taken to have uniform size, shape, and location, and a length

of ℓ_φ in the φ direction (parallel to the ring curvature). This derivation can be trivially expanded to the more general case of bindings of analytes with nonuniform refractive index, size, and shape by replacing with ℓ_φ with $\ell_{ea,\varphi}$, the average effective analyte length in the circumferential φ direction.

The new resonance wavelength in response to the bound analytes will be:

$$\lambda_m' = \frac{1}{m}\left(\int_{L-b\ell_\varphi} n_{eff,m}(\lambda_m', \varphi) d\ell + \int_{b\ell_\varphi} n_{eff,m}'(\lambda_m', \varphi) d\ell \right) = \frac{[L - b\ell_\varphi] n_{eff}(\lambda_m') + b\ell_\varphi n_{eff}'(\lambda_m')}{m}, \quad (3.2)$$

where the primed symbols denote new values (presence of analytes) and the unprimed symbols denote baseline values (absence of analytes). Defining the new resonance as $\lambda_m' = \lambda_m + \Delta\lambda_m$, waveguide dispersion is accounted for by:

$$n_{eff}(\lambda_m') = n_{eff}(\lambda_m) + \left.\frac{\partial n_{eff}}{\partial \lambda}\right|_{\lambda_m} \Delta\lambda_m, \quad (3.3)$$

$$n_{eff}'(\lambda_m') = n_{eff}'(\lambda_m) + \left.\frac{\partial n_{eff}'}{\partial \lambda}\right|_{\lambda_m} \Delta\lambda_m = n_{eff}(\lambda_m) + \Delta n_{eff}(\lambda_m) + \left.\frac{\partial n_{eff}'}{\partial \lambda}\right|_{\lambda_m} \Delta\lambda_m, \quad (3.4)$$

where $\Delta n_{eff}(\lambda_m) = n_{eff}'(\lambda_m) - n_{eff}(\lambda_m)$. Substitution from Eqs. 3.3 and 3.4 into Eq. 3.2 demonstrates the resonant wavelength shift to be:

$$\Delta\lambda_m = \lambda_m' - \lambda_m = \frac{\frac{b\ell_\varphi}{L}\Delta n_{eff}(\lambda_m)}{\frac{m}{L} - \left(1 - \frac{b\ell_\varphi}{L}\right)\cdot\left.\frac{\partial n_{eff}}{\partial \lambda}\right|_{\lambda_m} - \frac{b\ell_\varphi}{L}\cdot\left.\frac{\partial n_{eff}'}{\partial \lambda}\right|_{\lambda_m}}. \quad (3.5)$$

Assuming $b\ell_\varphi << L$, substitution from Eq. 3.1 with $m/L = n_{eff}(\lambda_m)/\lambda_m$ gives:

$$\Delta\lambda_m = \frac{\frac{b\ell_\varphi}{L}\lambda_m \Delta n_{eff}(\lambda_m)}{n_{eff}(\lambda_m) - \lambda_m\left[\left.\frac{\partial n_{eff}}{\partial \lambda}\right|_{\lambda_m} + \frac{b\ell_\varphi}{L}\left(\left.\frac{\partial n_{eff}'}{\partial \lambda}\right|_{\lambda_m} - \left.\frac{\partial n_{eff}}{\partial \lambda}\right|_{\lambda_m}\right)\right]}. \quad (3.6)$$

From Eq. 2.6, the denominator is recognized to have the form of group refractive index, $n_g = n_{eff}(\lambda_m) - \lambda_m(\partial n_{eff}/\partial\lambda)$. The analytes are assumed to have minimal contribution to n_g due to a low dispersion difference between typical biological analytes and the overcladding liquid, which is further reduced assuming a small portion of the ring circumference has analytes present. The denominator is then approximated by the conventional definition of group index:

$$n_g(\lambda_m) \approx n_g(\lambda_m) - \lambda_m \cdot \frac{b\ell_\varphi}{L}\left[\left(\left.\frac{\partial n'_{eff}}{\partial\lambda}\right|_{\lambda_m} - \left.\frac{\partial n_{eff}}{\partial\lambda}\right|_{\lambda_m}\right)\right] \tag{3.7}$$

The resulting ring resonance wavelength shift per bound analyte can then be defined as a ring resonator discrete analyte sensitivity $S_{d,RR}$:

$$S_{d,RR} \equiv \frac{\Delta\lambda_m}{b} = \frac{\ell_\varphi}{L} \cdot \frac{\Delta n_{eff}(\lambda_m)}{n_g(\lambda_m)/\lambda_m}. \tag{3.8}$$

It is apparent from Eq. 3.8 that the ratio ℓ_φ/L strongly modulates the resonator sensitivity to discrete analytes. This is a trait unique to detection of discrete objects of significant size [78] [79], as opposed to detection of homogeneous refractive index changes from a cladding liquid or sensing the concentration of objects in an aqueous solution with size too small to be resolved [16] [17] [18] [19] [26] [27] [28] [80] [81].

This derivation differs from the case of uniform bulk refractive index sensing as discussed in Section 2.5.3 from the use of $b\ell_\varphi < L$. If $b\ell_\varphi = L$, and the substitution from Eq. 3.1 into Eq. 3.5 is replaced with $m/L = n_{eff}(\lambda_m)/\lambda_m$, the result will rearrange to the definition of homogeneous ring resonator cladding sensitivity seen in Eq. 2.80, $S_{c,RR} = \Delta\lambda_m/\Delta n_{clad}$. Therefore, the discrete analyte case describes the sensing response of a ring between the limit of no analytes and a ring fully saturated with bound analytes. In this regime, and unlike cladding sensitivity, the sensitivity of the ring is inversely proportional to the size of the ring. Homogeneous cladding sensitivity is independent of ring size.

Eq. 3.8 can be further generalized by reframing it in terms of a change in bound analytes ($b \rightarrow \Delta b$) and the sensed analyte optical size (more formally, the wavelength normalized optical perturbation size) given by $\ell_\varphi \Delta n_{eff}(\lambda_m)/\lambda_m$:

$$S_{d,RR} = \frac{\Delta\lambda_m}{\Delta b} = \left(\frac{\ell_\varphi \Delta n_{eff}(\lambda_m)}{\lambda_m} \right) \cdot \frac{\lambda_m{}^2}{Ln_g(\lambda_m)} = \left(\frac{\ell_\varphi \Delta n_{eff}(\lambda_m)}{\lambda_m} \right) \cdot \Delta\lambda_{FSR} \tag{3.9}$$

with the definition of $\Delta\lambda_{FSR}$ recognized from Eq. 2.60. This form suggests a practical way of comparing the $S_{d,RR}$ (hereafter denoted simply as S_d) of different ring designs. The sensed analyte optical size for a given design can be simulated computationally, and the $\Delta\lambda_{FSR}$ can either be extracted computationally or through experiment.

3.3. Derivation of discrete analyte sensing figure of merit

Sensing performance depends on both the achievable resonant shift and measured linewidth of the resonant cavity [80] [82]. To account for this, we use as a sensing figure of merit (*FOM*) the ratio of analyte induced resonant shift to the resonant peak full width at half maximum (*FWMH*, Eq. 2.57) [83]. *FOM* relates to the intrinsic sensor limit of detection $LOD_i = \lambda_m/(Q_L S)$ [75] by $FOM = 1/LOD_i$.

If the analyte does not significantly change resonator loss ($\alpha_{analyte} << \alpha_{total}$) and that the resonant shift is small compared to the center wavelength, this situation is described equivalently by the expressions:

$$FOM \equiv \frac{\Delta\lambda_m}{\Delta\lambda_{FWHM}} = \Delta\lambda_m \frac{F}{\Delta\lambda_{FSR}} = \frac{\Delta\lambda_m}{\lambda_m} Q, \tag{3.10}$$

where F is the ring finesse (Eq. 2.61), $\Delta\lambda_{FSR}$ is the free spectral range (Eq. 2.60), and Q (Eq. 2.55) is the measured loaded Q of the resonator. An *FOM* of one corresponds to a shift wavelength shift equal to the *FWHM* of the resonance, as show below in Figure 3.1 for an O-band centered resonator.

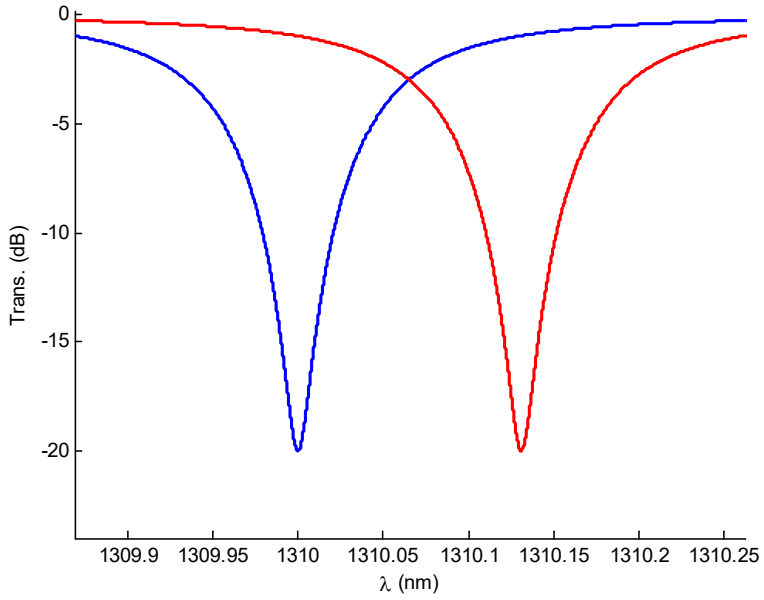

Figure 3.1. Graphical demonstration of a sensing figure of merit equal to one (*FOM*=1), a wavelength shift equal to the resonance full width at half maximum.

Normalized to a single bound analyte, the discrete analyte sensing figure of merit FOM_d is similarly defined as:

$$FOM_d \equiv \frac{S_d}{\Delta\lambda_{FWHM}} = \frac{S_d}{\Delta\lambda_{FSR}} \cdot F = \frac{S_d}{\lambda_m} \cdot Q. \tag{3.11}$$

From the definition of *FWHM* in Eq. 2.57, this relationship (using $\Delta n_{eff}(\lambda_m) = \Delta n_{eff}$ for compactness), is equivalent to:

$$FOM_d : \frac{S_d}{\Delta\lambda_{FWHM}} = \left(\frac{\ell_\varphi \Delta n_{eff}}{\lambda_m}\right) \cdot \frac{2\pi}{\alpha L} = \ell_\varphi \Delta n_{eff} \frac{k_0}{\alpha L} = \frac{\ell_\varphi \Delta n_{eff}}{2\kappa L}. \tag{3.12}$$

Recognizing the definition of finesse from Eq. 2.61, FOM_d is equivalently expressed as:

$$FOM_d \equiv \left(\frac{\ell_\varphi \Delta n_{eff}}{\lambda_m}\right) \cdot F \tag{3.13}$$

From this representation, the discrete analyte sensing figure of merit FOM_d is the product of the cavity finesse F and the sensed analyte optical size (the optical path perturbation due to the bound

analyte normalized to the operating wavelength). The dependence on finesse instead of simply on the more commonly considered quality factor is similar to applications relying on high $Q/V = (F/A_{eff})\cdot(n_g/\lambda_m)$ [84] [85], where V is the mode volume and A_{eff} is the cross-sectional mode area. Though not considered here, the derived *FOM* similarly applies to detection of discrete analytes by other optical ring resonator geometries such as microracetracks, though the specifics of Δn_{eff} may lead to complicated results.

3.4. Design considerations overview

To obtain a maximally sensitive cellular biosensor with the goal of single bacterial analyte resolution, we focus in this section on maximizing sensitivity for the case of a single cell bound to a small radius ring. It is apparent from Eq. 3.13 that maximum sensitivity results from maximized $\ell_\varphi \Delta n_{eff}/\lambda_m$, and F (i.e. minimized αL). We consider the rod shaped bacteria *E. coli* [86], so the actual analyte size and shape of analytes be similar among the individual analytes. However, ℓ_φ will depend on the particular geometry of cell to ring binding, as well as on the degree of modal delocalization of the ring mode. Thus, we consider a range of potential likely binding geometries to evaluate sensing response for all likely cases.

Table 3.1. Properties of aqueous clad single mode waveguides in large (100 μm) radius rings.

λ (nm)	α_{H2O} (dB/cm)	Waveguide (HxW)	Mode Pol.	$\mathbf{Q_{i,H2Oabs}}$	$\alpha_{m,H2O}$ (dB/cm)	n_{eff}	n_{g+}	$\frac{\partial \lambda_m}{\partial T}$ (pm/K)	$\frac{\partial n_{eff}}{\partial n_c}$ (S_{wg})	$\frac{\partial \lambda_m}{\partial n_c}$ ($S_{RR,n}$)
1550	46.5	Si, 220 x 500 nm	TM	**28,050**	23.6	1.702	3.757	49	0.497	205
1550	46.5	Si, 220 x 500 nm	TE	**105,100**	7.1	2.426	4.239	75	0.148	54
1550	46.5	SiN, 500 x 1100 nm	TM	**36,380**	10.5	1.599	2.059	15	0.207	156
1550	46.5	SiN, 500 x 1100 nm	TE	**60,800**	7.0	1.669	2.085	17	0.130	96
1310	6.68	Si, 220 x 350 nm	TM	**354,100**	2.8	1.955	4.741	52	0.403	111
1310	6.68	Si, 220 x 350 nm	TE	**674,100**	1.4	2.403	4.566	61	0.202	58
1310	6.68	SiN, 500 x 850 nm	TM	**392,800**	1.0	1.647	2.111	14	0.167	103
1310	6.68	SiN, 500 x 850 nm	TE	**511,400**	0.7	1.692	2.115	15	0.129	80

3.4.1. Waveguide material

Both Si and SiN are considered for waveguide materials. The high refractive index of silicon allows for high Q operation at very small radii [15], which is beneficial for maximizing F. The large index contrast also results in a large electric field directly outside the waveguide [87]. However, the lower refractive index of SiN means lower index contrast with H_2O and a more delocalized mode. This is potentially advantageous for maximizing Δn_{eff} for relatively large bacterial analytes. Additionally, SiN waveguides have achieved much higher Q than that achievable in Si, albeit typically with oxide cladding and very large radii [13]. Furthermore, SiN has a thermo-optic coefficient [88] [89] [90] an order of magnitude lower than silicon, making them less sensitive to environmental changes in temperature as shown in Table 3.1.

3.4.2. Mode polarization

Optical microresonator sensors often operate in the more delocalized TM polarization instead of the higher Q TE mode commonly used in most other applications [9]. However, we consider the TE mode here for optimization purposes due to the significantly lower radiation loss for small bending radii compared to the TM mode [91]. Additionally, as the modal distribution of the TE mode is concentrated on the sides of the waveguide, we consider the possibility that TE modes are more sensitive to certain analyte-to-ring binding geometries.

3.4.3. Mode wavelength

The C-band near 1550 nm is the standard wavelength for microring resonators due to the availability of amplification from EDFAs and low loss in silica fibers [9], but suffers from the high absorption of water [20] [21] necessary as an overcladding in many sensing applications. This motivates consideration of the O-band near 1310 nm, which offers the lowest H_2O absorption [74] available in silicon's transparency window. The limiting Q of large microrings due to H_2O absorption is seen in Table 3.1. A shorter wavelength also allows for smaller radii rings without significant bend induced radiation loss, potentially enabling larger F. While FOM_d directly depends on wavelength, the major contribution will be a result of the achievable F at a given λ_m.

3.4.4. Delocalization and cavity loss

High F results from a small cavity with low loss, with maximum F depending on the interplay of radius and radius dependent losses with radius independent losses. Total loss is a result of scattering, bending, and water absorptive losses. While absorption and bending losses may be computationally explored, scattering loss is entirely fabrication dependent. As it is the dominant loss source between the bending and absorption limited extremes, fabricated devices are required for estimation of achievable F. Computational investigation and design will thus initially focus on maximizing Δn_{eff} by encouraging waveguide modal delocalization, while being mindful that delocalization will tend to increase loss. To this end, this investigation includes the design parameters of waveguide material, mode polarization, wavelength band, and waveguide dimension.

3.4.5. Waveguide dimension

Varying the waveguide dimension can be used to promote modal delocalization to increase both ℓ_φ and Δn_{eff}. However, this tends to result in increased α due to scattering and bend losses and will increase the effect of water absorption. Modal delocalization will also vary significantly with different waveguide materials, mode polarizations, and wavelength, necessitating a full study of the achievable Δn_{eff} for each.

3.5. Conclusions from theoretical considerations

3.5.1. Comparison of cladding sensitivity and discrete analyte sensing equations

The preceding derivation of ring resonator sensitivity to detection of individual objects of discrete size has revealed that this case differs from the commonly used equations for cladding sensitivity. A summary of these relationships can be seen in Table 3.2 (note: equations for cladding sensing figure-of-merit and discrete analyte waveguide sensitivity were trivially derived from the previous equations). Cladding sensing depends only on $S_{c,WG}$, λ, n_g, and Q, making it a relatively straight forward case to analyze with clear focuses ($S_{c,WG}$ and Q) for optimization.

Discrete analyte sensing is a more complicated situation. Sensed analyte optical size ($\ell\Delta n_{eff}/\lambda$) depends on analyte specifics and binding location and will require substantial simulation for

optimization. Unlike cladding sensing, discrete analyte sensing depends on the size of the cavity. Sensitivity will be optimized by minimizing L (maximizing $\Delta\lambda_{FSR}$), but after a point this will substantially increase radiation losses and degrade resonance linewidth. The tradeoff between L and losses is accounted for by optimizing for cavity finesse (F) instead of the more typical quality factor Q. While finesse is a well-known quantity, it has not been utilized as a critical figure-of-merit for sensing applications.

Table 3.2. Summary of sensing qualities for cladding and discrete analyte sensing.

Sensing Type	**Quality**	**Equation**	**Units**
Cladding Sensing	Waveguide Sensitivity	$S_{c,WG} = \frac{\partial n_{eff}}{\partial n_c}$	Unitless
Cladding Sensing	Ring Resonator Sensitivity	$S_{c,RR} = \frac{\partial \lambda}{\partial n_c} = S_{c,WG} \cdot \frac{\lambda}{n_g}$	nm/RIU
Cladding Sensing	Sensing Figure-of-Merit	$FOM_c = \frac{S_{c,RR}}{\Delta\lambda_{FWHM}} = S_{c,WG} \cdot \frac{2\pi}{\alpha\lambda} = S_{c,WG} \cdot \frac{Q}{n_g}$	1/RIU
Discrete Analyte Sensing	Waveguide Sensitivity	$S_{d,WG} = \frac{\partial n_{eff}}{\partial b} = \frac{\ell}{L} \cdot \Delta n_{eff} = \left(\frac{\ell \Delta n_{eff}}{\lambda}\right) \cdot \frac{\lambda}{L}$	RIU/ analyte
Discrete Analyte Sensing	Ring Resonator Sensitivity	$S_{d,WG} = \frac{\Delta\lambda}{\Delta b} = S_{d,WG} \cdot \frac{\lambda}{n_g} = \left(\frac{\ell \Delta n_{eff}}{\lambda}\right) \cdot \frac{\lambda^2}{n_g L} = \left(\frac{\ell \Delta n_{eff}}{\lambda}\right) \cdot \Delta\lambda_{FSR}$	nm/ analyte
Discrete Analyte Sensing	Sensing Figure-of-Merit	$FOM_d = \frac{S_{d,RR}}{\Delta\lambda_{FWHM}} = \left(\frac{\ell \Delta n_{eff}}{\lambda}\right) \cdot \frac{2\pi}{\alpha L} = \left(\frac{\ell \Delta n_{eff}}{\lambda}\right) \cdot F$	Per analyte

3.5.2. Sensor optimization procedure

The clear dependence on ring size (as either R, L, or the size dependent F) of the discrete analyte sensitivity motivates exploring minimally size sensors. Minimizing the size of a sensor to increase its sensitivity has been previously explored for whispering gallery mode sensors [92] because their sensitivity depends on sensor size even for the case of cladding sensitivity. Alone, however, size minimization is generally [93] not considered a fruitful procedure for practical devices. Although more sensitive, the available sensing area/volume is also reduced proportional to the increase in sensor resolution. Ultimately, the detection of a single analyte is not of interest, rather it is the detection of a concentration of analytes, typically expressed as analytes per unit volume (e.g. analytes/mL).

An increase in concentration sensitivity requires an increase in sensor resolution while maintaining or increasing the sensing volume. The analysis here suggests a way to do exactly that. Finesse, as will be seen later, is a direct quantification of the multiplexing ability of a ring. Multiplexing multiple sensors onto a single waveguide will increase the effective sensing volume of the array, allowing for a true sensitivity increase to discrete analytes. This differs from the case of homogenous cladding sensitivity. As homogenous cladding sensitivity is independent of sensor size, multiplexing sensors may provide redundancy and a potential avenue to detect multiple "channels" on a single waveguide, but will have no effect on sensitivity.

The approach in this work is to follow a two-step plan to optimize sensitivity to discrete analytes:

1. Optimize S_d: Optimize the sensor resolution of a ring to a particular biological analyte such that the ring will detect a single analyte in all potential binding scenarios.
2. Optimize FOM_d: Multiplex as many optimized rings as possible into a sensing array, thereby increasing the sensing volume.

A maximally multiplexed array of rings, each of which can detect down to a single bound cell, then represents an optimized ring resonator sensor for that analyte. No further sensitivity increase beyond single cell resolution sensitivity would be useful, and a maximally multiplexed array will have as many devices as possible with a given set of fabrication procedures. Additionally, because of the size dependence, the sensitivity of an array can be decreased by increasing the size of the

sensors (e.g. by N), and multiplexing fewer of them ($1/N$ times as many rings). This can effectively create a way to control the dynamic range of a device to from the maximally sensitive case up to as insensitive as is desired.

3.5.3. Summary

In summary, optimal sensing performance of the microring resonator for single cell resolution sensing depends on how the interplay of the microring material, structural, and modal parameters affect Δn_{eff}, F, and ℓ_{φ}. For practical sensing performance, a sensor with a large resonant shift and small radius, while still maintaining a Q large enough to clearly measure a wavelength shift, is desired. Computational investigation will focus on maximizing the effective index difference Δn_{eff} due to a single bound cellular analyte in a comprehensive exploration of binding situations. Finesse is considered, but due to the large contribution of fabrication induced scattering losses in real ring resonators, fabricated devices will be necessary to determine the optimal ring size/finesse.

4. MODELING OF DISCRETE ANALYTE SENSING

4.1. Development of a cross-sectional model

The inherent 3D nature of the microring resonator structure requires a full-wave 3D electromagnetic simulation of the device to predict overall performance through the sensing *FOM*. This was achieved in steps, beginning with a simplified 2D simulation of a waveguide cross-section to optimize those parameters uniform in the cross-section of the microring. The results from these simulations were then extended to a full 3D model to accurately model the entire sensing scheme. We begin with the analysis of the shift in effective mode index which results from the electric field interacting with a single cellular analyte. A 2D cross-section was used to explore the effect of the waveguide material and geometry, mode polarization, and wavelength. A straight waveguide cross-section was used at this stage to approximate the curved ring mode. Compared with full 3D COMSOL Multiphysics simulation which automatically considers the mode drift, the discrepancies between the two are small.

Using a 2D finite element model in COMSOL, a straight waveguide was modeled with and without a bound bacterial cell. Four different binding scenarios (shown in Figure 4.1) were considered to account for a full range of possible methods of analyte to waveguide binding. The model consists of a SiO_2 substrate, a Si or SiN waveguide, and a single cellular analyte surrounded by H_2O. For accurate field distribution calculation, a finite element mesh with minimum $\lambda_0/300$ and maximum $\lambda_0/100$ element sides were used in the simulation. Refractive index values for Si [94], SiN [95], SiO_2 [96], and H_2O [97] were obtained from Sellmeier coefficients [98]. Wavelength specific absorption from H_2O was included as a separate polynomial fit over each separate wavelength band as the extinction coefficient $\kappa = \mathrm{Im}(\tilde{n}) = \lambda_0 \alpha_{abs} / (4\pi)$. The material absorption limited Q of Si, SiN, and SiO_2 is lower than that of H_2O by multiple orders of magnitude for the considered wavelengths and was neglected. The native oxide layer ~1 nm thick present on silicon surfaces [99] was also neglected, as its inclusion changed effective index values by <0.1%.

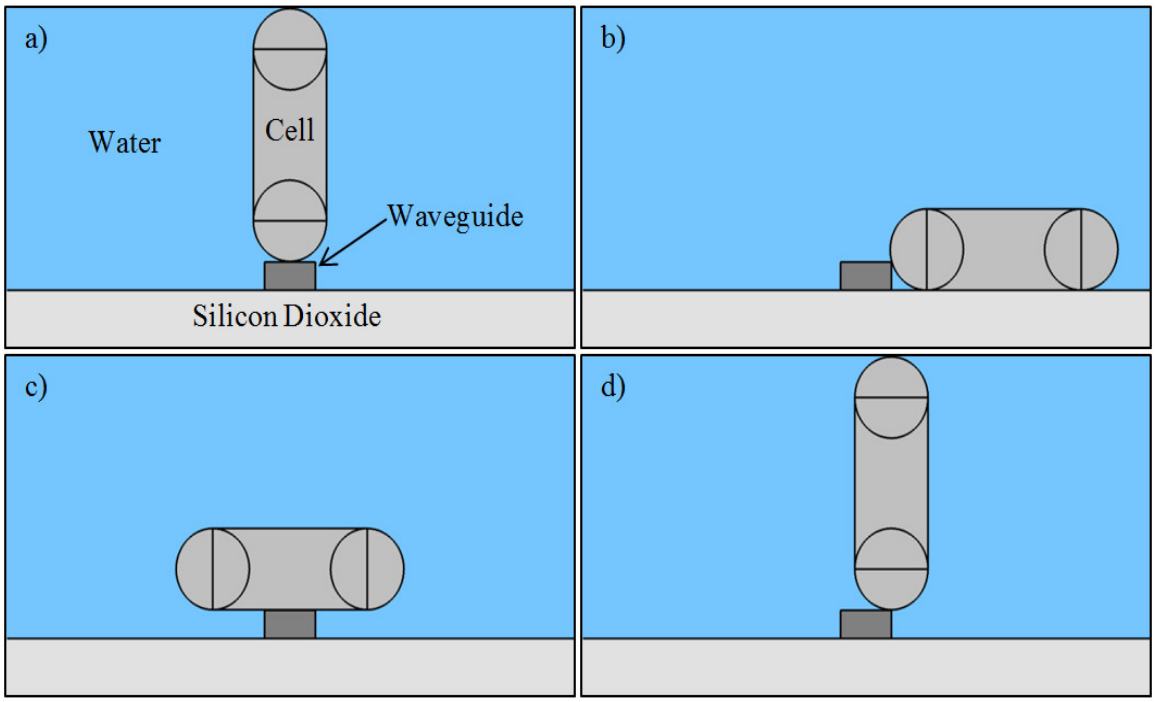

Figure 4.1. Cross-sectional models of ring and bound cell in the following binding geometries: Top (a), Side (b), Tee (c), and Corner (d).

The physical and spectral characteristics of the rod-shaped *E. coli*. [86] (K12 strain) are used as a typical model bacterium in the design of the simulations. The cell is simulated as a spherocylinder (cylinder with hemispherical caps on each end) with volume $V = \pi r^2(4r/3 + l) \approx 1.1$ fL, length $l =$ 2.24 µm, radius $r = 0.36$ µm, and refractive index described by a Cauchy relation [86] over the NIR, with $n_{1550nm} = 1.3885$ and $n_{1310nm} = 1.3879$. The size parameters used are conservative, and corroborated by a variety of sources [100] [101] [102] [103]. *E. coli* is typical in size and structure for rod shaped bacteria [104], and the hemispherical ends offer a typical model of spherical bacteria [105] as well. Due to the fast falloff of the waveguide evanescent field, the cellular volume within one cellular radius of the waveguide contributes nearly the totality of the cellular optical path length difference due to the cell. As a result, the model will apply generally to many different bacterial analytes.

In all binding scenarios, the cell was placed at a binding distance of 5 nm corresponding with the use of single domain antibodies (sdAbs) [106] for a minimal binding gap with selective surface chemistry. SdAbs possess a long shelf life and can withstand high temperatures. Their ability to

refold after heat or chemical induced denaturing makes them of particular interest for point of care biosensing applications, as a functionalized sensor surface could be reused numerous times. With dimensions of only 4 x 2.5 x 3.5 nm, compared that of full sized antibodies with dimensions of 15 x 7 x 3.5 nm [107], sdAbs enable a maximum field interaction with a bound cell while still maintaining chemical specificity. The effect of binding distance on the achievable effective index difference for waveguide geometries from Table 3.1 with a cell bound in the Top position from Figure 4.1(a) can be seen in Figure 4.3. Though the cross-sectional index shift is plotted, the speed of falloff and relative amplitude difference from total optical path difference remains essentially unchanged.

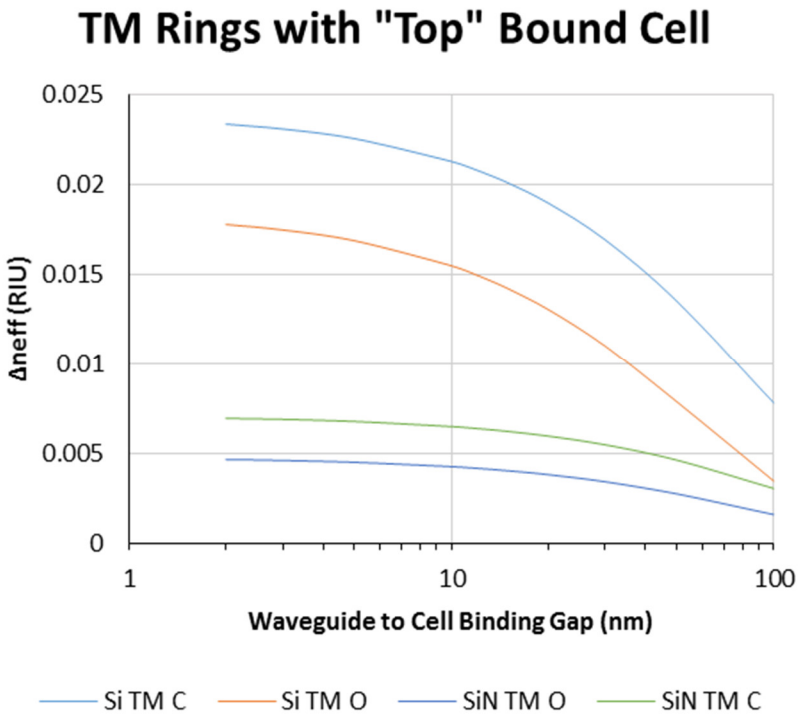

Figure 4.2. Effect of varying waveguide to cellular analyte binding distance for TM modes.

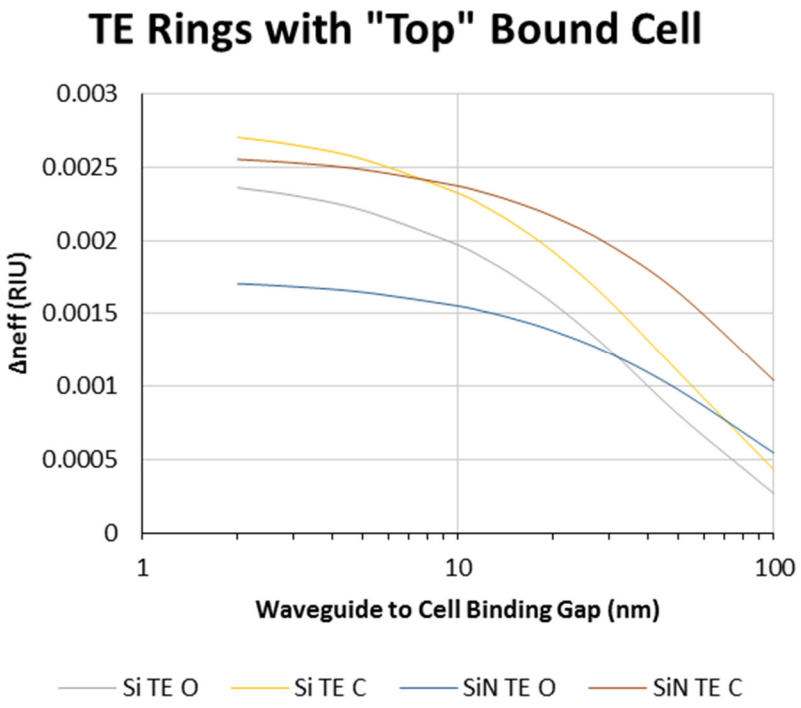

Figure 4.3. Effect of varying waveguide to cellular analyte binding distance for TE modes.

It can be seen that minimizing the binding gap corresponding to the use of sdAbs allows for the maximum Δn_{eff}. However, even conventionally sized antibodies would produce a sizeable index shift, and performance is only degraded by ~15-30% compared to the optimal case. It can also be seen that the reduced effective refractive index of a SiN waveguide leads to a smaller index shift close to the waveguide, but also a slower falloff with increasing distance from the waveguide.

To determine the effect of waveguide to bacterial analyte binding, both Si and SiN were simulated at TE and TM polarizations at wavelengths of 1310 nm (O-band) and 1550 nm (C-band). The waveguide dimensions used in the simulation for Si and SiN reflect the dimensions necessary for complete confinement of the mode in that material and were varied around those values. A comparison of the resulting index shifts is shown for the binding geometries considered in Figure 4.1: Top (Figure 4.4), Side (Figure 4.5), Tee (Figure 4.6), and Corner (Figure 4.7). The pure black squares indicate a waveguide geometry that either does not support a propagating mode or supports a mode that couples strongly into the SiO_2 substrate.

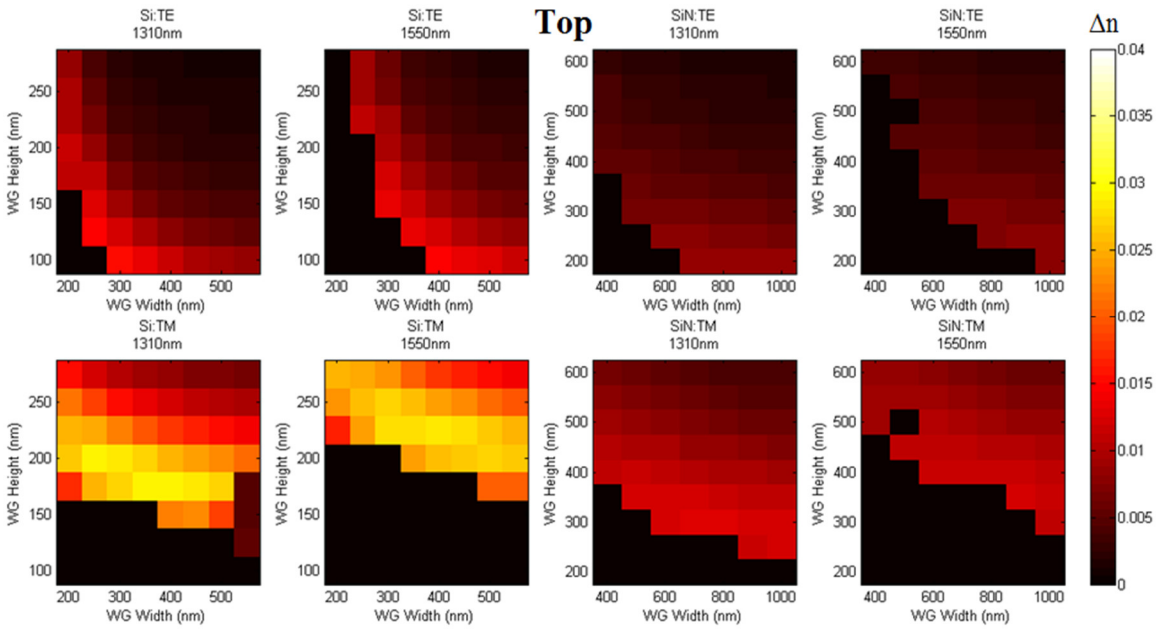

Figure 4.4. Cell binding-induced refractive index shifts as a function of material, dimension, and polarization for the Top binding geometry seen in Figure 4.1(a).

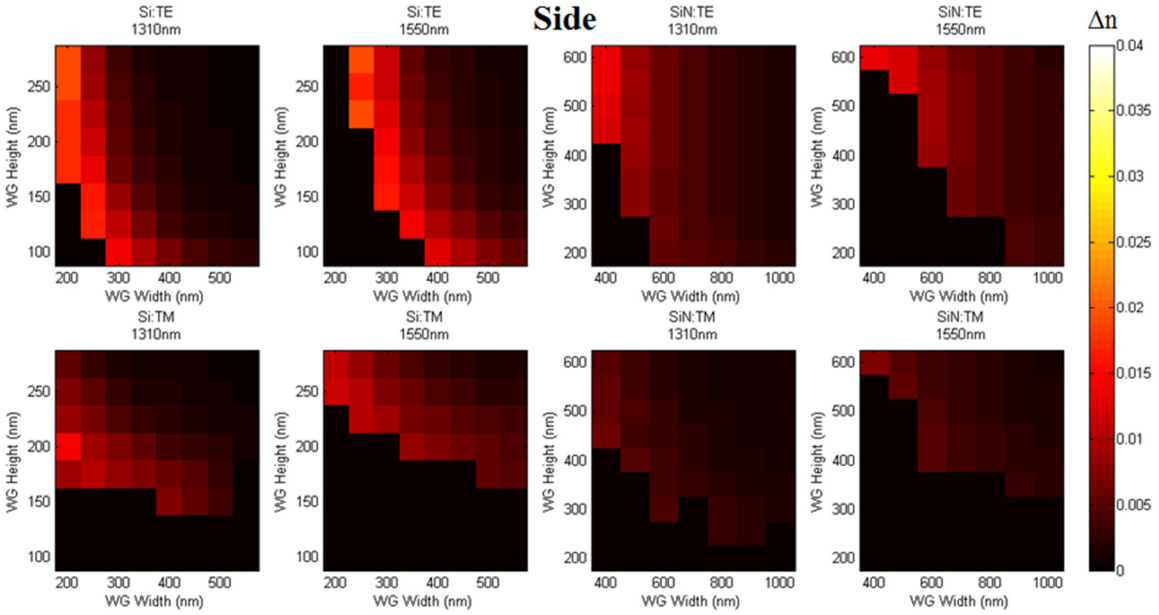

Figure 4.5. Cell binding-induced refractive index shifts as a function of material, dimension, and polarization for the Side binding geometry seen in Figure 4.1(b).

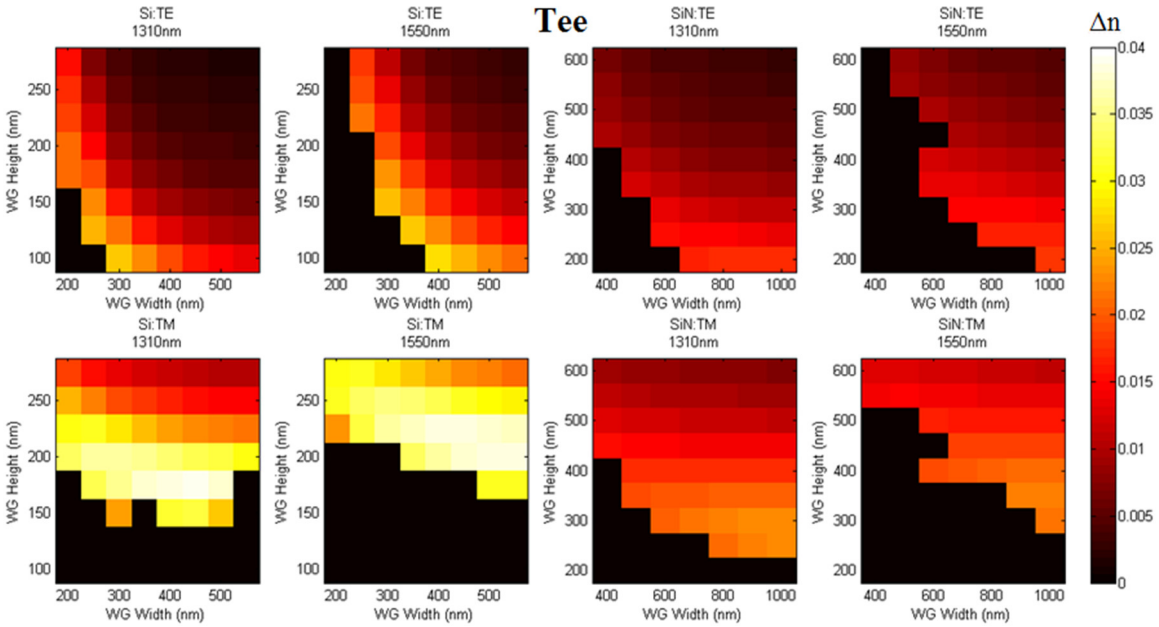

Figure 4.6. Cell binding-induced refractive index shifts as a function of material, dimension, and polarization for the Tee binding geometry seen in Figure 4.1(c).

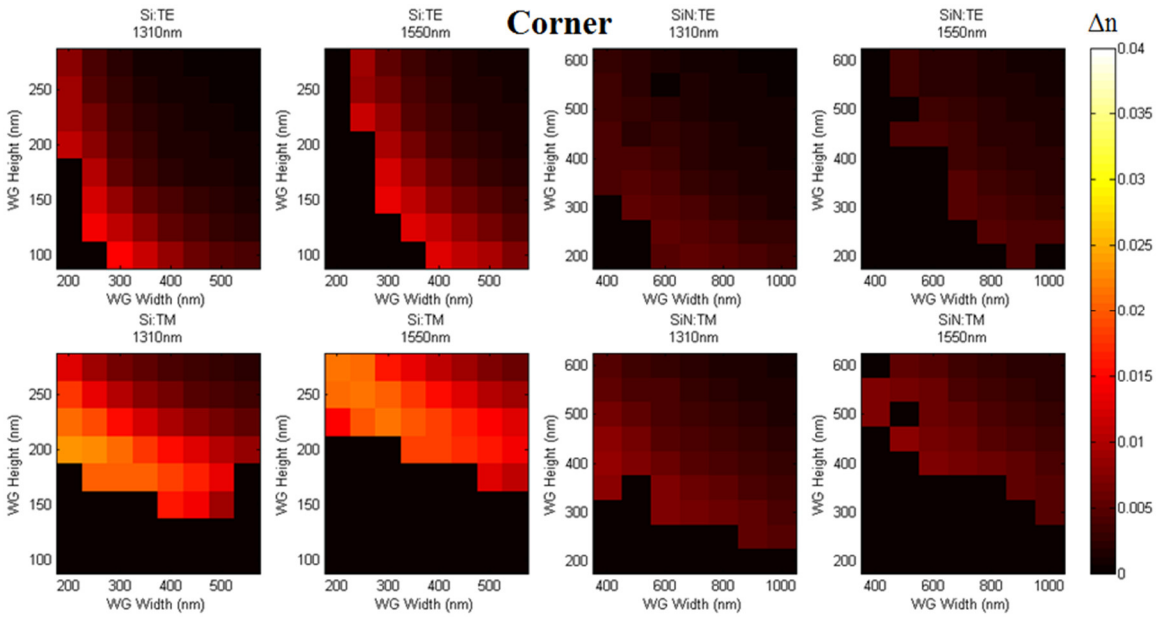

Figure 4.7. Cell binding-induced refractive index shifts as a function of material, dimension, and polarization for the Corner binding geometry seen in Figure 4.1(d).

Comparing polarizations, the TM mode offers an order of magnitude larger Δn_{eff} than the TE mode for both Si and SiN. Thus the 2-4 times lower losses (seen in Table 3.1) experienced by the TE

mode do not compensate for the decrease in sensitivity. Additionally, the TE mode only showed higher sensitivity to Corner binding for extreme aspect ratio waveguides. With respect to material, Si tends to offer ~2-3x higher Δn_{eff} than SiN for both the O and C-bands. Comparing performance between the wavelength bands, achievable Δn_{eff} is comparable if the waveguide dimensions can be reduced for the smaller wavelength O-band. However, the C-band does offer much higher Δn_{eff} for common Si heights of 220 nm and 250 nm, which could be beneficial depending on losses. Additionally considering losses and achievable F gives a complete picture of the sensing potential of each design possibility. A 2D axisymmetric COMSOL model was used to evaluate the intrinsic Q of rings limited by bending loss and water absorption. To avoid dispersive effects, the resonant wavelength was kept constant while m and R were varied.

Although decreasing the radius has the effect of increasing the effective index, it was found that the ratio of n_g/n_{eff} remained constant for a given wavelength to within a few percent even for extremely small rings ($m \leq 10$). As the ratio between Q and F (Eq. 2.62) is $Q/F = m \cdot n_g/n_{eff}$, F could be calculated using the essentially radius invariant ratio n_g/n_{eff} together with the simulated Q for a given m. Bend and absorption limited F for various radii TM rings with cross-sections from Table 3.1 are presented in Figure 4.8.

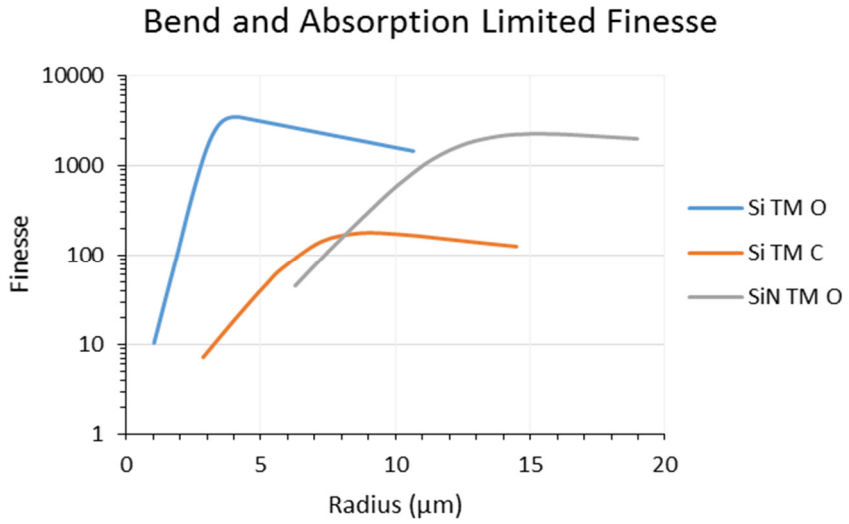

Figure 4.8. Achievable bend and absorption limited finesse for TM resonators.

As seen in Figure 4.8, for typical waveguide sizes, Si TM O-band rings can obtain higher ideal finesse compared to that of SiN TM O-rings. This is a result of the higher refractive index of Si compared to SiN, which allows for similar bending loss at much smaller radii. As the effective index shift in SiN was lower than that of Si, this implies that the overall *FOM* for SiN rings will lag behind that of Si rings, except perhaps in the case of ultrahigh *Q* SiN rings surpassing the scattering loss limited *Q* of Si. However, as ultrahigh *Q* SiN rings typically require very large radii, *F* would likely be degraded as well. Considering this, combined with the already 2-3x lower effective index shift of SiN, motivates the use of Si rings going forward. Additionally, the orders of magnitude lower losses in the O-band, combined with the fact that identical Δn_{eff} can be obtained, motivate the exploration of Si O-band rings over Si C-band rings.

Although the highest index shift for Si TM O-band rings is obtained from a waveguide ~175 nm x 450 nm in dimension, this will not necessarily result in the largest *FOM*. A high finesse relies on a low loss, minimally sized cavity. However, for the TM mode bending loss [46] can play a significant role in limiting the finesse. Bending loss scales as [46]:

$$\alpha_{bend} = K \exp\left(-\frac{2\pi R}{\lambda_m} \left[2\frac{n_{eff} - n_c}{n_{eff}} \right]^{3/2} \right), \tag{4.1}$$

meaning that for a given radius *R*, the effective index n_{eff} of the ring mode will play a dominant role in the loss experienced by the ring. The more highly delocalized modes of Figure 4.4 to Figure 4.7 will suffer a finesse degradation due to the lower index contrast that gives them a high sensitivity. The waveguide dimensions must therefore balance the achievable Δn_{eff} with the achievable *F* through the sensing *FOM* of Eq. 3.13. It would also be beneficial to operate at a waveguide dimension that offers single mode operation for each polarization. Higher order modes may have a higher loss and different sensitivity than the fundamental modes, making analysis of the ring transmission spectra more difficult. It was seen in Figure 4.4 to Figure 4.7 that waveguide height plays a much larger role than width for Δn_{eff}. Changing either will have a large effect on $n_{eff,}$ and the bending loss. Thus, for choosing waveguide dimensions, a given height can be selected, and the width can be increased as much as possible while still maintaining single mode operation.

A comparison of two different waveguide heights shows the maximum achievable finesse in Figure 4.9(a) for a corresponding radius in Figure 4.9(b) for different values of scattering limited Q. Note that the scattering limited intrinsic Q compounds the losses due to bending and absorption as seen in Figure 4.8. Although the 180 x 465 nm waveguide offers the highest Δn_{eff}, the slightly larger height waveguide of 220 x 350 nm offers 2-3 times the finesse for all $Q_{i,scat}$. As this comes at the expense of only ~30% less Δn_{eff}, the overall effect is a significantly increased FOM. This silicon height also corresponds with that widely available in SOI wafers, making it both a convenient and high-performance choice. Inspection of figure Figure 4.9(b) implies that best performance of a 220 x 350 nm ring lies within R=2.5 to 4 µm for a wide range of scattering losses.

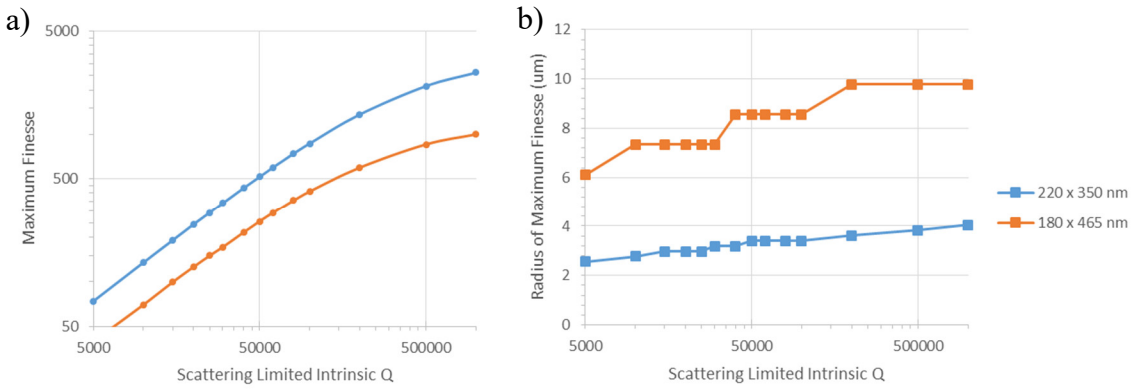

Figure 4.9. Maximum finesse (a, left) for a given radius (b, left) at different values of scattering limited intrinsic Q for TM O-band waveguides.

4.2. Three-dimensional ring model

To determine performance of a microring sensor, a 3D FEM COMSOL model of the ring was developed from the 2D cross-sectional model. Following the 2D analysis, investigation focused on Si TM rings in the O-band, with cross-sectional dimensions of 220 x 350 nm. Using the same refractive index and absorption parameters, 3D models corresponding to the various binding geometries in Figure 4.1 were created. An input/output waveguide was placed next to the ring such that the ring was coupled to the waveguide in an all-pass fashion, which has been shown to offer better Q values than alternative ring coupling setups [9]. A ring of radius 2.5 µm was selected as a balance between total ring circumference and experimentally achievable Q factor [15]. Focus

remained on achievable wavelength shift due to a single bound cell (S_d) as the ideal ring size to maximize F will strongly depend on scattering loss limit introduced by fabrication.

Performance was determined using simulations of the ring at different wavelengths, with and without the bacterial cell, and calculating the transmission spectra of the ring for each case. Perfectly matched layer (PML) boundary conditions were used to minimize reflection within the simulation domain. Mesh elements in the waveguide were set to a size of $\lambda_0/(10n_l)$ or smaller, with the remaining elements sized at least $\lambda_0/(6n_l)$ near the waveguide, and gradually decreasing to $\lambda_0/(5n_l)$ far from the waveguide (n_l indicating the local refractive index of the particular material in the mesh). The ring transmission spectra were determined using the ratio of the integral of the power contained in and around the input/output waveguide before and after the ring. The coupling gap was optimized for critical coupling to maximize extinction ratio.

The resulting wavelength spectra for the 2.5 μm ring before and after attachment of a cell in the In-Plane binding condition is seen in Figure 4.10. Both with and without the cell present, the loaded Q was found to be $Q_L \approx 23.2$k for the $m = 24$ mode nearest to 1310 nm. The lack of change in Q indicates minimal cell scattering losses compared to bending losses at this Q and radius. A wavelength shift of 728 pm was found for a single modeled *E. coli* in this "best case" binding scenario, which represents a $FOM_d = 13$ and $S_d = 728$ pm/cell. The response of the ring to the further range of binding scenarios can be seen in Table 4.1. For all binding scenarios, the loaded Q remained essentially unchanged at $Q_L \approx 23\text{k} \pm 1\text{k}$. Using 2D axisymmetric simulation to estimate n_g at 4.742, a finesse of 405 was found. This was used to calculate the sensed analyte optical size ($\ell_\varphi \Delta n_{eff}(\lambda_m)/\lambda_m$) due to the analyte through Eq. 3.13. Through a 2D cross-section, the sensing volume [108] in the ring cross-section was estimated to extend 305 nm above the waveguide top and 200 nm beyond the sides for the 1% definition, with a 1/e cut off 120 nm above the waveguide top but zero on the sides. A cross-section of the sensing volume can be seen in Figure 4.11.

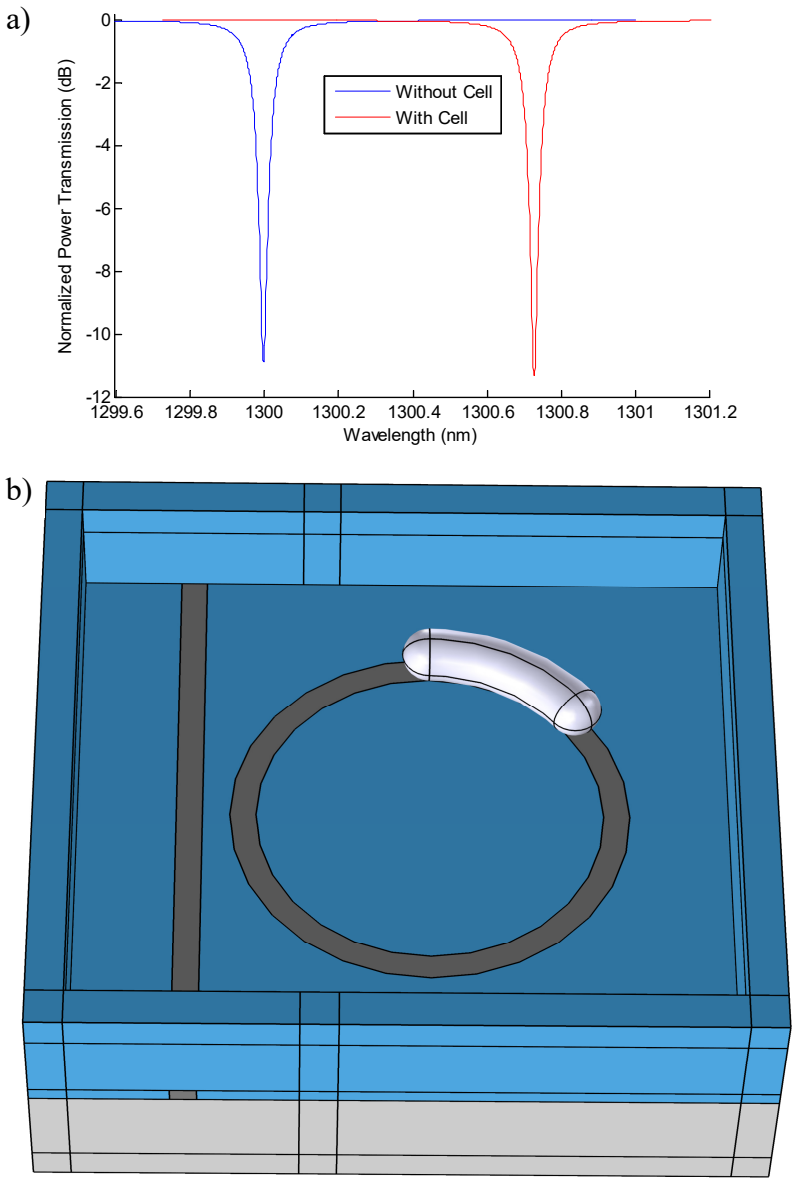

Figure 4.10. Transmission spectrum (a, upper) indicating wavelength shift due to single bound bacterium in the In-Plane binding condition (b, lower).

Table 4.1. 3D Model results of resonant shift in varied binding scenarios due to single bound cell.

Binding Scenario	In-Plane	Tee	Top	Outer Corner	Inner Corner	Outer Side	Inner Side
S_d (pm/cell)	728	127	95	67	55	19	9
FOM_d	13.00	2.27	1.70	1.20	0.98	0.34	0.16
Sensed Analyte Optical Size $\ell\Delta n_{eff}/\lambda$ (mRIU)	32	5.6	4.2	3.0	2.4	0.84	0.40

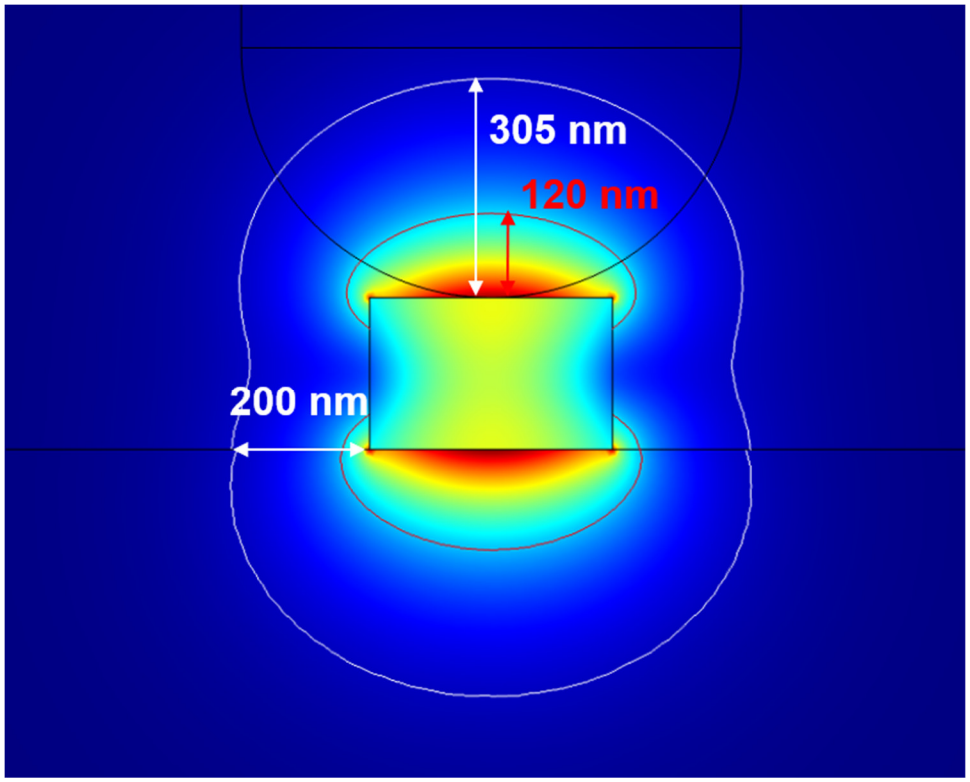

Figure 4.11. Sensing volume and electric field profile of optimized waveguide for 1/e shift (red) and 1% shift (white).

Considering the remaining binding conditions, the In-Plane and Tee scenarios represent two ends of the spectrum for cases when the cell is bound with its long axis parallel to the substrate. The In-Plane condition has a maximum amount of the analyte interacting with the ring, and the Tee condition represents the minimum if the cell binds to the top of the waveguide. Other similar bindings will fall between these cases as roughly the sine of the angle between the cell axis and the ring radius. S_d in the In-Plane case will be proportional to the length of the bound cell, which can vary significantly even within a single cellular strain population [101]. However, it is notable that S_d in all other considered binding scenarios will be essentially length independent and depend only on the radius of curvature. As a radius of curvature of/around 360 nm is typical of spherical bacteria [105], these other binding cases therefore apply to a range of both rod shaped and spherical bacterial strains.

The Top binding represents binding in the case of the analyte axis perpendicular to the substrate, with the Corner condition representing the worst case. Initially considering binding in the center

of the waveguide, a S_d = 95 pm/cell and FOM_d = 1.7 were found, indicating an easily detectable binding event. Varying the location of the cell in the Top binding showed a wavelength shift within 10% of the maximum for over 40% of the waveguide top surface. A worst-case shift occurred with the cell in the inner corner of the ring and resulted in 43% lower sensitivity than when bound in the center of the waveguide. The inner corner shows lower performance than the outer corner due to the slight migration of the ring mode away from the center of the waveguide, which is expected for small bending radii.

The absolute worst-case performance occurs for the Side binding, an in this case there is a factor of 2 difference between the binding on the inner side and outer side of the ring. However, even for the inner side binding, an FOM_d = 0.16 is seen. This is 8-fold larger than the FOM = 1/50 detectable limit achievable with accurate wavelength referencing [109]. It is concluded that the 2.5 μm TM O-band ring represents a ring design optimized for S_d in whole cell detection, as comprehensive computer simulation suggest it will detect a single *E. Coli* bacterial analyte in all potential binding scenarios.

5. EXPERIMENTAL DETECTION OF A CELLULAR SIMULANT

5.1. Overview

To experimentally demonstrate the sensing potential of an optimized microring for whole cell detection, the previously developed simulations were used to design a cellular simulant (CS) made of the electron beam lithography (EBL) photoresist ma-N 2403 [110]. By depositing the CS on rings and measuring transmission spectra before and after removal of the CS, the effect of a single bound cell can be experimentally simulated. This has the advantage of allowing accurate placement of the analyte and allows for SEM to confirm the position of the analyte for subsequent comparison of measured transmission shifts with that expected from simulation. Ma-N 2403 is easily removed in acetone, allowing for minimal disturbance of the chip except to remove the CS.

The total optical size of the CS was designed to approximately to an *E. coli* cell bound to the ring in the In-Plane binding geometry. The refractive index and absorption of ma-N were measured across the C and O-bands by ellipsometry to account for material dispersion, with the Sellmeier fit incorporated in the previously developed models. The average measured $n \approx 1.609$ with low absorption agree well with manufacturer specifications [111].

In order to confirm that a focus on the TM O-band was indeed warranted, TE and TM silicon rings for use in the O and C-bands were initially fabricated. The cladding sensitivity of the rings was measured, along with the achievable quality factor and finesse for a range of radii.

5.2. Fabrication of devices for experimental cellular simulant proof of concept demonstration

5.2.1. Fiber-to-chip coupling: grating couplers

5.2.1.1. Motivation for use of grating couplers

Coupling light into and out of an integrated optical chip is a nontrivial problem due to the refractive index difference between an optical fiber and silicon waveguides. Low coupling loss requires efficiently converting the fiber mode into a mode that will be supported by the waveguide. As the mode parameters are a function of both material and wavelength, this coupling is inherently

wavelength dependent. A few commonly employed methods of coupling are lensed fiber to inverse tapers [112] and grating couplers [113].

Lensed fiber may be coupled with inverse fiber tapers to match mode size, which achieves low loss. However, the added steps to properly define the chip edge make this relatively time intensive and expensive in a research setting. Using a lensed fiber [114] to couple directly to a single mode silicon waveguide is simple but suffers from a high loss of ~10 dB per facet. Additionally, alignment is relatively time intensive and requires design accommodations or careful alignment techniques to eliminate coupling to the slab mode in the bulk silicon substrate.

Grating couplers are more wavelength dependent and design intensive than simple focusing based side coupling schemes but allow for a much greater integration density on chip, as well as lower losses compared to direct lensed fiber to silicon waveguide coupling. Instead of a linear distribution of N devices, an array of N x N devices may be made on the same chip. This makes grating couplers ideal for research and development testing, as many parameters may be varied on the same chip, saving both time and money. Furthermore, use of a fiber v-groove array allows a single 5-axis stage to be used for both input and output alignment [113]. If a chip is designed properly, once the angular alignment and vertical offsets are set, the lateral (X and Y) adjustments necessary to move from device to device are quick and simple. This allows for measurement times of ~ 2 minutes per device, meaning a chip with hundreds of devices may be characterized in a single day.

5.2.1.2. Design and simulation

For coupling, initial devices focused on partially etched grating couplers [113]. A grating setup was simulated in COMSOL Multiphysics and modeled a single mode fiber coupling through either air or water into a silicon grating with partially etched grating teeth. Situations of fiber-to-chip (F2C) coupling, with a fiber coupling light into a grating and waveguide, and chip-to-fiber (C2F) coupling, with a waveguide mode being diffracted by a grating up into a fiber, were both considered due to the non-reciprocal nature of the scattering involved. In practice, the F2C case is the limiting factor for bandwidth and maximum coupling efficiency, and it was this situation for

which optimization was ultimately performed. Simulation was done in 2D to minimize computational time requirements.

Simulation of the grating structure requires variation of several parameters, including grating period, duty cycle, etch depth, and coupling angle [113]. Grating coupling efficiency depends on both wavelength and polarization, requiring design for each wavelength and wavelength band of interest. Within these, a wavelength range must be simulated to determine bandwidth for both the F2C and C2F cases. Additionally, the optimal position of the fiber with respect to the grating depends on the particular design, requiring lateral offset be optimized for each design iteration. The thickness of silicon on top of the waveguide, thickness of buried oxide layer, and refractive index of material between the grating and the fiber also play a large role, with re-design usually being necessary if altering these values. For this work, silicon top thickness was fixed at 220 nm, buried oxide thickness fixed at 2 μm, and water was present between the silicon and fiber. Maintaining design parameters but changing from a water overcladding to an air overcladding will primarily result in a center wavelength shift.

Fabricated couplers typically differ from simulated couplers in duty cycle and etch depth, while the grating period and waveguide height will be extremely close to those simulated. Variations in duty cycle and etch depth are a result of non-idealities in the RIE process, specifically RIE lag [115], sidewall sloping [116], and the difficulty in predicting/maintaining etch rates in the highly chemical Cl_2/O_2 ICP RIE plasma etch. These will result in changes to the center wavelength, coupling efficiency, and bandwidth [113].

Optimal lateral alignment varies with the coupler parameters, and changes somewhat between the F2C and C2F coupling cases. The C2F case has much larger tolerances for misalignment than the F2C case due to the large size of the fiber core compared with the grating teeth. One of the consequences of the use of a v-groove array instead of independently controlled fibers is that the lateral alignment will be practically fixed for both the F2C and C2F cases if the couplers are laterally aligned and the v-groove is parallel to the aligned couplers. This forces a less than ideal coupling scenario, although this could be avoided if the grating positions were offset from one another to compensate.

In simulations, height from the chip to fiber was assumed to be 1 μm. A larger height will generally decrease maximum coupling and bandwidth, although this decrease will not be significant close to the chip [113].

An optimal coupling design for partially etched couplers used with an aqueous overcladding was found for both TE and TM polarizations and the O and C-bands. A duty cycle of 50% was chosen to simplify the simulation space, and a 70 nm etch depth was found to give maximum coupling (agreeing with many prior designs in 220 nm Si, such as [117]). A coupling angle of 10° was chosen to match previously purchased polished fiber v-groove arrays. Coupling angle does not have a strong effect on maximum efficiency but does have a large effect on the center wavelength [113].

Table 5.1. Partial etch grating designs for use with aqueous overcladding at a 10° coupling angle.

Mode	Center Wavelength (nm)	Etch Depth (nm)	Grating Period (nm)	Duty Cycle (%)	Peak Efficiency (%)	3 dB Bandwidth (nm)
TM	1310	70	750	50	50	57
TE	1310	70	510	50	58	60
TM	1550	70	1040	50	51	91
TE	1550	70	637	50	55	77

These couplers were fabricated and measured, and the resulting spectra differed significantly from the simulated results primarily though differing center wavelength. The simulation was then revisited with the etch depth varied, as etch depth is the only parameter that should have varied substantially from design to fabrication. It was determined that an etch depth of 130 nm gave results closely matching the fabricated devices. Compared to the intended etch depth, the deeper etch gave a slightly non-optimal maximum coupling efficiency, but a broader bandwidth.

5.2.1.3. Layout for fabrication

For fabrication, the couplers were designed as focused gratings, bringing the large size of the fiber mode down to the small size of the waveguide. A true focusing structure requires a parabolic distribution [118]. However, for reasonable curvatures, the coupling efficiency is not drastically changed. Thus, the curves used here are simply circles, and the focus distance is increased slightly to avoid needing to do a full curvature optimization.

Couplers were designed for use with fiber optic v-groove arrays (OZ Optics, P/N#: VGA-8-250-10-A-10.0-3.5-1.43-s-1300/1550-9/125-3U-1-1-0.5-GL) fabricated from Pyrex top and bottom pieces to allow viewing of the chip through the coupler. Examples of this view can be seen in Figure 5.1. The v-groove arrays contain arrays of either 4 or 8 fibers, spaced at 250 μm, with the end face polished at 10° off normal. The size of the fabricated gratings exceeds that necessary from simulation in order to increase the alignment tolerance of the couplers. A larger coupler does have the result of decreased bandwidth, so a reasonable size was chosen.

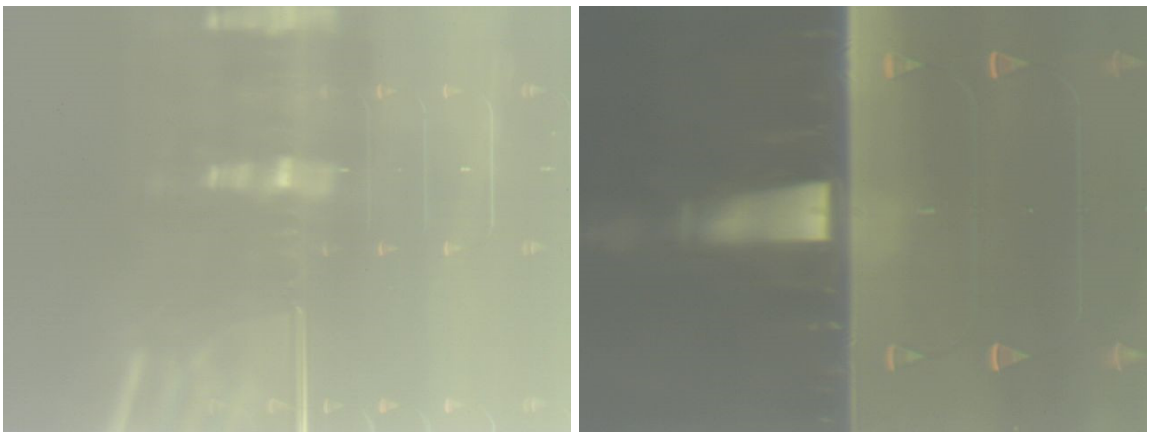

Figure 5.1. Views of fabricated devices through the all Pyrex fiber v-groove array.

Lowest measured fiber-to-fiber loss was 10 dB for the TE O-band, 10 dB for the TE C-band, 14 dB for the TM O-band, and 18 dB for the TM C-band. However, it was desired to intentionally decrease the power to avoid nonlinear effects in the rings. As a result, fiber-to-chip distance was increased to achieve a fiber-to-fiber loss of 30 dB for all devices.

5.2.2. Microring fabrication

Silicon microrings were fabricated on an SOI wafer with 220 nm Si thickness and 2 μm of buried oxide. Waveguides were defined with 100 kV EBL and 100 nm thick hydrogen silsesquioxane (HSQ) resist, followed by inductively coupled plasma reactive ion etching (ICP RIE) in a chlorine and oxygen plasma. Partially etched, focused vertical grating couplers for use in an aqueous environment were designed specifically for each wavelength band, with the partial etch occurring in a separate step before patterning of the waveguides, rings, and coupler edges.

All-pass coupled rings for use in either the O-band or C-band were fabricated, with C-band devices having 500 nm wide waveguides and O-band devices having 350 nm waveguides. These widths were chosen for single mode operation and to balance high Δn_{eff} from Figure 4.4 to Figure 4.7 with reasonable loss. Smaller widths may increase loss considerably [46] especially for small radii ring, though this was not explored experimentally here. Rings with radii of 10, 7.5, 5, 3.75, 2.5, and 1.25 μm were fabricated, with a variety of gap sizes to obtain near-critical coupling. Two sets of identically designed devices were patterned, a set of sensing rings for later use with the ma-N CS and the other to function as reference rings. The reference rings were designed with the intention of serving as an environmental control to allow environmental changes during removal of the CS to be compensated for.

5.2.3. Characterization overview

Characterization of the rings was performed with Keysight 81600B and 81960A tunable lasers and N7744A power meters. Scans with 1 pm resolution over both the O and C-bands were taken with and without DI water overcladding. Fiber-to-chip coupling was accomplished with a fiber v-groove array (OZ Optics) and grating couplers designed for use with an aqueous overcladding at the appropriate wavelength band and polarization. Polarization was adjusted between the TE and TM cases with a fiber polarization controller. Gratings in water gave a fiber to fiber loss of ~14 dB and ~10 dB in air, though input power for characterization was intentionally reduced to avoid nonlinear effects in the silicon rings.

5.2.4. Sensitivity to cladding liquid

By comparing the resonant shift between air and water overcladdings, the ring sensitivity to a bulk refractive index change could be measured. A summary of measured sensitivity, along with a comparison to simulated values (based on the measured fabricated waveguide widths), can be seen in Table 5.2. Note that the simulated values here differ slightly from those shown in Table 3.1 due to the use of measured waveguide widths instead of the design widths.

Table 5.2. Cladding sensitivity for fabricated rings compared with simulated values, and measured loss characteristics.

Quantity	TM O-band	TE O-band	TM C-band	TE C-band
S_c - Simulated (nm/RIU)	111	58	189	46
S_c - Measured (nm/RIU)	112	52	178	47
S_c Percent Difference – Measured vs. Simulated (%)	+1%	-12%	-6%	+2%
FOM_c	1700	800	550	650
$Q_{L,max}$	21,600	21,600	5,100	23,500
F_{max}	350	330	55	550

TM O-band rings showed a cladding sensitivity S_c up to 133 nm/RIU, with S_c between 112-115 nm/RIU near 1310 nm. This matches to within 1% the predicted S_c of 111 nm/RIU at 1310 nm from simulation in Table 5.2. As expected, this sensitivity was dependent on resonant wavelength. Variation across the wavelength band of ±13% was seen, with larger sensitivity occurring at longer wavelengths due to increased mode delocalization. Ultrasmall radius rings of 1.25 μm were seen to have a sensitivity increase of ~12% due to their increasingly delocalized mode, though at the cost of significantly reduced Q. S_c for rings 2.5 μm and larger showed no change in sensitivity with respect to radius, as expected. TM C-band rings showed S_c near 1550 nm of 178 nm/RIU, with no variation in sensitivity with radius. This matches the predicted value to within 6%. C-band rings showed a maximum $Q_L \approx 5000$ for $R \geq 5$ μm and O-band rings offered $Q_L \approx 20000$ for $R \geq 2.5$ μm. TM O-band rings demonstrated a 6-fold higher finesse than TM C-band rings. TE O-band rings showed comparable F_{max} to TM O-band rings, but with substantially reduced S_c. TE C-band rings showed ~60% higher F_{max} than TM O-band rings, but with an ~60% decrease in S_c. Due to

their high F, high Q, and high S_c, the FOM_c achieved by the TM O-band rings was 2 to 3-fold greater than other ring types, and though not the focus of this work, even surpasses that achievable with many other higher sensitivity sensor types [119].

5.2.5. Comparison of the demonstrated S_c to prior art

The only other use of O-band microring sensors known to the author [91] explored TM and TE O-band rings in silicon for cladding sensing purposes with the intent of maximizing FOM_c through the relatively lower loss of the O-band. Similar to this work, [91] used 220 nm of silicon and a 2 μm buried oxide layer, but differed in the use of a fixed ring radius of 30 μm, and waveguide widths of 300 nm for the TE mode and 400 nm for the TM mode. [91] showed measured cladding sensitivity to an aqueous NaCl solution and to deposited proteins.

For the TE mode, the demonstration in [91] showed a limiting Q of ~8400, F of ~8 (assuming an n_g=4.6), S_c of 90 nm/RIU, and FOM_c of 670. The larger waveguide width here (350 nm vs. 300 nm) leads to a 2.6-fold higher Q than [91], but a 42% lower S_c. The combination of these effects leads to a 19% higher FOM_c in this work. The main substantial difference is that the smaller radius rings and lower losses in this work show a 40-fold higher F than [91].

For the TM mode, the demonstration in [91] found a limiting Q of ~33500, F of ~33 (assuming an n_g=4.7), S_c of 113 nm/RIU, and FOM_c of 2900. The smaller waveguide width here (350 nm vs. 400 nm), and potentially the fabrication process, lead to a 36% lower Q than [91], but nearly identical S_c. The higher losses here lead to a 41% lower FOM_c compared to [91]. As with the TE mode, the main substantial difference is that the smaller radius rings in this work result in a 33-fold higher F than [91].

As ring size (and F) are not directly related to sensitivity in cladding sensing applications, this difference is a result of optimizing for F in this work, whereas ring size in [91] was likely a somewhat arbitrary choice. Beyond that difference, as far as cladding sensitivity, the demonstration here is largely comparable to [91]. The fact that the two are comparable in terms of cladding sensitivity can be taken as an independent validation of the work presented here.

5.2.6. Predicting FOM_d

Having experimentally obtained F and Q values for rings of multiple radii, estimates of FOM_d could be obtained (via Eq. 3.13) by determining simulated values for the sensed analyte optical size ($\ell\Delta n_{eff}/\lambda$). 2D+Z simulation of straight waveguides with bound In-Plane cells were performed to determine the sensed analyte optical size for TM and TE modes at the O and C-bands. The estimated FOM_d was then obtained as the product of the experimentally obtained F and the computationally obtained $\ell\Delta n_{eff}/\lambda$. These values can be seen in Table 5.3, with the estimated FOM_d shown in bold, and the maximum $FOM_{d,est}$ underlined. As expected from Eq. 3.13, for a fixed sensed analyte optical size, the largest values of FOM_d occur at values of maximum finesse, not values of maximum Q.

Table 5.3. Predicted FOM_d for TE and TM modes in the O and C-bands.

Mode	Analyte optical size, $\ell\Delta n_{eff}/\lambda$ (mRIU)	Quantity	R = 10 µm	R = 7.5 µm	R = 5 µm	R = 3.75 µm	R = 2.5 µm	R = 1.25 µm
TM O-band	33.2	$Q_{L,max}$ (x1k)	19.4	21.6	21.3	16.0	20.0	0.5
TM O-band	33.2	F_{max}	85	125	185	185	350	17
TM O-band	33.2	$\boldsymbol{FOM_{d,est}}$	**2.8**	**4.2**	**6.2**	**6.2**	**<u>11.7</u>**	**0.6**
TE O-band	4.2	$Q_{L,max}$ (x1k)	16.5	17.0	20.9	21.6	18.2	4.0
TE O-band	4.2	F_{max}	75	105	190	260	330	150
TE O-band	4.2	$\boldsymbol{FOM_{d,est}}$	**0.3**	**0.4**	**0.8**	**1.1**	**<u>1.4</u>**	**0.6**
TM C-band	38.2	$Q_{L,max}$ (x1k)	5.1	4.6	4.1	2.4	0.7	X
TM C-band	38.2	F_{max}	35	40	55	40	17	X
TM C-band	38.2	$\boldsymbol{FOM_{d,est}}$	**1.3**	**1.5**	**<u>2.1</u>**	**1.6**	**0.7**	**X**
TE C-band	4.2	$Q_{L,max}$ (x1k)	19.2	19.3	19.1	22.3	23.5	2.3
TE C-band	4.2	F_{max}	110	150	225	345	550	110
TE C-band	4.2	$\boldsymbol{FOM_{d,est}}$	**0.5**	**0.6**	**0.9**	**1.4**	**<u>2.3</u>**	**0.5**

The TM O-band gives the highest predicted FOM_d of 11.7, which is the best by 5-fold. The TM and TE C-band rings have values of 2.1 and 2.3, showing that the increased sensitivity of the TM C-band mode suffers from the high loss of a 220 nm silicon top thickness. The TE O-band was seen to have slightly lower F than the C-band, leading to the worst values of the four. Considering the achievable F, it was concluded that a focus on the TM mode O-band was warranted. It will be the focus for the remainder of this work.

5.3. Cellular simulant fabrication

After creation of the microring devices and a validation that a focus on the TM O-band was warranted, the ma-N CSs were patterned. Samples were initially solvent cleaned in 5-minute ultrasonic baths of toluene, acetone, and isopropyl alcohol. Then, samples were Piranha cleaned (1 part 30% H_2O_2 to 3 parts concentrated H_2SO_4) for 10 minutes, followed by an H_2O rinse and N_2 gun dry. The sample was then dipped in premixed 7:1 HF:H_2O buffered oxide etchant (BOE) for 7 seconds to remove native oxide from the silicon waveguide. The sample was then placed on a 150 degree °C hot plate for 15 minutes to desorb water from the silicon surface.

The preceding cleaning steps were crucial for proper photoresist adhesion. While ma-N adheres very well to bare silicon, it adheres poorly to silicon dioxide [120]. This is because, like many common photoresists, ma-N is nonpolar, and requires a nonpolar, hydrophobic surface for good adhesion [121]. Bare (hydrogen terminated) silicon provides such a hydrophobic surface and is stable for some time (up to ~1 hr.) in an air ambient environment [99]. Silicon dioxide, in contrast, provides a hydrophilic, polar surface, due to the presence of surface hydroxyl (OH) groups [122]. This is accentuated with oxide grown in the presence of H_2O, as in either wet oxide or native grown oxide in a wet ambient, or with the oxide grown during the Piranha clean [123]. Thus, the BOE dip removes the strongly hydrophilic oxide, replacing it with a strongly hydrophobic hydrogen terminated silicon surface [124]. Heating to 150 °C not only dehydrates the surface, but thermally cracks any remaining OH bonds to present a uniform hydrophobic waveguide surface for strongly adhered ma-N [125]. The same effect could have been achieved with an adhesion promoter such as HDMS [121], but the optical effect of HDMS of indeterminate thickness on the resonance response was unknown.

After cooling to room temperature, ma-N was spun at 3000 RPM for 30 s and post-baked at 90 °C for 75 s. After 100 kV EBL, the chip was developed in MF-26A for 45 s. Figure 5.2(a) shows a silicon ring with deposited ma-N CS, and Figure 5.2(b) shows an identically designed reference ring without an ma-N CS.

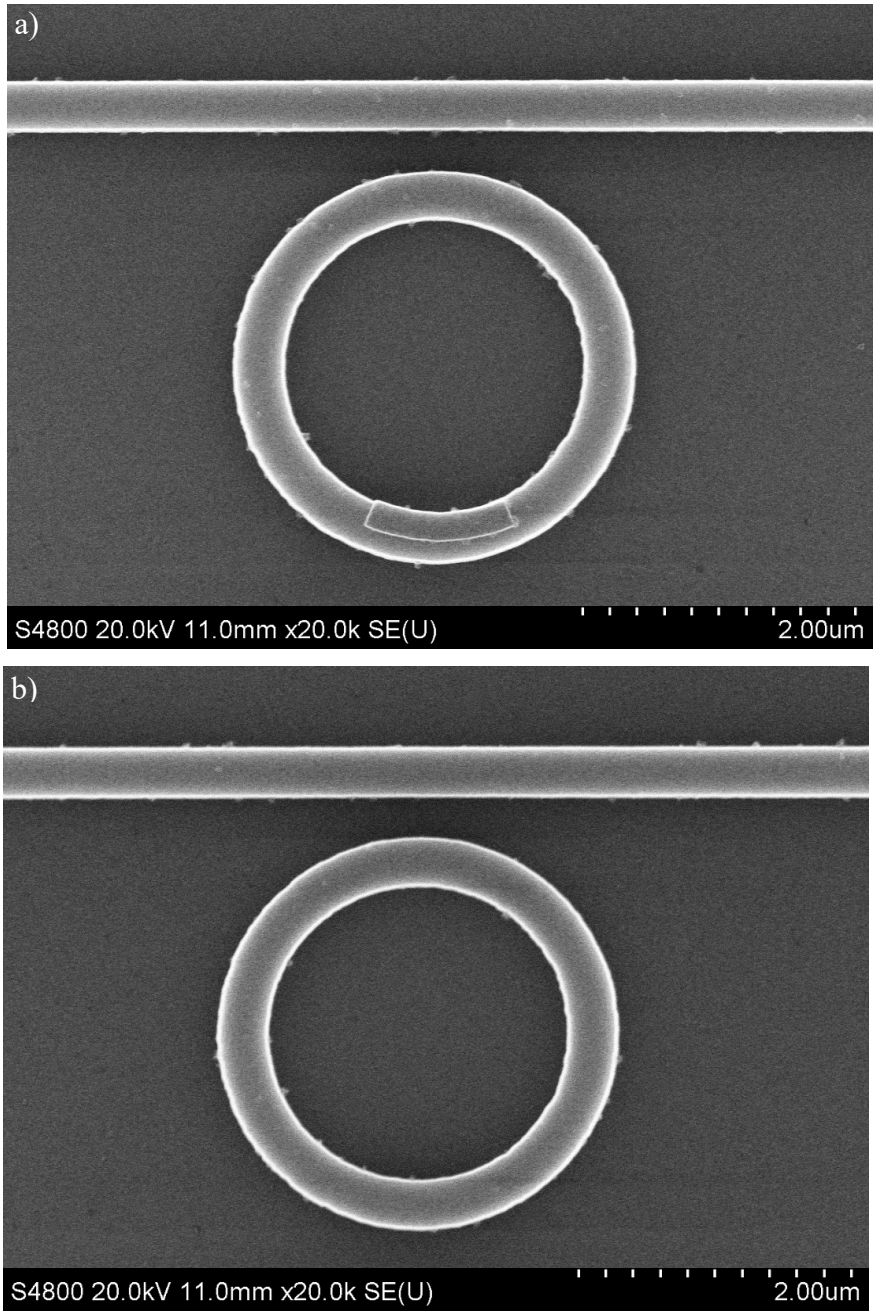

Figure 5.2. Fabricated silicon microring sensing ring with ma-N cellular simulant (a, top) and reference ring without cellular simulant (b, bottom).

Patterned ma-N had an average thickness of 110 nm and width of 200 nm, as measured by SEM and AFM. Small (<50 nm) residual particles of ma-N were noticed after development, likely resulting either from incomplete dissolution/development from MF-26A, unintentional crosslinking during the 150 °C baking [126], or coagulation of photoresist after its expiration date. However, even for large rings the total volume of residual ma-N was much less than the volume of deposited ma-N in the CS. As a result, the residual ma-N could function to decrease the signal to noise of the measurement, particularly for larger rings, while still offering a meaningful shift in resonance due to the CS.

The CS was found to be offset from the designed position in the center of the ring waveguide due to EBL alignment error. The radial and lateral offset combined to an effective ~63 nm radial offset from the waveguide center. Additionally, keystone error had the effect of stretching the length of the simulants by ~1.5%, resulting in simulants 1035 nm long in the circumferential direction.

5.4. Characterization of proof of concept devices

5.4.1. Initial measurements

Measurement was performed as described in Section 5.2.3. For the first step in the comparison, measurements were taken with the chip covered in DI water with the ma-N CSs present. In order to minimize temperature drift between the sensing and reference rings, measurements were taken such that each sensing ring and its corresponding reference ring were measured within minutes (<2) of one another. DI water was let sit for 24 hours to thermally equilibrate with the room before being dispensed on top of the chip. The temperature of the substrate holder was also monitored to within 0.1 °C to ensure thermal drift in the room was not a factor.

5.4.2. Cellular simulant measurement removal and remeasurement for TM O-band

After devices were measured with water cladding and ma-N present, the chip was removed from the stage and soaked for 10 hours in a covered beaker of acetone. This had the effect of completely dissolving any attached ma-N on the chip, as ma-N is typically removed instantly when exposed to acetone [111]. The sample was then double rinsed in DI water to remove any residual ma-N. It was then further cleaned in a standard solvent clean, with a five-minute acetone soak, followed by

isopropyl alcohol, and finally followed by DI water. All solvents had been allowed time to reach thermal equilibrium with the rest of the laboratory to minimize thermal drift. The chip was then placed back onto the measurement stage, and re-clad with room temperature DI water.

With ma-N having been removed, the transmission spectra of each device were then remeasured. An example of wavelength spectra for both reference rings (which had no deposited CS) and sensing rings (which previously had a deposited CS) before and after ma-N was removed is seen in Figure 5.3. The large blueshift (shift towards shorter wavelengths) seen in the sensing ring was taken as a confirmation of the removal of the ma-N CS, while the relatively unchanged behavior of the reference ring confirmed its desired roll as a control.

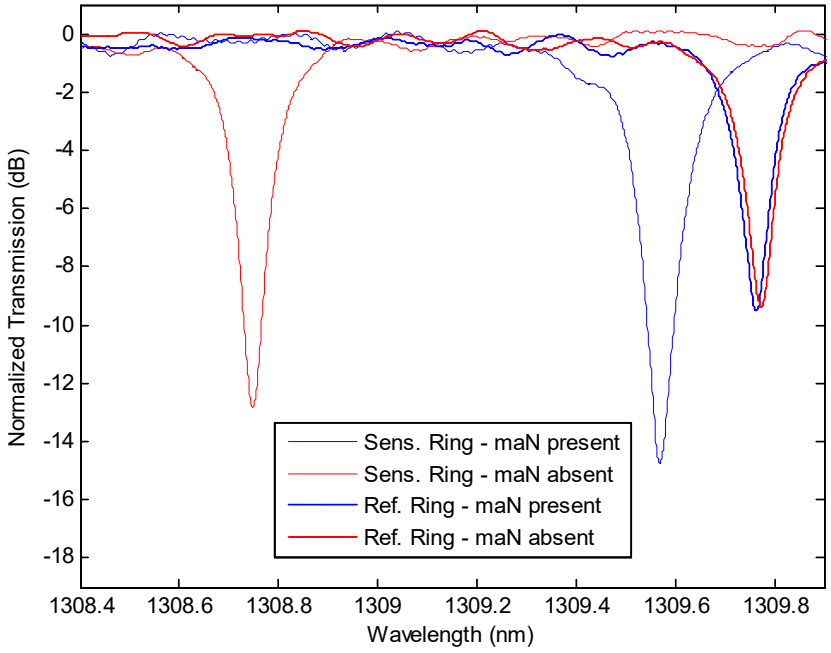

Figure 5.3. Normalized transmission spectra of corresponding 2.5 μm radius sensing (solid) and reference (dotted) rings before (blue) and after (red) ma-N removal.

The resonance shifts for the 1310 nm resonance family of all measured pairs of sensing and reference rings before after the acetone soak are seen in Figure 5.4(a). For clarity, the plot is shown as the shift due to the presence of ma-N, which was positive (redshift), instead of the shift due to the removal of ma-N, which was negative (blueshift). As a whole, the reference rings showed a

mean redshift of 39 nm after removal of ma-N, with a standard deviation of 107 nm. This shift was essentially independent of radius, as expected from changes in resonance due to temperature or the radius independent presence of residual ma-N particles before removal in acetone. The sensing rings showed a very strong radius dependent resonance shift, as expected. To isolate the shift due to the ma-N CS, the relative shift between the sensing and reference rings was found by subtracting the reference ring shift from its corresponding sensing ring, as shown in Figure 5.4(b) for all ring pairs.

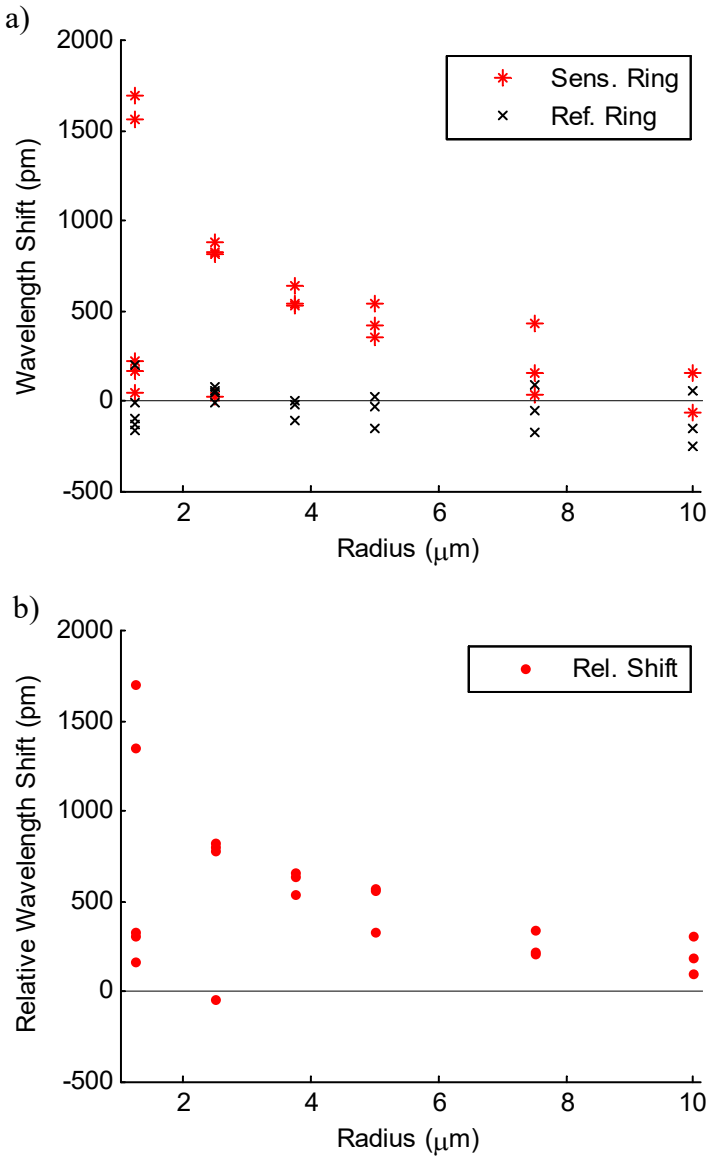

Figure 5.4. (a, upper) Resonance shift of 1310 nm resonance family due to presence of ma-N for both sensing and reference rings, and (b, lower) the relative shift of sensing/reference ring pairs.

A majority of the 1.25 μm and one of the 2.5 μm sensing rings showed a shift within the range of the reference rings instead of the much larger shift characteristic of sensing rings. As the relative shift of these rings compared to their corresponding reference rings was more than 3 standard deviations outside the relative shift of other ring pairs of the same radius, this was deemed an error outside of environmental fluctuation. The adhesion of ma-N to the waveguide relies on a strong oxide and water free bond between the ma-N and silicon. This was ensured in fabrication by thorough cleaning and promotion of a hydrophobic waveguide surface. However, the combination of radial and circumferential offset of the ma-N CS places part of the CS very close to, or indeed over, the edge of the top of the waveguide. This can be seen in the left part of the CS in Figure 5.2(a). The strong curvature of these smallest rings exacerbates the effect. Additionally, measurement was done from largest rings to smallest, with the 1.25 μm ring CSs experiencing the greatest time in aqueous overcladding. It is therefore likely that photoresist adhesion was compromised, either by penetration of water or the growth of a wet native oxide between the CS and the waveguide surface. This would have caused significant loss of the CS before initial measurement of the sensing ring resonance could be done. As major outliers, these device pairs with shifts below 350 pm for 1.25 μm rings and below 0 pm for 2.5 μm rings were neglected for the remainder of the analysis here.

Comparison of wavelength shifts in the same resonance family in Figure 5.5 is necessary due to the wavelength dependence of the wavelength shift. Indeed, all the important ring parameters were seen to vary in some form with respect to wavelength. An example of this is shown in Figure 5.5 for a 2.5 μm radius ring.

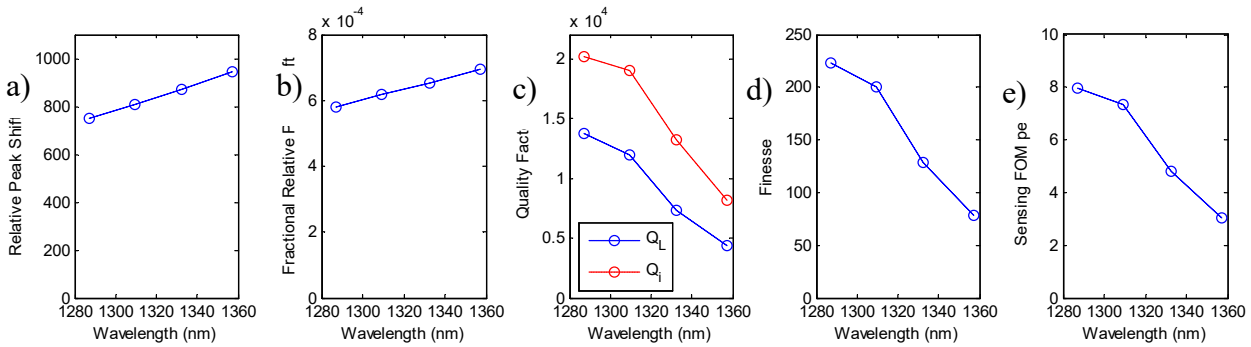

Figure 5.5. Example of wavelength dependent behavior of (a) relative peak wavelength shift, (b) fractional relative wavelength shift, (c) loaded and intrinsic quality factor, (d) finesse, and (e) sensing figure of merit per fabricated cellular simulant.

The relative peak shift in Figure 5.5(a) is seen to be directly proportional to wavelength. This is a result of increased modal delocalization with increasing wavelength and mirrors the previously seen dependence of cladding sensitivity on wavelength. Additionally, even though it was included to help compare devices operating at different wavelengths, the fractional wavelength shift in Figure 5.5(b) is also seen to depend strongly on wavelength. This is because the wavelength dependence changes much more rapidly than does the center wavelength itself. The loaded and intrinsic quality factor in Figure 5.5(c) are dependent on modal delocalization, as is wavelength shift, though Q has an inverse dependence. Larger modal delocalization means both increased bending loss and scattering loss, although at this radius scattering loss is the dominant component. Additionally, for any coupling gap, shorter wavelength light will be more weakly coupled than longer wavelengths. This results in more strongly undercoupled resonances for shorter wavelengths, also contributing to higher loaded Q. However, if coupling differences were the dominant factor, intrinsic Q should remain constant. Although we imperfectly estimate it here (via $Q_i = 2Q_L / \left(1+\sqrt{10^{(ER/10)}}\right)$ [127], where ER is the measured extinction ratio), it could be more rigorously measured with a symmetrically coupled ring to definitively determine which effect is dominant. It should be noted that ER for this device was measured to be above 9 dB for all resonances, both with and without the CS, making for clearly resolvable peaks. Finesse, seen in Figure 5.5(d) is quite similar in its wavelength dependence to Q. Although it additionally depends on the FSR and center wavelength of each resonance, for a given radius these change only slightly with radius. Thus, the wavelength dependence of F closely mirrors that of Q_L for a given radius.

The sensing figure of merit, *FOM*, defined in Eq. 3.10 and seen in Figure 5.5(e), depends equally on the wavelength shift and the Q (or F). However, due to the much larger change in Q (and F) vs. wavelength than the wavelength shift vs. wavelength, the *FOM* for a given radius is dominated by the contribution of the Q (and F).

It is additionally notable that the earlier assumption in section 2.2.7 of unchanged dispersion due to the analyte holds extremely well. Across all devices, n_g changed less than 1% after the removal of ma-N, with similar variation for both reference and sensing rings.

5.4.3. Agreement of fabricated performance with simulation

To account for the wavelength dependence of the peak shift and *FOM*, a linear fit of all a device's relative resonant peak shifts was made and evaluated for a given reference wavelength. This is particularly useful for precise comparisons with the 3D model, as a difference in resonance wavelength of ~10 nm (2% fractional difference) was present due to fabricated radii being slightly larger than designed. The measured relative shift due to the deposited CS could then be directly compared with that expected from simulation to validate the previously developed models. A wavelength normalized comparison between the relative shift measured for 2.5 μm radius rings (Figure 5.6(a-c)) and that obtained from 3D COMSOL modelling with an introduced CS (Figure 5.6(d)) is seen in Figure 5.6.

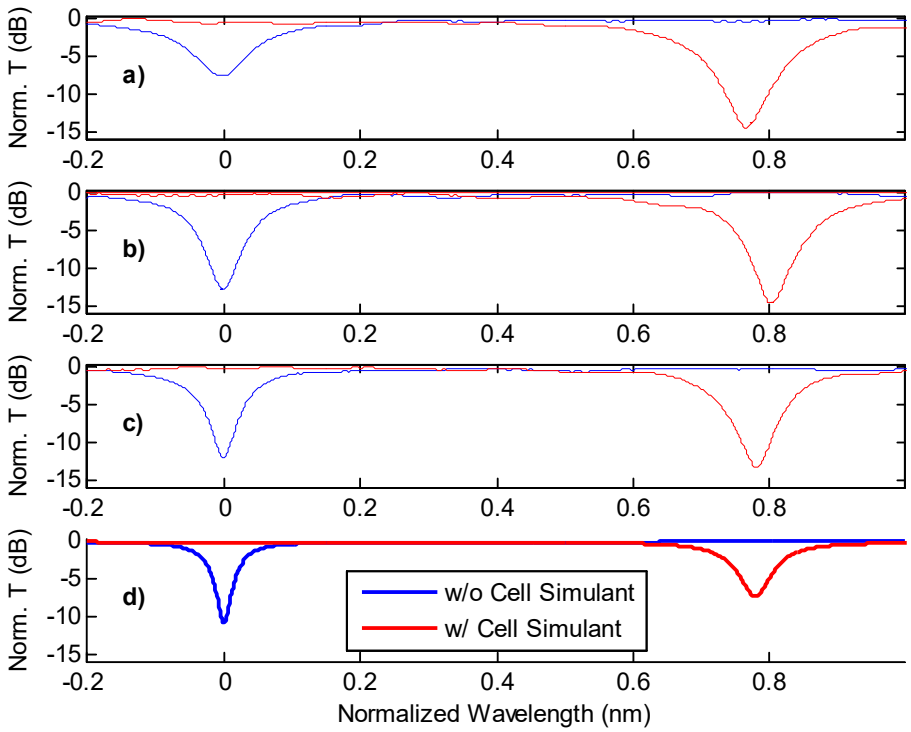

Figure 5.6. (a-c) Measured relative resonance shift of 1310 nm resonance family due to ma-N cellular simulant compared to (d) the 3D simulated cellular simulant for the m = 24 mode.

The parameters for the modelled CS were obtained from the measured SEM (such as Figure 5.2(a)) and AFM values of the fabricated CSs. Excellent agreement between the model and experiment was obtained, with resonances for all 3 devices falling within 3% of the predicted 779 nm shift. Critical coupling is obtained at a coupling gap of 365 nm for a bare simulated ring, and Q_L falls 60% from 23.2k to 14.5k due to the CS. For the measured rings, the highest Q_L is obtained for a 300 nm coupling gap (seen in Fig. Figure 5.6(c), and previously in Figure 5.5), which similarly falls 38% from 11.9k to 8.6k due to the CS. The degradation in Q_L is likely a result of increased scattering loss due to the relatively high refractive index of the CS compared with water. For other rings, the decrease in Q_L is similar.

As a result of the excellent agreement between the measured values and the simulated model, the 3D simulation results can be used to better understand the measured sensing performance. According to the model of a 2.5 μm ring, the deposited CS produces a 7% larger wavelength shift

than would be obtained by a single bound cell in the In-Plane binding condition. The measured relative shifts can thus be reduced by 7% to accurately normalize the CS optical path difference to that of a single bound cell. This normalized relative shift of the 1310 nm mode family for all rings can be seen in Figure 5.7. This normalization also allows the normalized wavelength shift to be considered the discrete analyte sensitivity S_d for an In-Plane *E. Coli* cell, and the *FOM* to be the discrete analyte figure of merit FOM_d for an In-Plane *E. Coli* cell.

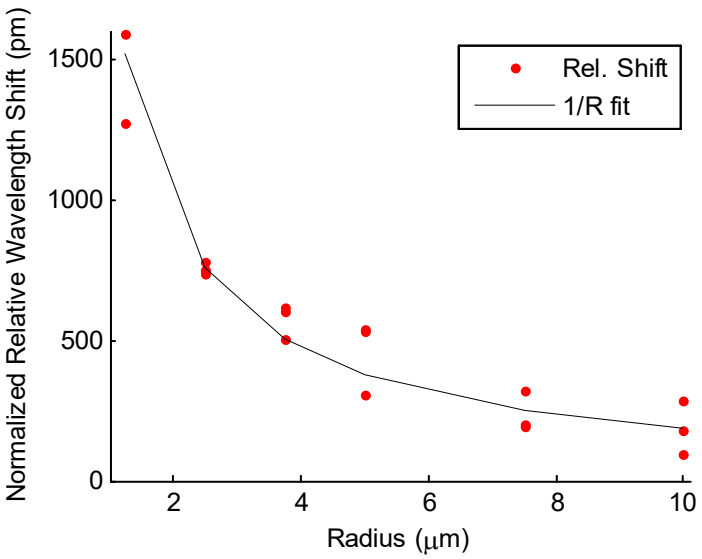

Figure 5.7. Measured relative shift of sensing rings normalized to that of a single bound cell in the In-Plane binding condition.

Using the mean shift of the 2.5 μm rings as a reference, the behavior of the rings can be fit to the 1/R dependence predicted by Eq. 3.8. This simple 1/R fit matches the average of the measured shifts to within 20% for each radius, which experimentally confirms the derived dependence of discrete analyte sensitivity on ring size.

5.4.4. Determination of discrete analyte sensitivity and figure of merit

Once normalized to match the optical size of the CS with a single bound cell, the normalized relative wavelength shift of Figure 5.7 is equivalent to the discrete analyte sensitivity S_d defined in Eq. 3.8. However, a more appropriate way to quantify this is take the mean for all measured

rings of a given radii to reduce the effect of noise. In the case of Q_L and F, the lack of uncertainly or noise effects make the maximum value at a given radius similarly appropriate.

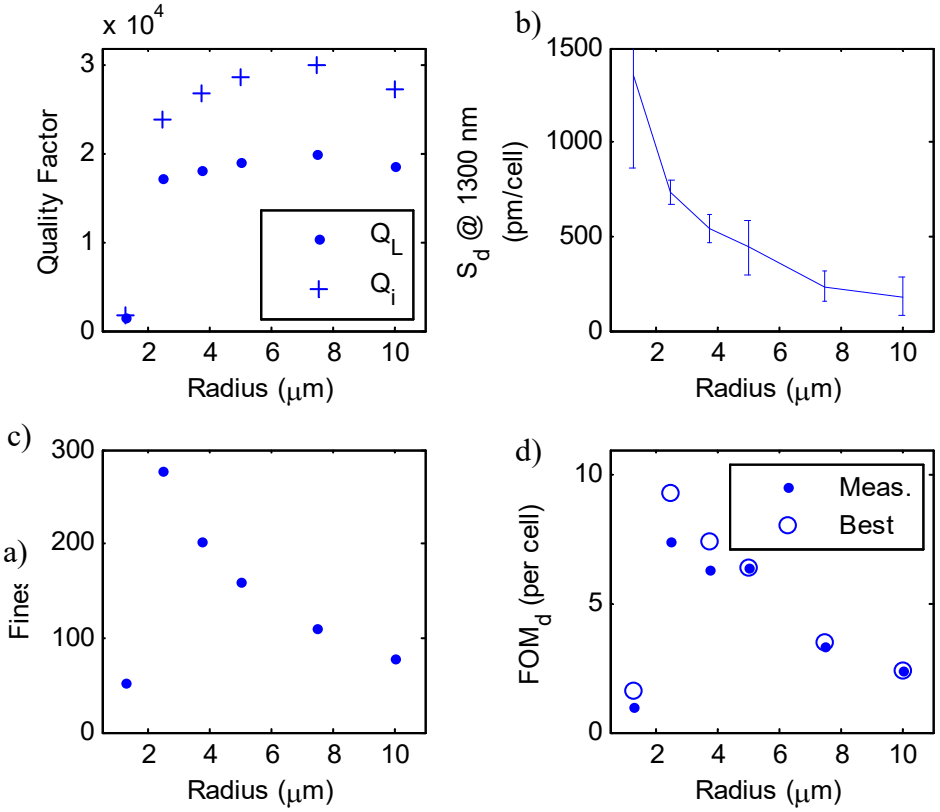

Figure 5.8. TM O-band sensing performance for varying radii rings. (a) Maximum measured loaded Q and estimated intrinsic Q, (b) mean measured discrete analyte sensitivity S_d and standard deviation normalized to 1300 nm, (c) maximum measured finesse, and (d) discrete analyte sensing figure of merit FOM_d for best measured sensing devices and best measured ring.

Figure 5.8 shows the performance summary of the TM O-band rings with respect to radius. The maximum measured Q_L and the corresponding estimated intrinsic Q, Q_i, is shown in Figure 5.8(a). Q_L was seen to jump by an order of magnitude in the move from R=1.25 μm to R=2.5 μm. Here Q_L essentially saturates, as $Q_{L,max}$(2.5 μm) = 17.2k is lower by only 16% than highest measured Q_L for any radius ring of 19.9k. This is comparable with other published sensing rings [91], making our result typical. However, it is likely that many of the larger radius rings may be slightly overcoupled, requiring a gap larger than 300 nm for best operation. Additionally, the Q_i estimated for all devices was significantly below the calculated absorption limiting Q. This indicates further

refinement in the fabrication process to reduce scattering losses could have a significantly beneficial effect.

The mean S_d normalized to 1300 nm is shown in Figure 5.8(b), along with the corrected sample standard deviation for each radius. The variation in measured S_d of typically ~100 pm is a result of the noise present on the entire sample, as the reference rings as a whole show a standard deviation of 107 pm with a mean redshift of 39 pm. The small mean shift of the reference rings suggests a temperature drift <1 K, as the temperature sensitivity of the rings (from Table 3.1) is predicted to be ~52 pm/K. Thermal drift [128] [129] is unlikely to be the source of the ~100 pm deviation, as a 2 K swing would be required within the ~2 minutes between measurement of sensing of reference rings. The noise is likely a combination of the unwanted residual ma-N particles and the effect of solvent cleaning, which may remove spurious dust particles collected before initial measurement. This deviation would be much smaller in an integrated microfluidic system, and any short scale thermal drift could be removed by simultaneous monitoring of the reference and sensing rings.

While Q_L remains relatively constant for $R \geq 2.5$ μm, the measured F_{max} as seen in Figure 5.8(c) scales as $1/R$ once Q_L has saturated. The measured sensing figure of merit normalized to a single cell in the In-Plane binding condition is shown in Figure 5.8(d). This is calculated as $FOM_d = S_d(\lambda)Q_L/\lambda$ where the mean S_d is used to minimize the effect of measurement variation. Also shown is the "Best Case" FOM_d that would have been measured if the highest measured Q resonance were used for sensing. For both 2.5 μm and 3.75 μm rings this happened to occur on a reference ring, though in other rings a sensing ring offered the best Q_L.

The largest measured $FOM_d = 7.4$ is seen for a 2.5 μm ring, with a best-case value of $FOM_d = 9.3$. Either of these are more than large enough to detect the binding of a single cell in the In-Plane binding condition. Compared to simulation, these values are lower by 43% and 28%, respectively, as a result of lower Q_L than the bending loss limited case in simulation. As predicted, it is seen that FOM_d decreases approximately as $1/R$ after saturation of Q_L. This confirms the importance of sensor size for maximizing discrete analyte sensitivity, as a 3.88x increase in performance is seen for the 2.5 μm rings compared to 10 μm rings. Even larger radii would see a similar performance

degradation. Comparing finesse with FOM_d and S_d reveals a very close correlation between the two, validating the use of finesse as a key component in the discrete analyte sensing figure of merit. It also allows for prediction of device performance with other analytes if the effective optical size of the analyte is known.

5.4.5. Estimated lower bound for detection

Taking the best measured Q_L as indication of achievable performance, the uncertainty in S_d can be used to form a lower bound estimate of performance. It was seen that mean measured S_d matches simulated values to within 3% but taking the lower bound estimate of mean minus sample standard deviation, S_d could be reduced by up to 8%. Combining this with the 28% lower FOM_d due to Q_L, a worst case estimated FOM_d could be reduced 35% compared to simulated values. Performance for the considered bindings estimated using this lower bound are shown in Table 5.4. We can also compare this lower bound estimate for S_d with our current system limit of detection [91], defined as a change 3 standard deviations above the noise limit. For our tunable laser and power meter, this is limited by the stability of the measured resonance wavelength [80] which was found for a TM O-band ring in DI water to be $\sigma = 0.6$ pm over multiple scans. The ratio of the estimated lower bound sensitivity to our system detection limit is listed in Table 5.4. While FOM_d provides a measurement system independent look at performance, $S_d/(3\sigma = 1.8 \text{ pm}) > 1$ represents successful detection of a bound cell by our current scanning measurement setup.

Applications such as continuous monitoring with highly multiplexed sensors are of interest, and for these a 3σ limit is unsuitable. The 3σ detection limit is only valid for hundreds of observations, as at 3σ, every 1 in 370 measurements would be expected to fall outside the $\pm 3\sigma$ range. More appropriate would be a 6σ limit, for which we would expect only 1 in 5×10^9 to fall outside the $\pm 6\sigma$ range. For our setup, $6\sigma = 3.6$ pm. Given the 1 pm resolution of scanning, and to eliminate false detection of shifts in the range $3.5 \text{ pm} < \Delta\lambda < 3.6$ pm which would register at 4 pm, we consider a rounded up 6σ level to be $\lceil 6\sigma \rceil = 5$ pm. The result of this definition of a detection event is somewhat over cautious and will likely eliminate many actual detections of a cell. The benefit of being sure not to include false detection events due to normally distributed noise is deemed worthwhile.

Table 5.4. Predicted lower bound estimate for measured response to single bound cell in various binding scenarios.

Binding Scenario	In-Plane	Tee	Top	Outer Corner	Inner Corner	Outer Side	Inner Side
$S_{d,LB}$ (pm/cell)	667	116	87	61	50	17	8.2
$FOM_{d,LB}$ (per cell)	8.50	1.48	1.11	0.78	0.64	0.22	0.11
$S_{d,LB}/3\sigma$ (per cell)	371	64	48	34	28	9.4	4.6
$S_{d,LB}/6\sigma$ (per cell)	185	32	24	17	14	4.7	2.3
$S_{d,LB}/\lceil 6\sigma \rceil$ (per cell)	133	23	17	12	10	3.4	1.6

For all considered binding cases, including the most taxing case of a single cell bound on the Inner Side of the ring, the lower bound performance estimates exceed the detection limit. In the Inner Side case, $FOM_{d,LB}$ = 0.11, 5x larger than the 1/50 limit [109], and $S_{d,LB}/\lceil 6\sigma \rceil$ = 1.6, similarly indicating successful detection. This strongly suggests that the fabricated 2.5 μm devices would be able to detect the binding of a single cell, regardless of the particular binding geometry. Larger rings, however, would fall below this limit, with a cut off below 4 μm. Rings up to ~15 μm could satisfy the FOM_d = 1/50 limit [109], but would require significant changes in instrumentation to bring S_d above the $\lceil 6\sigma \rceil$ = 5 pm level.

6. PROOF OF CONCEPT DISCRETE DETECTION OF BACTERIAL ANALYTES

6.1. Overview

Although the capability of the optimized rings was demonstrated with cellular simulants, and the fabricated structures matched simulation extremely well, a proof of concept demonstration was desired to show the sensitivity of the rings to actual cellular analytes. This is because the previously demonstrated sections rely on literature measurements of the refractive index of cellular analytes, and it is desirable to link the computational models with real world experiment.

To accomplish this, cellular sensing chips were designed for use with *E. coli* cells, but without antibody binding chemistries or complex microfluidic setups. A large PDMS microfluidic channel was used, which shows performance in an unoptimized microfluidic device.

Under these conditions, cells will not be either physically or chemically bound to the sensing rings. Detection depends on transient proximity of the cells to a ring while the laser is scanning that particular ring. Due to practical effects of measurement discussed later in this section, the amount of time that a sensing ring will be probed will be very small. The upshot of this is that a multiring device will be self-referenced, as any ring not interacting with a cell will act as a reference for all other rings, and a ring will act as a reference for itself both before and after a cellular detection event. However, detection will require a large number of cells in solution to observe detection events due to the low likelihood of random interaction. As this is a proof of concept demonstration to validate the previous optimization, it is sufficient to support the analysis and optimizations of this work. Realization with a microfluidic setup and binding chemistry, while certainly not trivial, will not change the investigation in this work assuming that discrete detection events are indeed observed.

6.2. Design optimization of cellular sensing chip

In light of the optimization in chapter 4 and photoresist cellular simulant demonstration in chapter 5, device design utilized a silicon microring resonator 2.5 μm in radius, consisting of a waveguide

350 nm in width and 220 nm in height, operating with the TM polarization and in the O-band wavelength range. Beyond the individual sensor level, chip level optimizations also exist.

6.2.1. Wavelength-division multiplexing

As this work utilizes a tunable laser with a scanning range of ~100 nm, much of the spectrum is unutilized if only a single sensor is being used on a waveguide channel. Similar to the technique of wavelength-division multiplexing (WDM) [130] used in communications, a variety of sensors could be designed with differing resonant wavelengths. This would allow a much better use of the available characterization equipment and opens the possibility for a single pair of IO ports to measure multiple sensors. Multiple sensors could either be spread across a microfluidic channel to increase the channel size or capture rate, or rings could be placed in different microfluidic channels to sense different fluid samples. Depending on the functionalization process, this would include using a single IO pair for multiple bacterial types.

The ability to take advantage of this capability is a result of the single mode nature of the resonators, which provides easily discernable resonances, and the high finesse of the optimized devices. An example of the definition of Finesse from the ring transmission wavelength spectrum is seen in Figure 6.1. Finesse is directly equal to the number of resonances that fit within a single *FSR* at a spacing of one *FWHM* and is a quantification of the multiplexing ability of a resonator.

In practice, the maximum number of sensors per channel are determined by fabrication effects, specifically the achievable resonance finesse and center wavelength consistency. Both factors change with m, and thus experimental investigation was necessary to obtain reasonable values for both F and the repeatability of λ_m. For a 2.5 μm radius resonator, F values of 225-450 were achieved at the low end of the spectrum (1260-1290 nm), 160-280 in the center (1290-1320 nm), 50-150 at the top (1320-1360 nm). A plot F vs. wavelength, with the m values identified, can be seen in Figure 6.2. There is a clear decrease in F as wavelength increases, which is a result of using a resonator that is nearly in the radiation loss limited regime. This behavior suggests that potentially only the lower wavelength m values should be used for a highly multiplexed sensor.

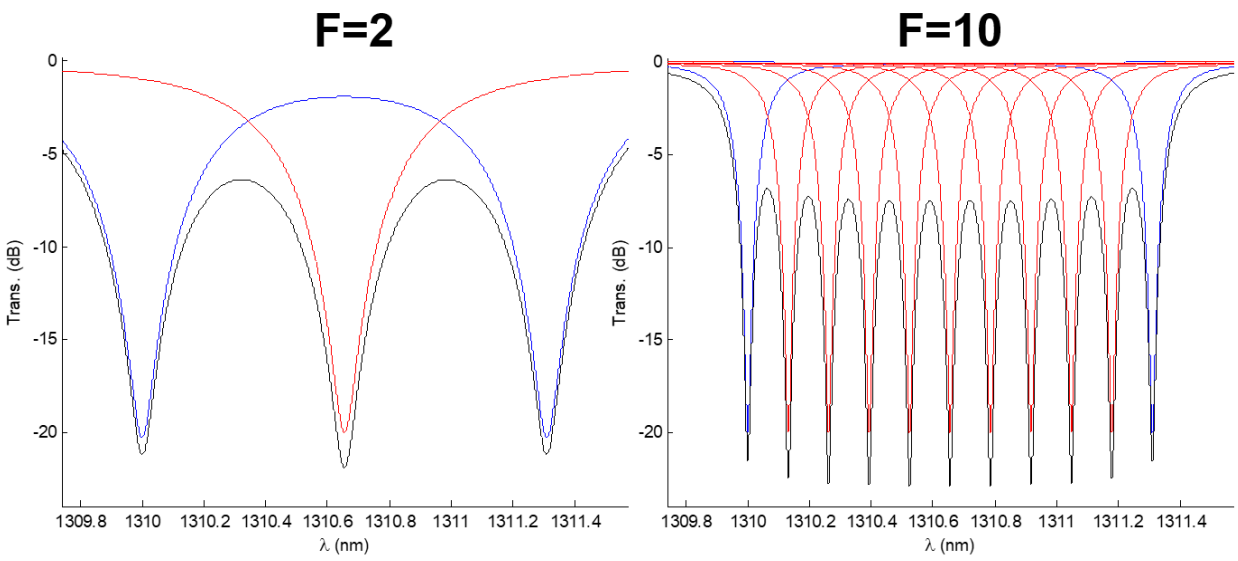

Figure 6.1. WDM definition of Finesse, for cases of $F = 2$ (left) and $F = 10$ (right).

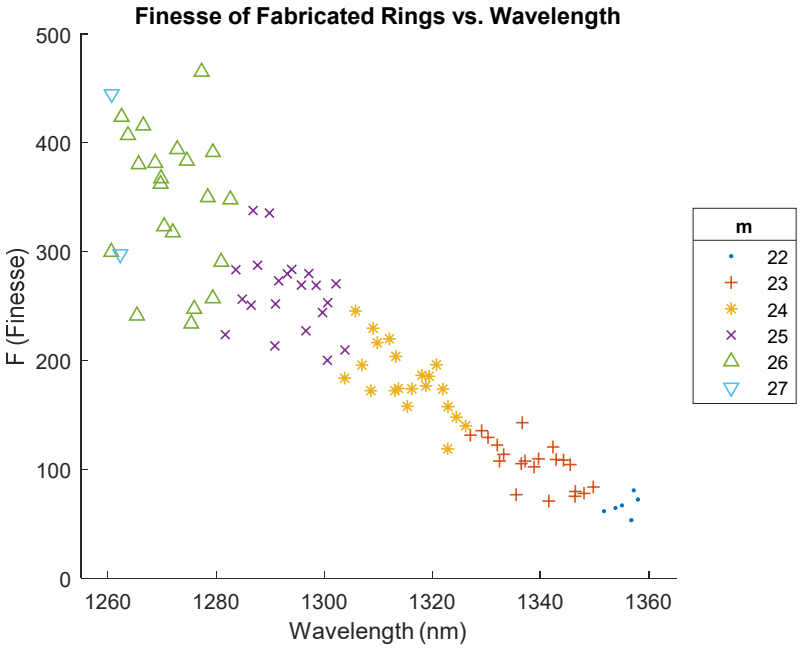

Figure 6.2. Finesse vs. wavelength of fabricated rings, with *m* values specified.

The writing accuracy of the EBL tool for the majority of this work (Vistec VB6) has shot placement steps down to 5 nm in the large field mode (~1300 µm fields) and 2 nm in the small field mode (~500 µm fields). The higher available writing current (and resulting lower cost) of the large field mode, which also helps reduce stitching errors through fewer field writes, was desired.

This limits the radius step of fabricated rings to 5 nm. The center wavelength change depends on the mode number through Eq. 2.50. The radius dispersion for a 2.5 μm Si TM ring (220 nm H x 350 nm W) in the O-band is seen in Table 6.1. It is notable that the shorter wavelength resonances will overlap before the longer wavelength resonances. With this in mind, rings can be designed to overlap at a single larger *m* resonance, and the gaps in the spectrum at smaller *m* will still enable resonance identification.

Table 6.1. Resonant wavelength radius dispersion for O-band microring.

m	λ_m (nm)	n_{eff}	n_g	*FSR* (nm)	$d\lambda/dR$ (nm/nm)	Rings/*FSR* (5 nm BSS)	Rings/*FSR* (2 nm BSS)	Rings/*FSR* (0.5 nm BSS)
21	1374.661	1.838	4.420	26.687	0.229	24	59	234
22	1347.974	1.888	4.576	24.812	0.221	23	57	225
23	1323.162	1.937	4.697	23.310	0.216	23	55	217
24	1299.852	1.986	4.790	22.076	0.212	22	53	209
25	1277.776	2.034	4.861	21.032	0.210	21	51	201
26	1256.744	2.080	4.916	20.124	0.208	20	49	194

In order to overlap at only a single *m*, the use of a 5 nm radial step limits the usable number of rings to 21 per channel. A 2 nm beam step size (BSS) would enable 51, and a 0.5 nm BSS would allow up to 201. These numbers are independent of Finesse. Thus, in the 5 and 2 nm step cases, Finesse is not a limiting factor, but in the 0.5 nm step case, the BSS limits becomes comparable to the achievable Finesse. The use of larger radius resonators will decrease the $FSR \propto 1/R$, and thus decrease dλ/d*R*. The result is that the maximum number of rings per *FSR* is inversely proportional to *R*. Finesse, the ratio of *FSR* to *FWHM*, is thus the figure of merit for WDM ability. The maximum rings per IO channel will be limited by the lesser of the Finesse and the maximum rings per *FSR* (as limited by BSS). Practically speaking, a width of at least 2.5 μm beyond each ring should be reserved to avoid modal cross talk (for the rings presented here). This would imply a minimum total footprint of 10 μm per ring. Thus for 201 rings in an IO channel, a device footprint of >2000 μm^2 would be required. Such a design would be achievable on an EBL tool with a 1000 μm large field size and 0.5 nm minimum step size, such as the JEOL JBX-8100FS.

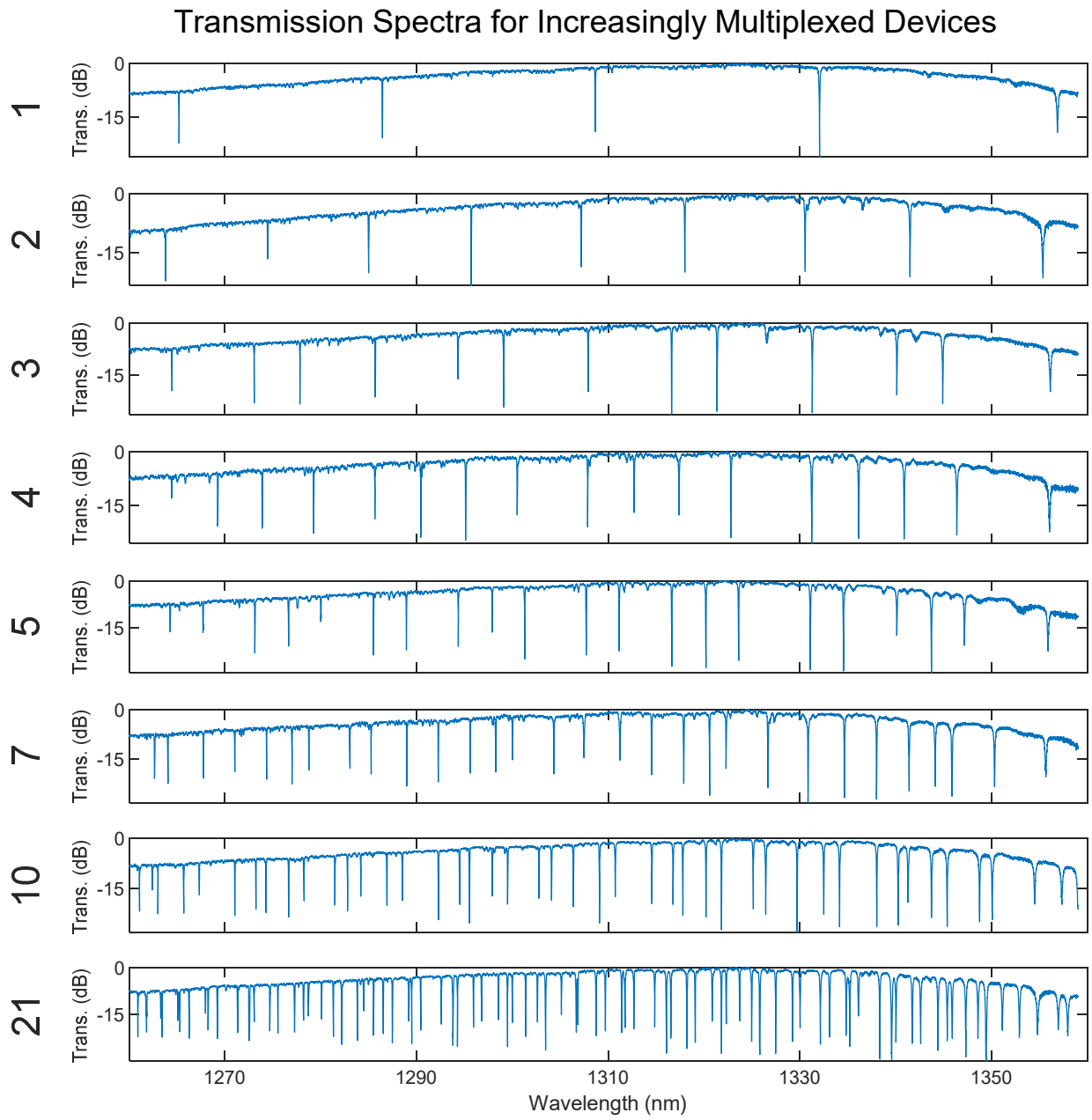

Figure 6.3. Transmission spectra of fabricated multiplexed ring arrays, from 1 to 21 rings.

The resulting spectra of multiple rings written with 5 nm shot placement steps in a single waveguide are shown in Figure 6.3. A difference between the designed and actual center wavelengths was seen to be in the range of ±1 nm. This large uncertainty may be a result of the 5 nm shot placement or may be inherent to the fabrication procedure. A method of decreasing or

correcting this uncertainty, such as adjustment with integrated heaters [129] or post fabrication trimming [131], would be desirable in a fuller implementation.

6.2.2. Time division multiplexing

The maximum scan speed of the Keysight 81600B O-band tunable laser over the 1260 – 1360 nm wavelength range is 40 nm/s in stepped mode, meaning a 100 nm scan takes 2.5 s. As a result, the device additionally functions like a time division multiplexed device. Wavelength spacing between each ring resonance for a 21 ring sensor (corresponding to 5 nm EBL shot steps) is ~1.08 nm, corresponding to a time delay of 27 ms. The average *FSR* of the rings across the scanning range is 22.3 nm, corresponding to a time delay between probing resonances of a given resonator of ~560 ms. As will be explained later in section 6.4.10, in that time span a cell can be expected to have diffused ~1 μm. Thus, in the absence of a binding antibody, cells may be detected at one resonance of a ring but not another. If binding antibodies were present, it would give the time resolution to within 0.5 s, if the cells were bound during the scan.

As was previously seen in Figure 4.11, for a 1% refractive index change, the extent of the sensing area of the ring is limited to 200 nm on the waveguide sides, and 305 nm on the waveguide top center. The top extent shrinks in width after ~100 nm. The more stringent $\lceil 6\sigma \rceil$ limit to be used here will further decrease the effective sensing area, down to ~200 nm on the top and ~100 nm on the sides. Cells must therefore be quite close to the ring to be detected and can easily move out of range.

The necessary delay to process and store the measured data in the Keysight N7700A Photonic Application Suite IL (Insertion Loss) Engine software, v. 1.6.2.4 means that the delay between 100 nm scans is between 10 to 11 s. Thus, during an active scan of 40 nm/s over 100 nm, the chip is only being measured ~25% of the time. Of this, the sensors are only being actively probed on resonance. For a 21 device structure, assuming an average *FWHM* of ~100 pm, and 5 *FSRs* covering the 100 nm scanned spectrum, this corresponds to a 10.5% measurement duty cycle. Combining these, any sensing ring is being probed only 2.5% of the time, an individual sensing ring is being probed 0.12% of the time, and an individual resonance is being probed 0.024% of the

time. This poses a challenge to real time detection without chemical binding that would not be an issue for antibody bound analytes.

6.2.3. Chip design and microfluidic overlay: discussion of microfluidics

Having previously demonstrated the feasibility of single cell sensitivity, devices were fabricated to demonstrate the capacity for detection of individual cells. As more complex microfluidics systems for use in bacterial detection have been demonstrated in literature previously [21] [132] [133], the chips in this work were designed to focus on the proof of concept demonstration of optimized rings designs for discrete analyte sensitivity rather than a fully optimized cellular sensor. Towards that end, neither complicated microfluidic setups nor binding chemistries were employed for this proof of concept demonstration. However, the practical requirements of a complete system were considered, as these result in optical effects that could modify the detection potential of a device.

Microfluidic design is, in and of itself, an optimization problem. Typical microfluidic systems use controlled syringe pumps to deliver fluid, and thus control flow via applied pressure [133]. As the channel size decreases, the flow in a uniform channel becomes under pressure driven flow becomes laminar [133]. This has the effect of maximizing flow in the center of the channel and essentially stopping it at the channel walls (the no-slip boundary condition), resulting in a parabolic velocity profile. As a result of this gradient, relatively large analytes will be concentrated in the center of the channel. This poses an obvious problem for sensors that would naturally lie on the outskirts of the channel, such as microring resonators. This could be resolved by placing the sensor in the path of the analytes, designing a more turbulent channel, or minimizing the size of the channel. While microfluidic design is beyond the scope of this work, the options and implications are briefly discussed.

The sensor itself could be placed in the center of the channel. This requires a suspended [134] structure, which is more complex to fabricate, but has been demonstrated in air [135]. Issues such as structural integrity in response to relatively heavy analytes and large flows would have to be explored, and the device may function as a MEMS device [136] in a fluid channel. Additionally, the presence of the sensor will disturb the flow pattern, and analytes may simply flow around the

sensor depending on the particulars of the structure and analytes. It could be possible to specifically engineer the resonator to add turbulence or have points of turbulence near the resonator [137].

Tuning of the cavity dimensions may also be used. Bacteria, and *E. coli* in particular, have been seen to grow and travel in channels equal to or below typical cell dimension [138]. However, the flow rate in such channels is necessarily heavily reduced. This substantially decreases the amount of fluid that may be analyzed, although a necessary value would depend on the application. The issue of clogging also becomes important, as even if a single bacteria can be focused to a point in a channel, upon binding with a sensor it will then restrict the flow for other analytes. The ideal situation may be a very thin channel, such that the bacteria are forced to interact with the sensor, but with a width such that reasonable flow rates can be achieved. An ideal channel would have sensors spread across the length of this channel to remove the issue of clogging and allow for detecting numerous analytes before the channel becomes unusable. In this case, the analysis of section 6.2.1 would be useful.

For this work, a large (15mm x 34 mm) glass overlay with a PDMS (14.5 mm x 33.5 mm) gasket, contains a microfluidic channel 550 μm wide by 120 μm high by 20 mm long, was used for analyte delivery. This overlay was placed on top of a fabricated sensing chip (itself mounted on top of an SEM sample holder, and clamped with a metal clip), with the chip and overlay held together at the ends by two binder clips. The overlay was placed such that the microfluidic channel was overtop of the sensing rings, and the input couplers of the chip were unobstructed by the glass overlay. The v-groove array was then aligned to the input couplers of the chip.

This setup allowed an aqueous solution of cells to be introduced on top of the sensing rings in a controlled manner. As the size of the channel is much larger than the size of the sensors, delivery to the resonators at the bottom of the channel relies on diffusion. To enhance this, fluid flow should be stopped after the channel is full. The “no flow” nature of this proof of concept setup removed the need for a pump delivery system.

6.2.4. Fiber-to-chip coupling: subwavelength grating coupler

A butt coupling scheme with cleaved chip edges requires only a patterning step and an etch step, making the fabrication straightforward. Traditional grating couplers [113] require two different silicon heights to be defined, that of the grating depth and that of the defined waveguides. This triples the fabrication steps: an initial patterning and metallization/etch step defines alignment marks, followed by a step to pattern and partially etch the gratings, followed by a step to pattern and etch the waveguides. A simplified approach is to replace the partially etched grating trench with a metamaterial analog, a subwavelength vertical structure that approximates the required refractive index of a partially etched grating [139]. This introduces more fabrication sensitivity into the design but only requires a single pattering and etch step, equal to the fabrication steps in a butt coupling scheme. It was found that metamaterial gratings are particularly sensitive to back-reflection due to the larger effective index contrast of a fully etched slot. Given the long waveguides in this work, particular care in design was needed to minimize back-reflection.

Compared to the devices used with photoresist cellular simulants, a practical sensor requires larger separation between the fiber-to-chip couplers and the sensing resonator to allow for fluid channels. The input couplers can then be operated in air, while the sensing rings are clad with water. The increased waveguide length adds propagation loss, which may not be insignificant for long waveguides. Additionally, the microfluidic channels themselves must surround sections of the waveguide. This changes the effective refractive index of the waveguide section, which then transitions from a covered section (cladded in e.g. silicon dioxide or PDMS) to an uncovered section (with an aqueous cladding, e.g. water or PBS), as seen in Figure 6.4. The change in cross-section induces a reflection due to index mismatch. These reflections result in a Fabry-Perot cavity, and degrade the overall spectrum of the device. These will be further increased unpredictably for air pockets between the chip and the overlay, such as those seen in Figure 6.5. The increased Fabry-Perot effects due to a microfluidic channel further necessitates the design of low back reflection grating couplers to minimize added spectral noise.

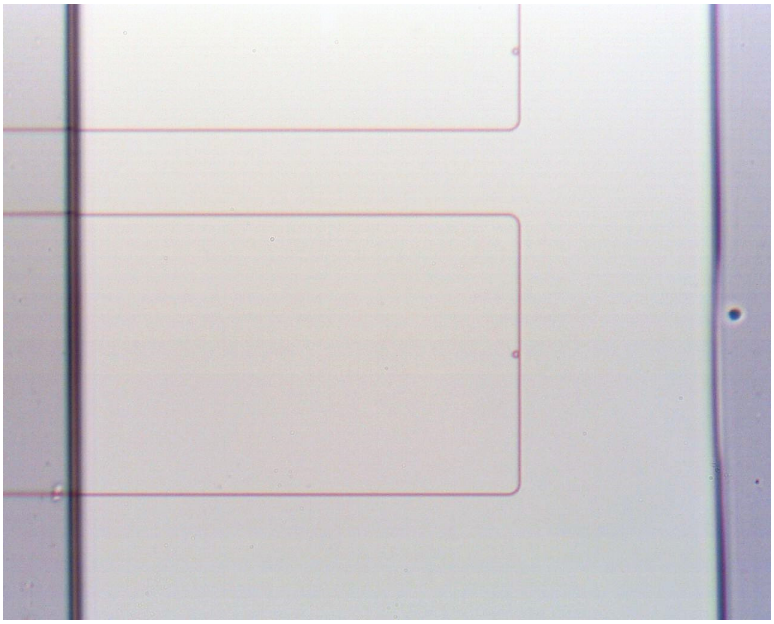

Figure 6.4. Microfluidic channel in PDMS over sensing ring and waveguide.

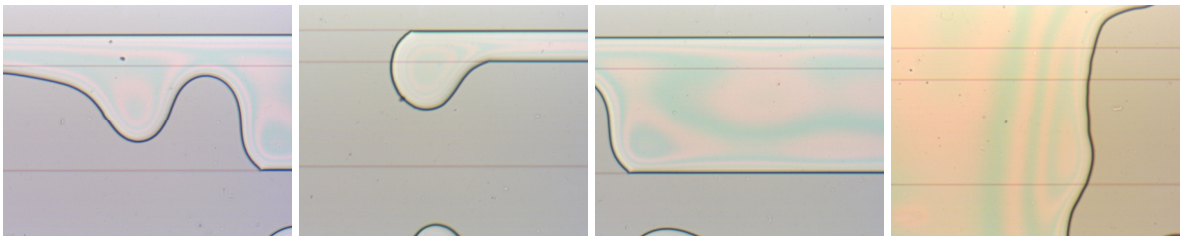

Figure 6.5. Examples of trapped air between PDMS and silicon in non-sensing sections of chip.

Fully etched focused metamaterial grating couplers [139] for use with air overcladding, the TM mode, and a center wavelength near 1310 nm were designed in COMSOL Multiphysics, with a focus on low back-reflection rather than absolute optimal coupling efficiency. The computationally optimal design was then fabricated, along with an array of slightly varied designs to account for fabrication imperfections. The fabricated optimal metamaterial grating design for low back-reflection, while also being broadband and as high efficiency as possible, coupling of the TM mode over the O-band with an air overcladding was found to have a grating period of 825 nm, a major tooth width of 495 nm (60% duty cycle), a minor tooth width of 160 nm (rounded down from 165 nm, 20% duty cycle), and gaps of 85 nm (rounded up from 82.5 nm, 10% duty cycle each). 19 grating periods were used, giving the coupler an overall length of 15.675 μm. The

grating teeth approximated a focusing parabola by circles, with a total arc of 45°. Gratings were spaced 250 µm apart to correspond to the spacing of a fiber v-groove array. An example of the layout for the optimized device can be seen in Figure 6.6.

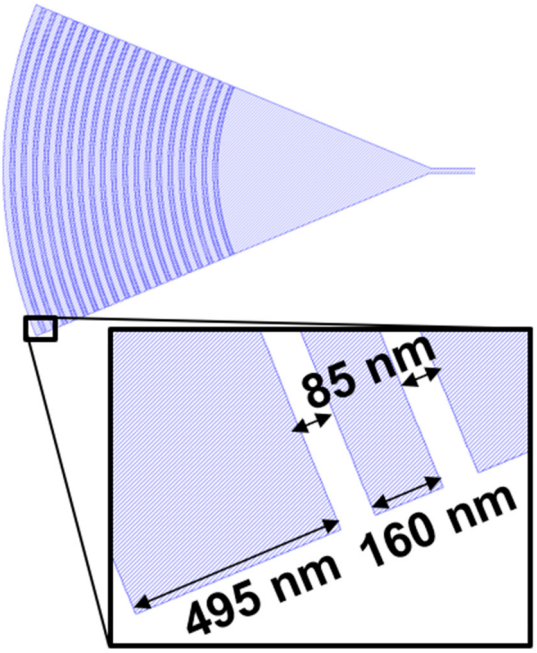

Figure 6.6. Layout of fully etched metamaterial grating coupler for low back reflection in the TM O-band.

6.3. Fabrication for cellular measurements

Obtaining well-functioning fabricated devices requires knowledge of a variety of minute points on how to handle materials, how certain materials behave, and non-intuitive but frequently encountered problems. However, despite the importance of these practical considerations for fabrication and reproducibility, they are typically omitted from formal writing. In an effort to make this work reproducible, as well as to share the lessons learned with other researchers, the fabrication details and practical considerations from this work formed the initial content of the BNCWiki [140], an online repository for the Birck Nanotechnology Center.

The sensing chip was designed with 24 ring array sensing devices. These were divided into 3 sets, each of which had rings positioned with a different orientation to the waveguide: one with rings inside the waveguide (towards the grating couplers), one with rings outside the waveguide (opposite side of the waveguide from the grating couplers), and one with rings alternating inside and outside. Each set varied the rings per device, having either 1, 2, 3, 4, 5, 7, 10, or 21 (as seen in Figure 6.3). The 21 ring device used a smallest ring radius of 2500 nm and increased this by 5 nm per ring up to 2600 nm. The other devices contained a 2500 nm ring and an even division of the remaining radii through the 2500 to 2600 nm interval. For example, the two ring device had rings of 2500 and 2550 nm, the 3 ring device had rings of 2500, 2535, and 2565 nm, the 4 ring device had rings of 2500, 2525, 2550, and 2575 nm, etc.

Device layouts were generated using a custom MATLAB script written by Dr. Ben Niu, which allows the generation of layout files with complicated geometries and allows curved structures to be approximated by polygons with a large (~3000) number of sides. Devices were converted with a beam step of 5 nm at a field size of 1300 μm x 325 μm. Layout BEAMER was used for data conversion, where BSS Alignment was set to X & Y, the facture mode was set to LRFT, a curve tolerance of 1.0 was used, and feature ordering was set to Writing Order.

Starting substrates were (100) SOI samples with a silicon top layer 220 nm thick and a buried oxide layer 2 μm thick. These were cleaved and cleaned in a three-step solvent sonication process using toluene, acetone, and isopropanol. The samples were then BOE dipped for ~4 s to remove the native oxide layer, rinsed thoroughly, and dehydration baked on a hotplate at 150 C for 3-5 minutes. XR-1541 6% was then spun on the chip at 6000 rpm for 30 s. The chip was softbaked at 120 C for 3 minutes, and then loaded into the Vistec VB-6 EBL tool. Exposure was done with a 5 nm beam step size and exposure dose of 2400 $\mu C/cm^2$. After exposure, the samples were developed in 25% TMAH for 70 s and then thoroughly rinsed in ultra-pure water. The silicon top layer was etched in a Panasonic E620 ICP RIE in a Cl_2/O_2 plasma. The remaining XR-1541 was then removed with a BOE dip and DI rinse.

6.4. Measurement of fabricated chips

The measurement setup consisted of a Keysight 8164B mainframe with an 81600B O-band laser. An N7744A Power Meter was used for detection. Polarization was controlled with a Newport F-Pol-PC fiber polarization controller. The fibers were coupled to an OZ Optics v-groove array mounted on a Newport 561D stage with DS-4F micrometers. Measurements were monitored with a 5 MP video microscope capable of 200-1250x magnification (2.8-0.4 mm field of view), and a 35 mm working distance.

The 81600B laser was scanned from 1260 nm to 1359 nm in 1 pm steps, with a tunable laser power output of 0 dBm, and a maximum detection power on the N7744A set at – 30 dBm. The fiber-to-coupler distance was intentionally increased to limit the maximum coupled power to < -30dBm to avoid non-linear optical effects. Scanning was done with a single scan at 40 nm/s. For the *FSR* of these sensors, this corresponds to a rate of ~0.5 s per *FSR*.

Scanning was initially done with the chip in air (without a microfluidic overlay), then with the microfluidic channel added, then with DI water introduced into the microfluidic channel. These initial measurements revealed the sensor was functioning properly, and that the PDMS overlay did not add a problematic amount of back reflection.

Next, the previous DI solution was removed, and an *E. Coli* laden DI solution was pipetted into the glass overlay such that the microfluidic channel was full, and the plastic end caps nearly so. The end caps were then covered to prevent evaporation or contamination. Measurement then commenced, with scans running continuously for 117 minutes. Measurement focused on a 21 ring array device, which as discussed in section 6.2.1, is the maximum number of rings in an array using a 5 nm EBL BSS. For the remainder of this section, this 21 ring array device will be referred to simply as the "sensor". The cells remained in motion throughout this time due to Brownian motion, gradually settling due to gravity. An example of the video microscope view of the fabricated 21 ring array in the bacterial solution can be seen in Figure 6.7. The waveguide to waveguide separation is 250 μm, the smallest ring (ring #1, R = 2.5 μm) is on the left, the largest ring (ring #21, R = 2.6 μm) is on the right, and the intermediate rings are appropriately distributed in the middle. Coupling gaps of 320 nm were used for all rings for near-critical coupling.

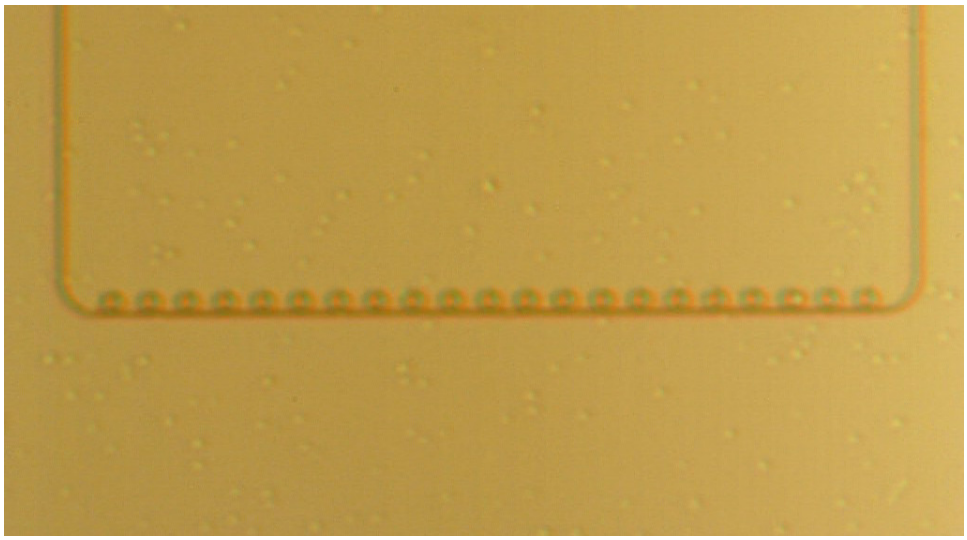

Figure 6.7. Image of *E. coli* cells over measured sensor.

E. Coli TOP10 cells were used. The TOP10 strain is a derivative of the DH10B strain [141], which is in turn a derivative of the K12 strain [142]. These were diluted in DI water from an initial concentration of ~10^9 CFU/mL to a 100x more dilute ~10^7 CFU/mL. DI water was used for dilution instead of Phosphate-Buffered Saline (PBS) due to the potential for crystallization of PBS from any evaporation, and the difficulty in cleaning off the condensed materials from the chip.

A video from the zoom microscope was later used to confirm the estimated ~10^7 CFU/mL dilution. A 250 μm x 238 μm x 120 μm volume was observed 105 minutes after addition of the cells to the microfluidic channel, and 250 cells were counted. This translates to an estimated concentration of 3.5 x 10^7 CFU/mL. Such a large dilution was required due to the large volume of the fluidic channel compared with the size of the sensing elements.

6.4.1. Detection event criteria and measurement details

As discussed in section 5.4.5, detection event criteria were defined to be conservative and rigorous. Detection events were required to have an abrupt (being defined here as a shift from one scan to the very next) resonance red shift over the $\lceil 6\sigma \rceil$ level. As mentioned in section 5.4.5, the 6σ level is significantly more conservative than typical sensor demonstrations, which typically use a 3σ level (e.g. [35]). The 6σ level is used here because of the large amount of data to be collected: 21

rings, each with up to 6 resonance peaks, being scanned over 120 minutes at 6 scans a minute, results in nearly 100,000 data points. A 4.5σ level would be required to keep the expected number of false detections to 1, and the 6σ level was used to further decrease this by over 3 orders of magnitude.

The standard deviation for wavelength noise σ_λ was determined by examining scan to scan variation in DI water, and consistent with previous experiments, was determined to be $\sigma_\lambda = 0.6$ pm. The 6σ level is then $\sigma_\lambda = 3.6$ pm. However, as the wavelength is measured in 1 pm steps, the cut off was further increased to remove the chance of round off error. The minimum shift to qualify as a detection event was therefore set at $\Delta\lambda_m = \lceil 6\sigma \rceil = 5$ pm. After this qualifying shift, the resonance was required to abruptly shift back to the previous value within noise (±1 pm). In order to ensure the resonance was clearly shifting, it was also desired that the shift satisfy $\Delta\lambda_m \geq FWHM/50$ [109].

Measurement data was automatically processed to find detection events, comparing each scan to the next after the data acquisition was finished (although this could have been done in real time with more sophisticated coding). After the automated identification process, each shift was then manually inspected to ensure the resonance shift was indeed real, uniform, and unambiguous.

As part of the detection identification algorithm, the raw spectrum was lo-pass filtered across the wavelength spectrum to remove confounding spectral features, such as double/split resonance peaks, and meta-material grating coupler induced Fabry-Perot "noise". Low *m* resonances required a more aggressive low pass filtering due to the high reflection at that end of the spectrum from the metamaterial grating coupler. For all detection events, both the filtered and raw spectra were manually inspected to ensure no spurious events were improperly counted.

6.4.2. Resonance shifts

Taking the 21-ring device as a single sensor, 92 resonances were present, which were measured by 679 wavelength scans. Comparing the change in resonance wavelength from scan to scan resulted in 62,376 resonance shifts. The distribution of these can be seen in Figure 6.8.

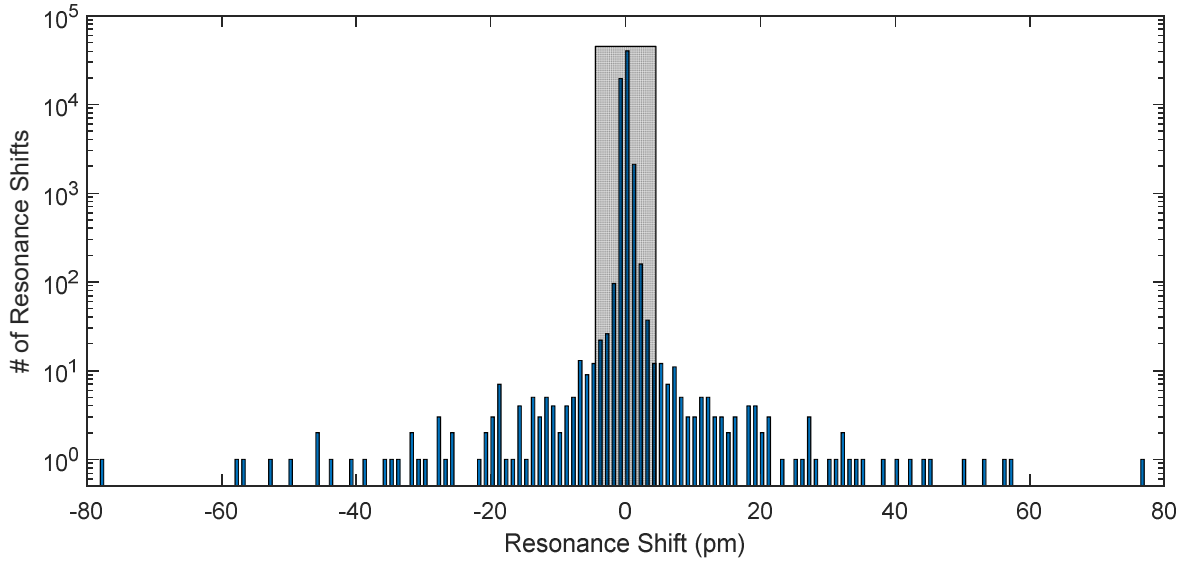

Figure 6.8. Histogram of resonance wavelength shifts for sensor exposed to cellular solution, with shifts at or below the 6σ level highlighted in grey.

40,115 (64.3%) were shifts of 0 pm, 21,705 (34.8%) were shifts 1 pm in magnitude, and 255 (0.4%) were shifts 2 pm in magnitude. Thus 99.5% of shifts were within the $\lceil 3\sigma \rceil$ range, less than or equal to 2 pm in magnitude. For context, all previous measurements of rings with DI water cladding observed at thermal steady state showed no shifts greater than 2 pm in magnitude. Of the 301 shifts larger than a magnitude of 2 pm, 204 shifts were also greater than or equal to 5 pm in magnitude. Thus, the use of the highly conservative $\lceil 6\sigma \rceil$ criteria may be ignoring some shifts due to genuine cellular interactions, but effectively ensures that false positive shifts due noise are excluded.

Based on the previously established detection criteria, which require an abrupt redshift of ≥ 5 pm and ≥ *FWHM*/50, followed by an abrupt blue shift to the previous value within noise (± 1 pm), and that the entire resonance was shifted clearly and unambiguously, 93 detection events were found. A detection event consists of both a red shift and a blue shift. The wavelength shift value of each detection event was assigned as the minimum of the red and blue shifts that make up the event. The distribution of these in terms of wavelength shift $\Delta\lambda_m$ and wavelength shift normalized to resonance width $\Delta\lambda_m/FWHM$ are presented in Figure 6.9. If a detection event is due to a single cell in the sensing region of the ring, $\Delta\lambda_m = S_d$ and $\Delta\lambda_m/FWHM = FOM_d$.

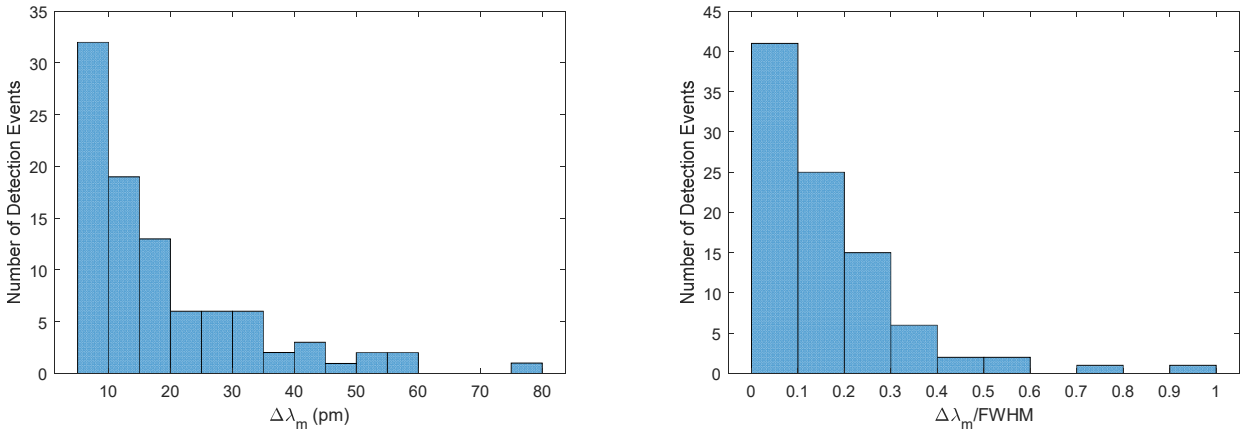

Figure 6.9. Histogram of wavelength shift (left) and resonance width normalized wavelength shift (right) for detection events of sensor exposed to cellular solution.

6.4.3. Resonance identification via free spectral range and resonance wavelength

Each resonance wavelength λ_m is due to a particular ring radius R and mode number m (Eq. 2.50). Additionally, the FSR (Eq. 2.58) depends directly on R and indirectly on m via n_g (as seen in Table 6.1). As seen in Figure 6.10, the discrete steps in FSR allow for an unambiguous assignment of an m to each resonance, and the increase in λ_m with R allows for an assignment of R. As seen in Figure 6.11, using FSR and λ_m as identifiers is much less ambiguous than using any of the loss figures Q, F, or $FWHM$, which also depend on R and m but strongly vary with fabrication imperfections.

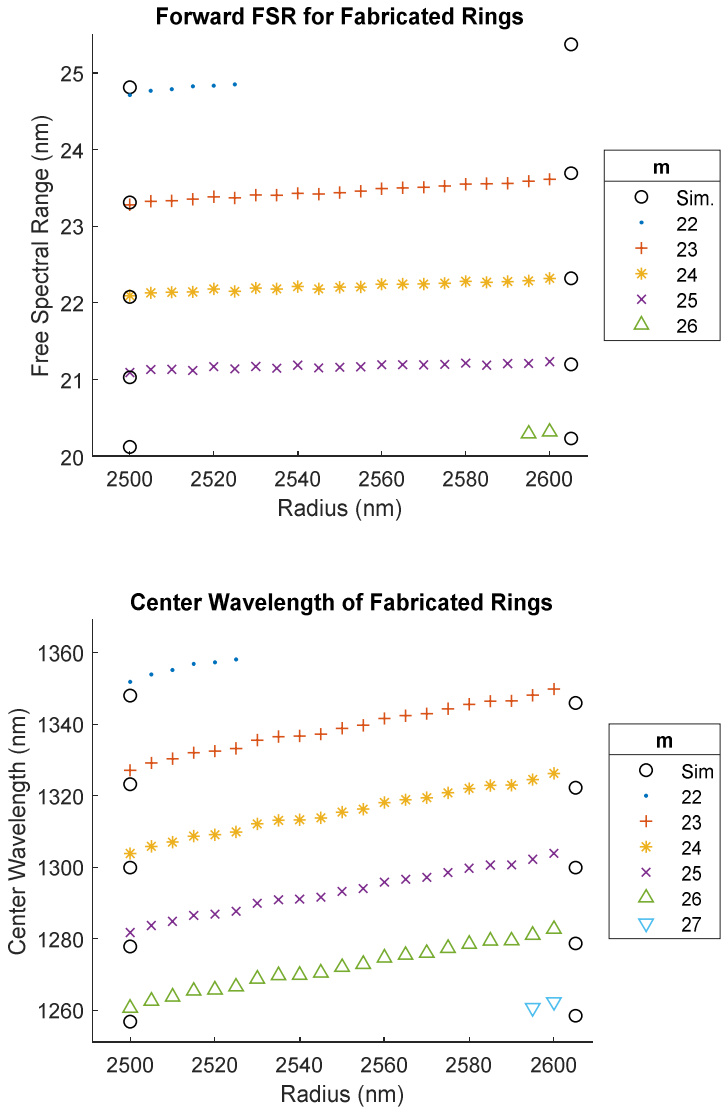

Figure 6.10. Forward *FSR* (upper) and center wavelength (lower) of fabricated rings vs. radius, with assigned *m* values indicated and simulated values for $R = 2500$ µm and $R = 2605$ µm shown.

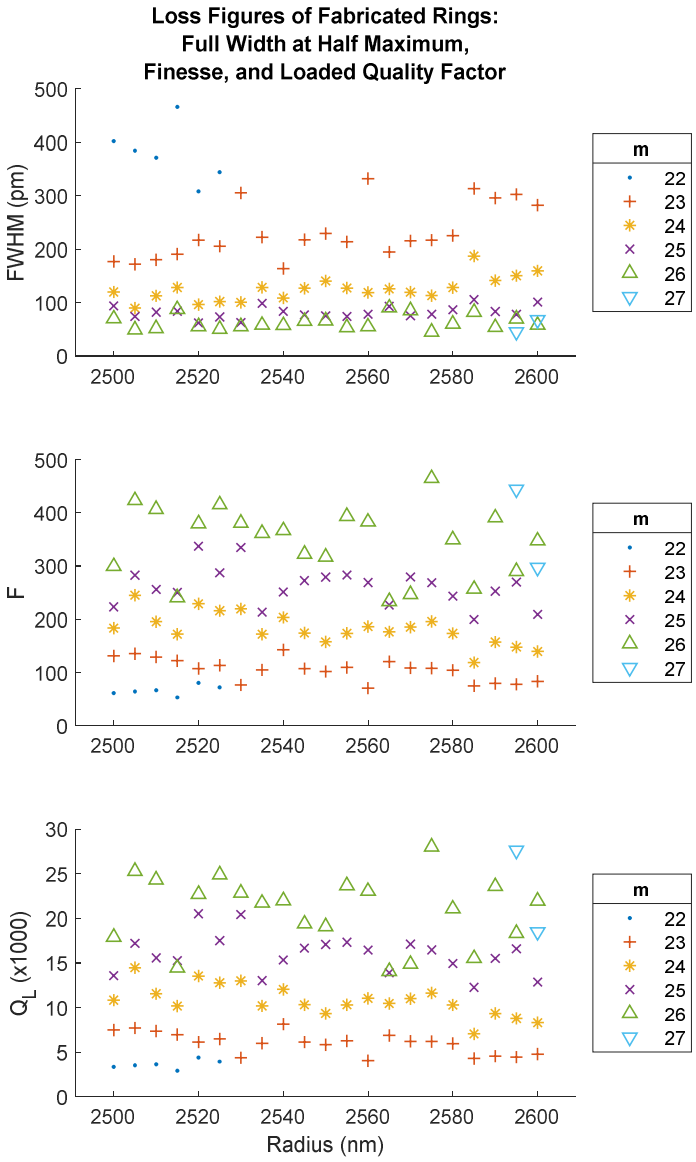

Figure 6.11. Loss figures of fabricated rings vs. radius: resonance full width at half maximum (*FWHM,* in pm, upper), finesse (*F*, center), and loaded quality factor (Q_L, in thousands, lower) for fabricated rings, with *m* values indicated.

The *m* value of each resonance was determined from the forward *FSR*, which proved to be an unambiguous identifier. Measured values matched those predicted by COMSOL simulation to within ±≤0.5%. Center wavelengths varied ±≤1 nm from the designed position due to fabrication error. Rings were identified based on the center wavelength of the $m = 26$ mode, being the highest order mode present for all rings. It was assumed that longer wavelength resonances belonged to larger radii rings, with the shortest wavelength $m = 26$ resonance being assigned to the $R = 2500$

nm ring, the largest wavelength $m = 26$ resonance being assigned to the $R = 2600$ nm ring, and the intermediate resonances disturbed similarly. Due to center wavelength variation of $\pm \leq 1$ nm caused by fabrication non-idealities, this was not an unambiguous identifier, and it is possible that assigned values differ from the actual value by 1-2 ring numbers. The use of a 5 nm beam step for EBL exposure as well as a 5 nm radius step proved to be less than ideal, as only a single extra "layer" of shots was added per ring. It would be better to use a smaller step size to increase this accuracy and smooth out the wavelength increase.

Regardless of initial fabrication variation, more accurate ring identification during measurement would have been possible with a few different methods. One is an IR camera [143], which could have been used to initially monitor the rings while the laser input wavelength was stepped manually. The relative position of the resonances could then have been recorded. Another method would be UV laser ablating excitation [131], which could have been to permanently change the resonances of rings to eliminate overlap. Before and after measurements could be used for ring number assignment. More complicated on-ring structures, such as on-ring heaters [129] or electrical modulators [144], could also have been used to identify or tune the resonances.

Video of the sensor was taken at points during the experimental period. Recordings that were later found to have coincided with detection events (DEs) were inspected. In some cases, it was confirmed that a cell was indeed over top of the sensing region of the assigned ring during the detection event, as seen in Figure 6.12.

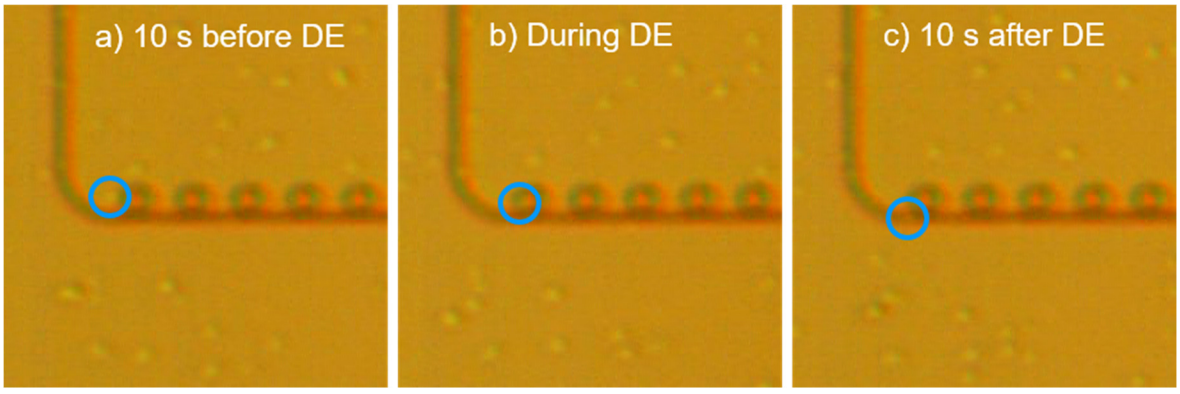

Figure 6.12. Position of a detected cell a) before, b) during, and c) after a detection event (DE) of the $m = 26$ mode of ring #1 ~106 minutes into measurement.

In other cases, no cell was observed at the assigned ring, but one or more cells were observed over top of the sensing region of a ring adjacent to (and thus ±1 ring number) from the assigned ring. These cases suggested that some of the ring numbers were mis-assigned due the ambiguous nature of the ring number assignment. In no cases where detection events occurred were neither the assigned nor adjacent rings observed to have a cell over top of the sensing region. It was common, however, to see a cell over top of the sensing region of a ring, but for no detection event to have been seen. This is not unexpected, as the fluidic channel is 120 μm high, but the sensing region only extends ~200 nm in the z direction. In these cases, cells were simply too far above the ring to be detected.

It was also seen that these experiments could not rule out the potential for more than a single cell to be in the sensing region of a ring at the time of a detection event, but that these would be due to a countably small number of cells (e.g. 2 or 3). The maximum number of cells that could potentially be in the vicinity of the ring at optimal packing in the Top binding condition would be 21. Detection events were observed resulting in shifts up to 78 pm, or 130σ. As such, this demonstration cannot claim to have definitively detected a single cell on a single ring (although this likely was indeed measured) but it can claim that discrete analyte resolution sensing was demonstrated, and that the single cell resolution sensing ability of the rings was confirmed. For example, the detection in Figure 6.12 caused a 21 pm shift. It cannot be definitively ruled out from the video that only the highlighted cell caused the entirety of the shift, as the region between rings 1 and 2 is blurry. However, even if a second (or third) cell happened to be present, the shift per cell (11 pm/cell, or 7 pm/cell, respectively) would still both exceed the 5 pm shift limit, and far exceed a shift due to noise (17.5σ/cell and 11.6 σ/cell, respectively).

6.4.4. Resonance behavior

With the *m* value and *R* of each resonance determined (as shown in Figure 6.10), the behavior of each ring during the measurement period could then be more closely inspected. As an example, the behavior of the resonances of ring #15 (R = 2570 nm) is shown in Figure 6.13. Each row displays the behavior of a different *m*. The X and Y scales of each column are to scale within the column.

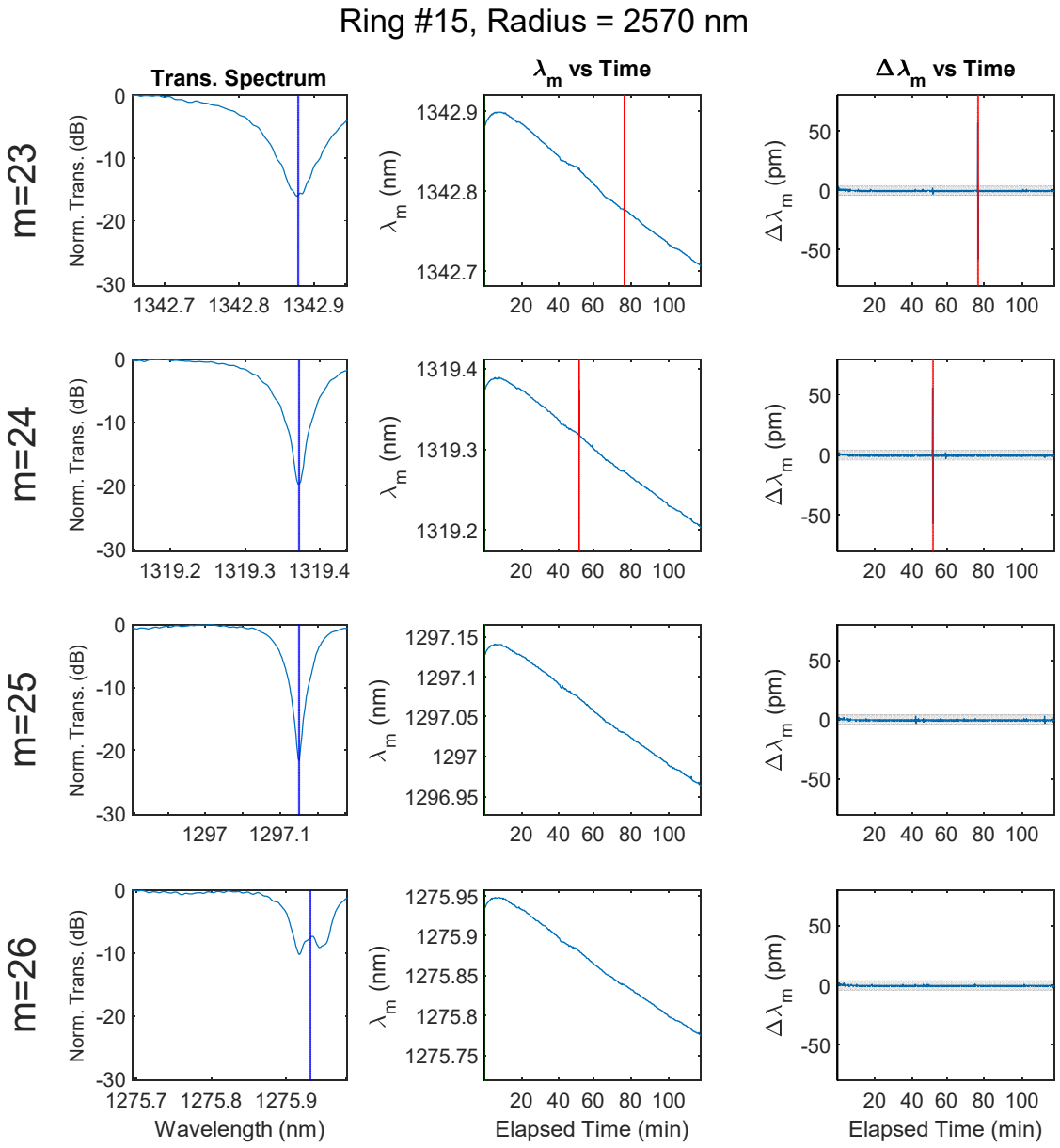

Figure 6.13. Resonance behavior of resonances of Ring #15 of sensor.

In Figure 6.13, the left most column shows the initial resonance shape and position (power vs. wavelength), with the center wavelength λ_m highlighted in blue. The center column shows λ_m vs time, with detection events highlighted in red. The right most column shows the scan-to-scan center wavelength shift $\Delta\lambda_m$ vs. time, with detection events highlighted in red, and the Y-axis region where wavelength shifts do not reach the threshold for a detection event $|\Delta\lambda_m| < \lceil 6\sigma_\lambda \rceil$ is overlaid with grey.

Ring #15 experienced two detection events, a 57 pm shift of the $m = 24$ mode about 52 minutes into measurement, and a 56 pm shift of the $m = 23$ mode about 75 minutes into measurement. It is notable that, for both detection events, none of the other resonances of the ring shift in a statistically significant way. The reasons for this will be further discussed later in section 6.4.10.

Additionally, the center wavelength of all resonances experiences a steady blue shift throughout the experiment. A similar blue shift was seen in experiments in chapter 5, which involved measurement of a water clad chip without an enclosure. This had been assumed to be due to evaporative cooling, as in those experiments water needed to be periodically added to replace that lost by evaporation. In this demonstration, however, no evaporation occurred. It was concluded this effect was due to the etching of the silicon waveguides in water [145]. The final value of this drift, seen in Figure 6.14, was seen to be similar for all rings, independent of radius, with variation in which ring shifted more or less. The resonances of each particular ring showed highly consistent shifts, with consistently slightly larger shifts for low m resonances than higher m resonances.

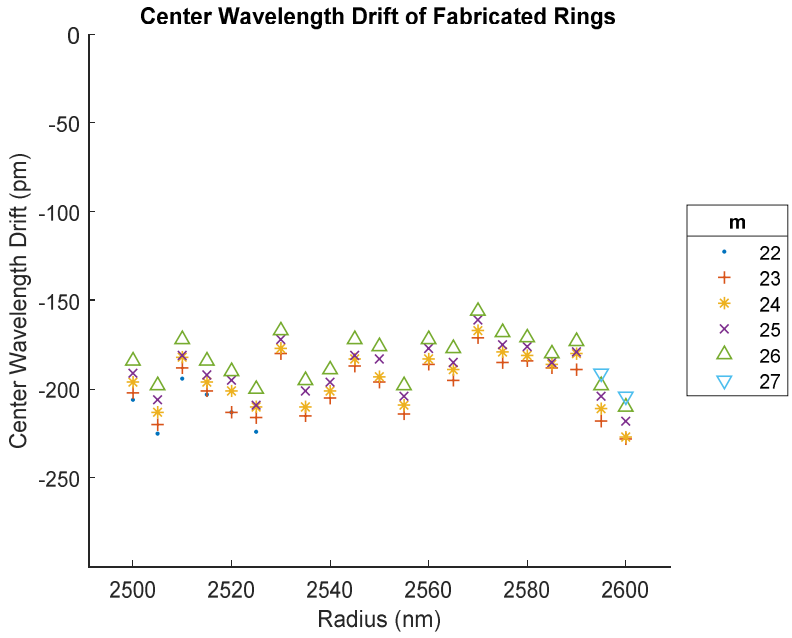

Figure 6.14. Final-to-initial resonance wavelength drift for measured sensor exposed to cell laden deionized water over 117 minutes.

6.4.5. Scan-to-scan resonance wavelength shift

The meaningful output of the sensor array is the scan-to-scan wavelength change for each resonance. With the *m* and ring number assigned to each resonance, these scan-to-scan wavelength changes can be grouped by ring and displayed by *m*. An example of the scan-to-scan wavelength change for all resonance of Ring #15 can be seen in Figure 6.15. Elapsed time is plotted on the X axis and mode number is plotted on the Y axis. The change is identified by the color of the relevant pixel, with yellow tones indicating a positive shift, blue tones indicating a negative shift, and green tones indicating no shift. Mode numbers from 22 to 27 are plotted, as this is the full range of *m* values for all the fabricated rings. For Ring #15, however, only *m* values from 23, 24, 25, and 26 were part of the scanned spectrum, and thus the values for $m = 22$ and $m = 27$ are all zero.

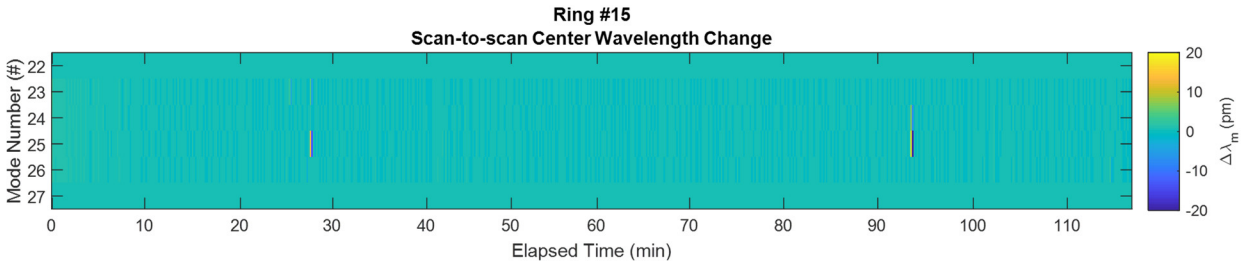

Figure 6.15. Scan-to-scan center wavelength change of a single ring (Ring #15) in the measured sensor.

Plots such as Figure 6.15 can be made for each ring in the array and combined to give a comprehensive picture of sensor behavior, displaying the shifts for each ring throughout the measurement period. A plot such as this is seen in Figure 6.16. The Y axis contains the *m* values for each ring, from 22 to 27, with 22 being at the top of the ring area and 27 being at the bottom. These plots, with 6 *m* values for each ring, are stacked together on the Y axis with each ring number labeled. As in Figure 6.15, the X axis is the elapsed time from the start of measurement, and color tones of each pixel identify the shift at the resonance and time. The maximum shift was found to be 78 pm. In order to more clearly show behavior at small shifts and generally enhance contrast, the resonance shift plot can be capped at ± 20 pm. This is shown in Figure 6.17.

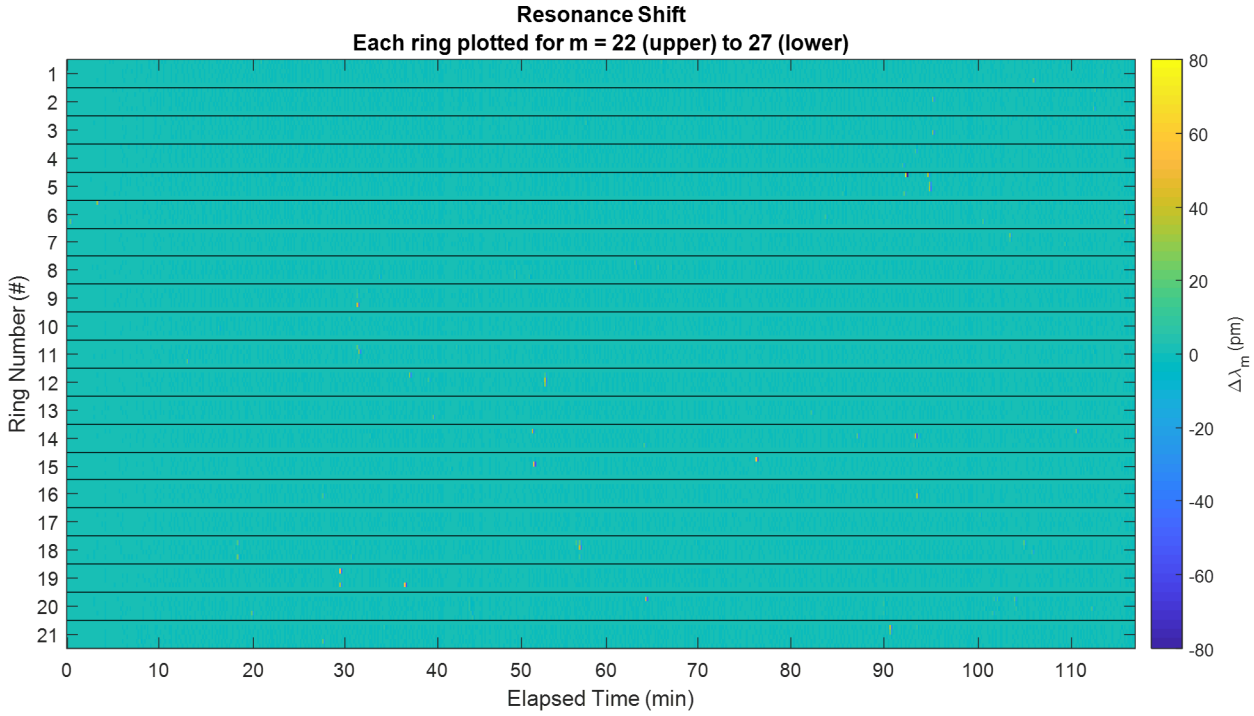

Figure 6.16. Full scale resonance wavelength shifts for all rings in the measured sensor.

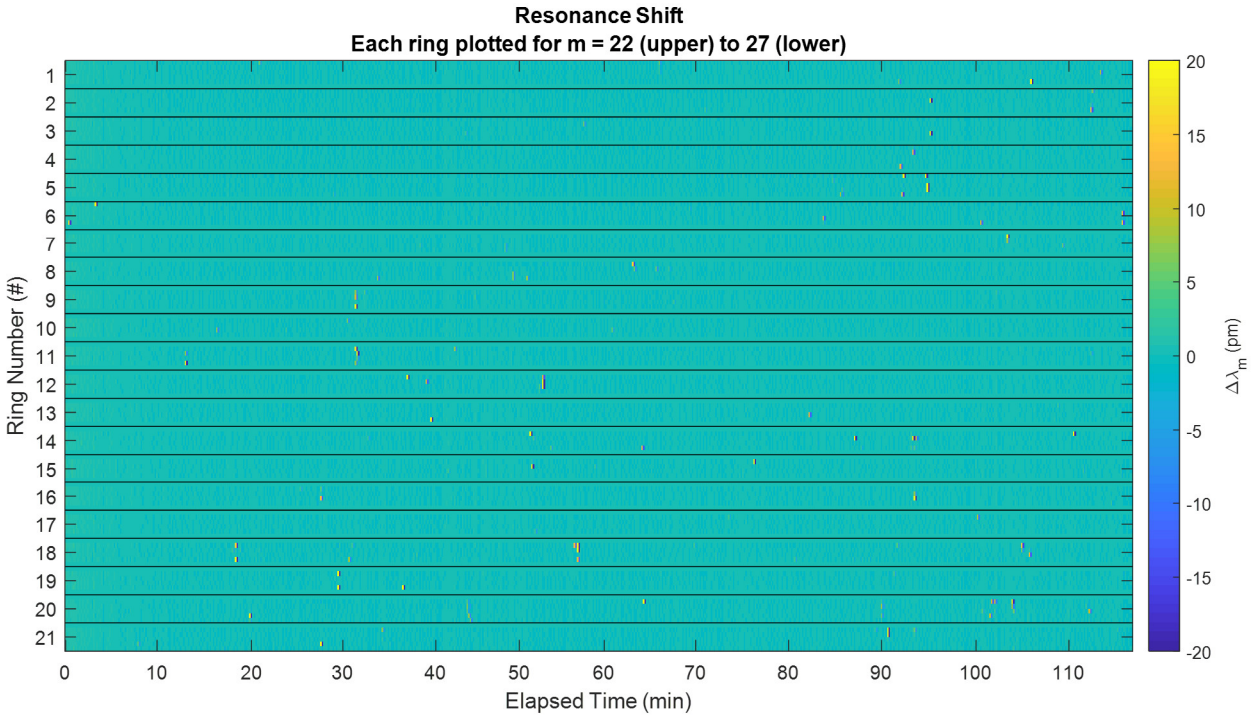

Figure 6.17. Limited scale (± 20 pm) resonance wavelength shifts for all rings in the measured sensor, to enhance contrast.

6.4.6. Detection events

As discussed in section 6.4.1, a detection event at a particular resonance is defined as the result of three conditions: 1) a shift $\Delta\lambda_{m,1} \geq 5$ pm and $\Delta\lambda_{m,1}/FWHM \geq 1/50$, 2) the following scan having a shift $\Delta\lambda_{m,2} = -\Delta\lambda_{m,1} \pm 1$ pm, and 3) upon inspection, the entire is seen to shift clearly and unambiguously. 93 detection events were found. These can be seen in Figure 6.18.

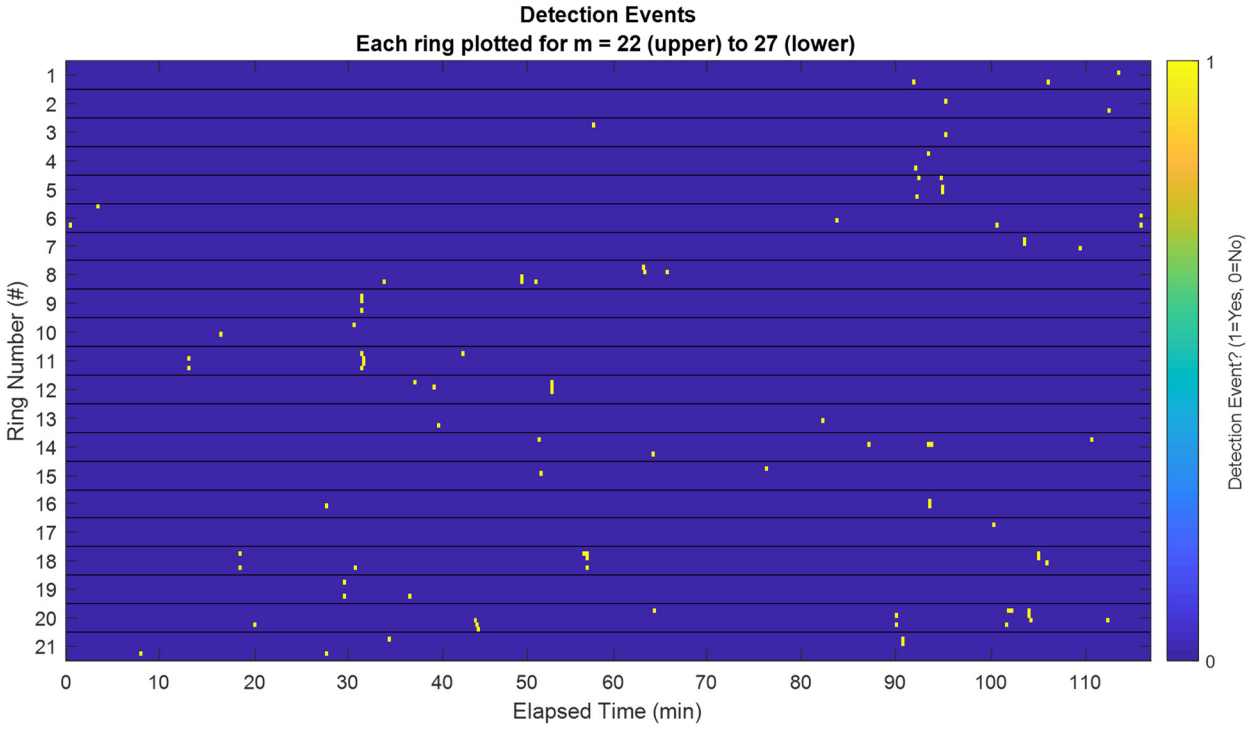

Figure 6.18. Detections events for the measured sensor.

Notably, the first detection event occurred less than a minute after measurement began. Additionally, it had been assumed that detection events would be more common as time went on, with cells settling due to gravity. That was not seen to be the case, potentially because the 2-hour time scale was too small for significant settling to take place.

6.4.7. Detection event wavelength shifts

The detection event resonant wavelength shift $\Delta\lambda_m$ of each detection event is shown in Figure 6.19, with the five largest shifts (shifts greater than or equal to 50 pm) identified with a red circle. $\Delta\lambda_m$ cannot be claimed to be equal to the discrete analyte sensitivity S_d because it is possible that more than a single cell was present to cause any particular shift. In the case that only a single cell is present, $\Delta\lambda_m = S_d$.

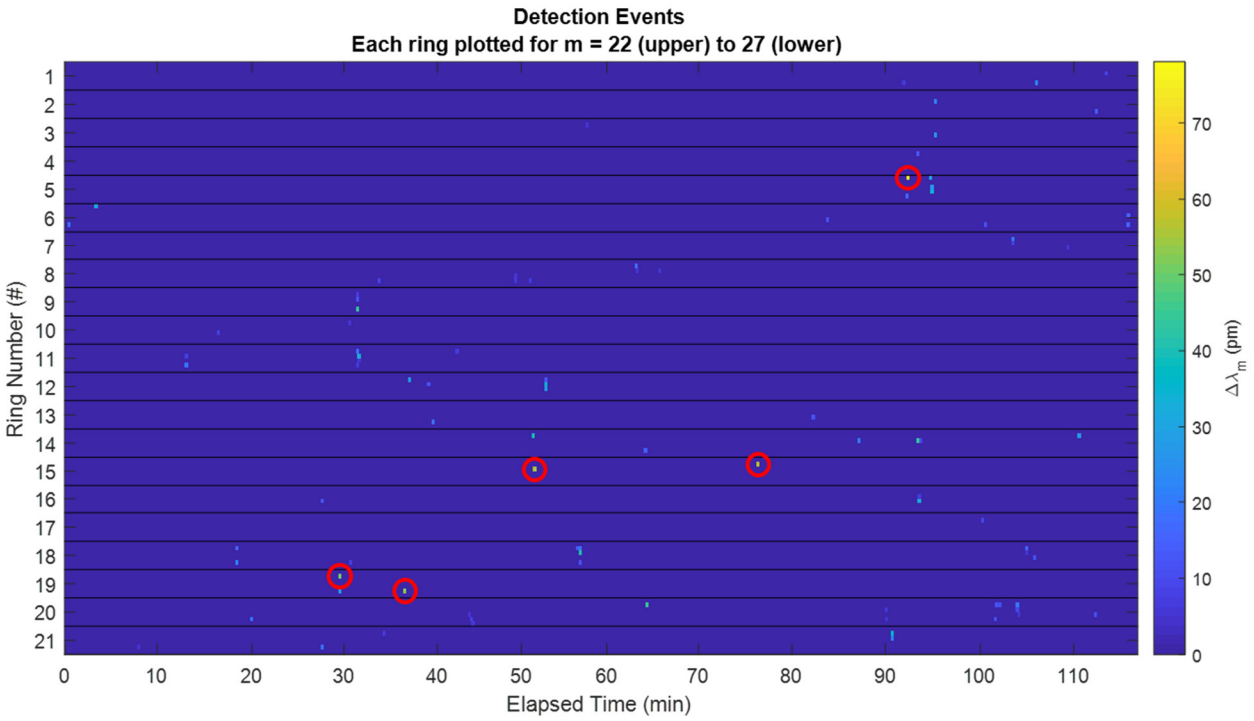

Figure 6.19. Resonance wavelength shifts of detection events for the measured sensor, with the five largest shifts circled.

The maximum $\Delta\lambda_m$ = 78 pm (130σ_λ) would be roughly equivalent to a single cell in the Tee or Top biding condition ~50 nm from the waveguide (based on estimates from full 3D simulation). In total, 5 shifts were greater than or equal to 50 pm (83σ_λ). As was previously seen in Figure 6.9, small shifts are most common, which is expected based on the random motion of the cells in solution.

6.4.8. Detection event sensed analyte optical size

As the free spectral range for each resonance was known, the sensed analyte optical size $\ell\Delta n_{eff}/\lambda$ could be determined from the wavelength shift $\Delta\lambda_m$. This is shown in Figure 6.20, with the five largest values (greater than or equal to 2.1 mRIU) identified with a red circle. These five largest values are the same detection events as are highlighted in Figure 6.19, which is expected because *FSR* varies much less than the observed shifts. The maximum optical perturbation was found to be 3.1 mRIU. From Table 4.1, this could be a cell in the "Outer Corner" geometry 5 nm from the waveguide. The smallest sensed analyte optical size in a successful detection event was 0.21 mRIU.

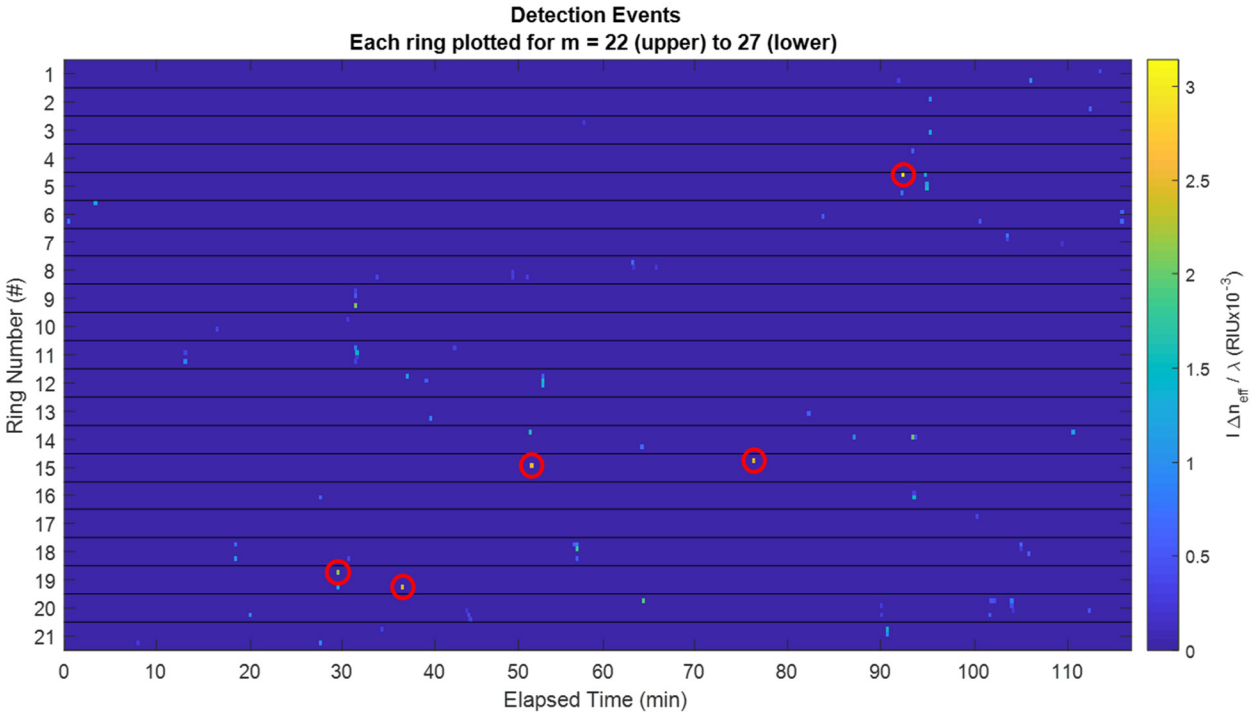

Figure 6.20. Sensed analyte optical size of detection events for the measured sensor, with the five largest values circled.

Figure 6.21 shows a 2D+z simulation of a cell above a waveguide in the Top binding condition with varying cell to waveguide distance for TE/TM O/C-band waveguides. Note that the value for a Top bound TM O-band waveguide in this simulation gives a sensed analyte optical size of 3.2 mRIU, while full 3D simulation predicted a value of 4.2 mRIU. This discrepancy is due to greater

delocalization, and therefore sensitivity, when the waveguide is curved with a radius of 2.5 μm compared to a straight waveguide used for the 2D+z simulation. For simplicity, the 2D+z values are used for comparison, and it should be noted that this comparison is very rough.

For the 2D+z simulation, the maximum sensed value of 3.1 mRIU corresponds to a cell in the Top position 7 nm away from the waveguide. The minimum of 0.21 mRIU would correspond to a Top geometry cell 165 nm from the waveguide. For comparison, the sensed analyte optical size of other ring designs (C-band, and TE mode) are shown. It is worth noting that taking the 0.21 mRIU minimum sensed analyte optical size for the TE mode would only detect Top position cells ≤ 30 nm from the waveguide, a more than 5-fold decrease in maximum sensing height.

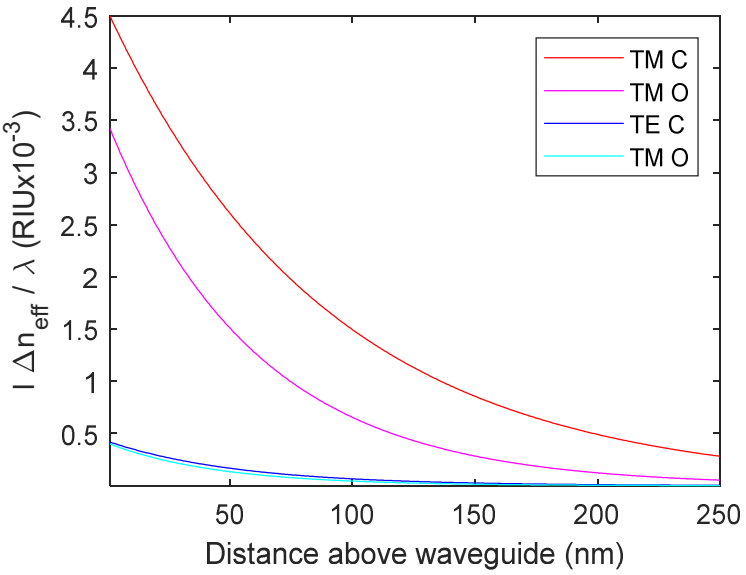

Figure 6.21. 2D+Z simulation of sensed analyte optical size vs. distance above the waveguide for a cell in the Top binding condition for TE/TM and O/C-band waveguides.

6.4.9. Detection event fractional wavelength shift

The fractional shift $\Delta\lambda_m/FWHM$ of each detection event can be seen in Figure 6.22. If these events could be said to occur due to a single cell, $\Delta\lambda_m/FWHM$ would be equal to the discrete analyte figure-of-merit FOM_d. Without that certainly, they are labeled more generally as the fractional shift. The largest fractional shift was 0.98, equating to a shift of nearly once resonance width. A

total of 4 shifts were seen above a value of 0.5. These are highlighted in Figure 6.22 with red circles.

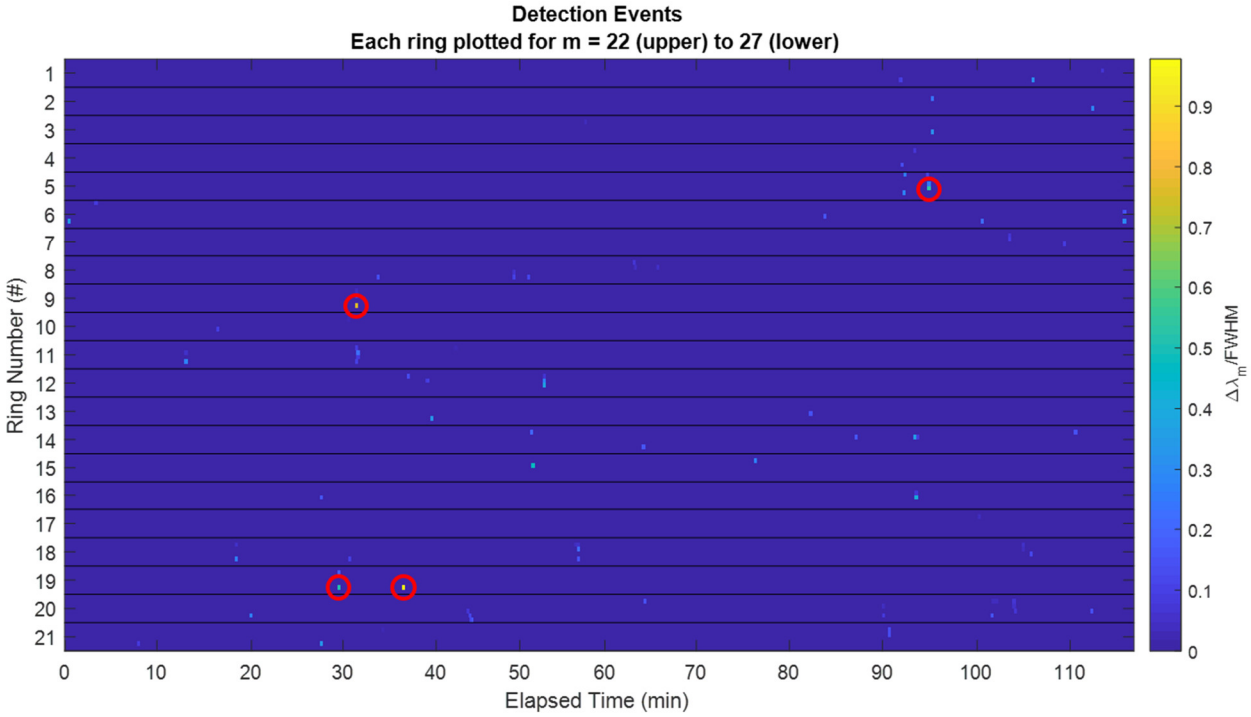

Figure 6.22. Wavelength shift per wavelength full width at half maximum (*FWHM*) for each detection event of the measured sensor, with the 4 largest values circled.

It should be noted that three out of the four largest values of these events are distinct from the detection events highlighted in Figure 6.19 and Figure 6.20. This is because smaller *m* value resonances have both higher sensitivity and lower *F*. As a result, the largest fractional shifts tend to be higher *F* resonances (higher *m*) than seen previously.

6.4.10. Adjacent detection events

Adjacent detection events can be defined as 2 or more consecutive *m* value detection events from the same ring, each measured 0.5 s apart. Adjacent detection events are highlighted in Figure 6.23. It was initially assumed before this measurement analysis that all detection events would have adjacent detection events due to the presence of any cell. However, measurement results showed that only 23% of detection events had a shift of an adjacent *m* in the same ring. A more careful

consideration of the motion of the cells in solution, which are governed by Brownian motion as they are not bound to any ring, shows that these should indeed be uncommon, as was measured.

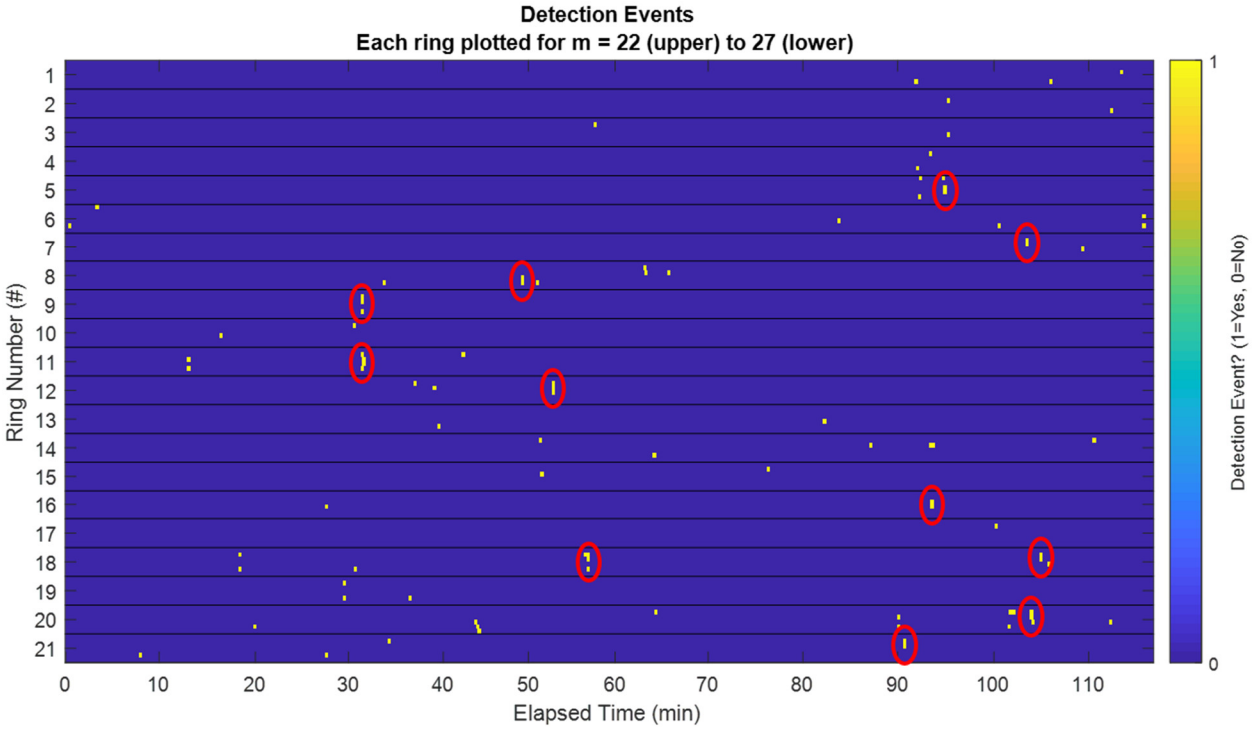

Figure 6.23. Detection events of the measured sensor, with adjacent detection events circled.

The time between scans of resonant peaks for a particular ring is 0.5 s, and the time between each measurement scan is 10 – 11 s. The typical diffusion coefficient for non-motile *E. coli*, which includes the TOP10 *E. coli* used in this work, is D ≈ 0.5 μm^2/s [146]. To very roughly estimate the expected diffusion time for the lengths considered here, in a 2D cross-section, the root mean squared displacement is $r_{rms} = \sqrt{\langle r^2 \rangle} = \sqrt{4Dt}$. Thus, for t = 0.5 s the expected r_{rms} = 1 μm, and for t = 10 s the expected r_{rms} = 4.5 μm. The interaction length for the $\lceil 6\sigma \rceil$ noise condition is approximately 200 nm on top of the waveguide, and 100 nm on the sides. The total sensing area formed around the center of the waveguide is then +200 nm in z, and ±275 nm in r. It should then take ~0.17 s (170 ms) to diffuse entirely across the sensing area (for 200 nm in Z, 550 nm in r, for a total of 585 nm). Diffusion out of only the Z plane (200 nm) would be expected to take 20 ms, and 275 nm of diffusion out of the r plane would be expected to take ~38 ms. Therefore, without

chemical functionalization, it should be expected that a cell will move out of measurement range before the next *m* value for a particular ring is scanned.

6.4.11. Corroborated detection events

Corroborated detection events can be defined as at least two detection events for a ring which occur on either the same scan, or within one scan of one another. A plot of corroborated detection events can be seen in Figure 6.24. It is notable that 57% of detection events are part of a corroborated detection event. This suggests that, as a detected cell is likely to diffuse out of the ring's sensing volume, it may also diffuse back into it, and may be detected on non-adjacent *m* values or as part of the next scan. It should be noted that these cannot be distinguished from a different cell being present and detected, but the fact that most detection events are corroborated suggests that they are not due to the coincidental presence of different cells.

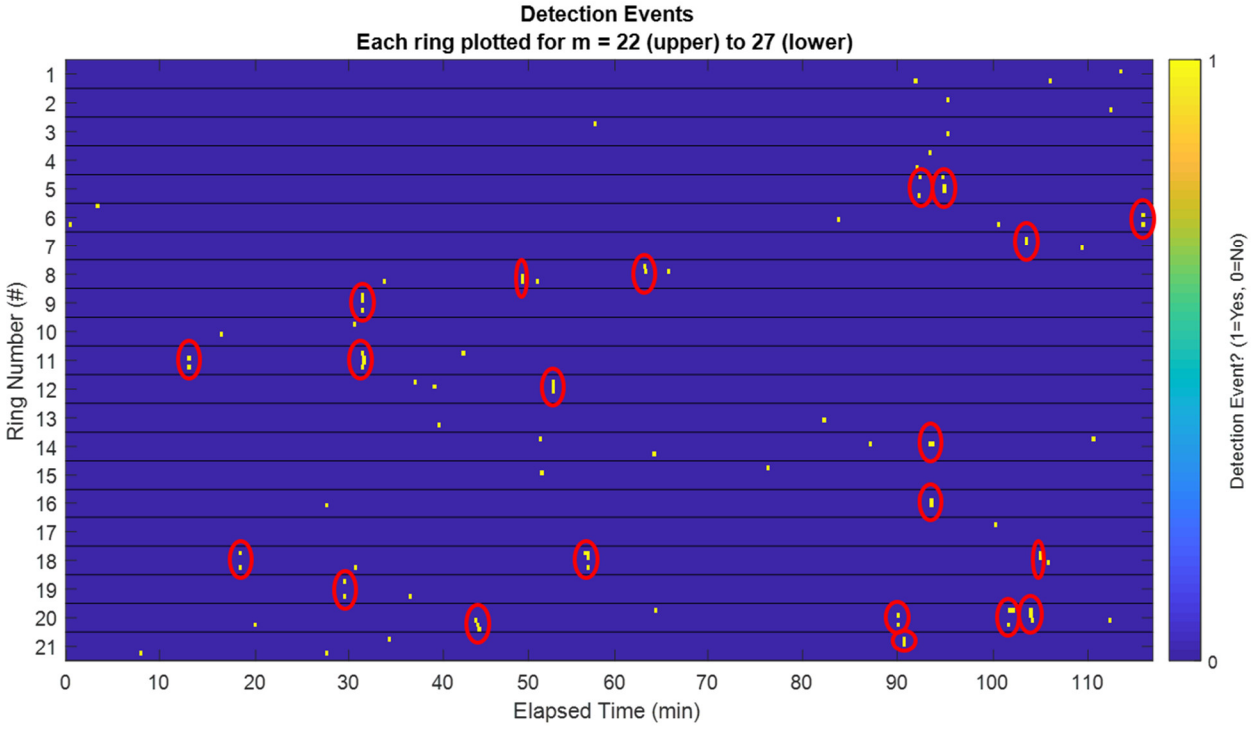

Figure 6.24. Detection events of the measured sensor, with corroborated detection events circled.

6.5. Summary

In summary, a fabricated 21 ring array sensing device, consisting of TM O-band rings of radii evenly distributed between 2.5 μm and 2.6 μm, was exposed to a solution of *E Coli* with concentration ~10^7 CFU/mL. A total of 679 scans were measured over a 117 minute time frame, with scans being taken every 10 to 11 seconds. Each of the 92 resonances in the spectrum of the sensor was assigned to a mode number based on its *FSR* by matching the observed and predicted *FSR* values. Each resonance was also assigned to ring number based on the center wavelength of the $m = 26$ mode, assuming longer wavelength resonances correlated with larger radii rings. Based on stringent detection criteria, 93 detection events were observed. 23% of detection events were seen to be adjacent to another detection event, and 57% of detection events were corroborated by another detection event. The largest wavelength shift observed was 78 pm, and the largest fractional wavelength shift was 0.98. Video inspection was used to confirm that cells were indeed potentially present in the sensing volumes of rings showing resonance shift, and that a countably small number of cells were responsible for shifts (e.g. 1, 2, or 3). As the shifts seen were large enough to exceed the noise floor even divided between a countably small number of cells, it was concluded that this experimental proof of concept demonstrated the ability of the optimized rings to detect bacterial cells with discrete analyte resolution.

This proof of concept demonstrates that the prior analysis, computational simulation, optimization, and photoresist simulant approaches are valid, at least to the point of being able to detect discrete bacterial analytes. While single cell sensing cannot be unequivocally claimed based on this demonstration, the observed wavelength shifts are large enough to be able to infer that individual bacterial cells may be detected above the detection limit. As only a single demonstration of sensing with bacteria was done, no information may be projected about the minimum detection limit of the devices. The main limiting factor in this metric is analyte delivery, and the tested setup was not optimized for this. However, as this work focuses on the optical design and optimization, the design and approach here may of use for other researchers designing an integrated system that also includes chemical analyte binding and an optimized microfluidic analyte delivery method.

7. CONCLUSION

7.1. Summary

This work presented the design, computational simulation, experimental photoresist cellular simulation, and experimental proof of concept demonstration of a ring resonator sensor optimized for the detection of discrete biological analytes. By analyzing the sensing interaction between a microring and a single analyte as a binding event, this work demonstrates that the sensing response to individual analytes can be greatly enhanced. It was shown that the commonly used sensing equations for cladding sensitivity, while certainly valid for uniform detection of fluids and homogeneously dispersed molecules, do not fully capture the subtleties of discrete analyte binding.

The derived discrete analyte sensitivity and discrete analyte figure of merit describe the sensing response of a ring resonator due to the inherently inhomogeneous binding of discrete analytes. The discrete analyte sensing equations become equal to the cladding sensing equations if a ring is uniformly and homogeneously saturated. The discrete analyte sensing equations reveal a common factor, the sensed analyte optical size, that must be computationally derived based on the ring, the analyte, and all potential binding geometries. The remaining factors, the free spectral range and finesse, can be determined experimentally outside of sensing applications. With the help of these equations, one can optimize an optical ring resonator sensor for use with an analyte of interest with relative ease. This optimization approach was confirmed both with precise non-biological experiments and experimental biological proof of concept.

The particular optimizations that made the single cell resolution sensitivity shown here possible were:

1) Working with silicon waveguides, as opposed to lower refractive index, but lower loss, materials such as high index glass or silicon nitride.
2) Working at the TM polarization instead of the more common TE polarization
3) Working in the O-band wavelength range instead of the more common C-band, which decreases losses due to water absorption by an order of magnitude

4) Working with small radius, high finesse resonators instead of the commonly used large radius resonators focused on the highest attainable quality factor

Silicon is a common material for rings, and the TM mode is often used in biosensing applications. However, operation in the O-band regime is extremely rare, and its use here in cellular sensing is a novel contribution of this work. A focus on finesse, instead of quality factor, is also a novel contribution. High finesse design makes the O-band particularly desirable, and makes the combination of small radius, TM O-band operation more than the sum of its constituent parts.

Through this optimization, it was shown that the designed high finesse and high sensitivity resonator was capable of robust single analyte resolution sensing, with *E. Coli* as a model analyte. However, a single such sensor is of limited use, and thus the rings were arrayed into a sensing array to increase the total sensing volume of the device. This again relied on finesse, which is directly equal to the multiplexing ability of a ring. A maximally multiplexed device (limited by the beam step size of the electron beam lithography tool) was fabricated and shown experimentally to have demonstrated discrete analyte resolution sensitivity.

The developed optimization approach for microrings in high sensitivity sensing applications is broadly applicable to other bacteria aside from *E. coli* and can be extended to other microbes such as viruses. The approach also allows for comparison of a variety of ring designs, materials, and enhancements. The fact that sensitivity to discrete analytes depends on the sensed analyte optical size and the cavity free spectral range, and that the discrete analyte sensing figure of merit depends on the sensed optical size and cavity finesse, allows for general ring design modifications to be evaluated against one another.

The radius dependence of discrete analyte sensitivity allows not only for high sensitivity design, but also the design of high dynamic range sensing devices. If it is not desirable to detect cells with single analyte resolution, the size of the cavity can be increased as desired. The decrease in finesse will be obvious, and rings can be proportionally removed from a sensing array to maintain working device.

7.2. Conclusion and discussion

In conclusion, with the goal of a maximally sensitive integrated and multiplexable cellular biosensor, this work has rigorously analyzed the binding of a discrete cellular analyte to a microring resonator and shown with experimental proof of concept that single analyte resolution sensing of unicellular bacterial analytes is feasible with silicon microring resonators operating in the TM mode O-band near 1310 nm. Although single cell *resolution* is separate from the more stringent case of single cell *detection* (defined as detecting a single cell in a volume of fluid (e.g. 1 CFU/mL) vs. a single cell bound to the detector), it represents a necessary condition and motivates measurement in a microfluidic system with biological analytes. Furthermore, the use of cavity finesse as part of the discrete analyte sensing of merit has not only the effect of maximizing sensitivity, but also minimizing sensor footprint and inherently optimizing for wavelength division multiplexing on a single waveguide channel.

Though discussion focused on the most difficult case of single cell resolution sensing, in an experimentally realized practical sensing system (a limited version of which was seen in chapter 6) it will be common for multiple cells to bind to a properly functionalized ring resonator sensor. The effect of multiple cell bindings will be a nearly linear shift of the resonance wavelength, with the degree of linearity determined by the specific binding locations and orientations of the attached cells. Although the Q of the ring may decrease slightly as cell scattering losses increase, multiple cell bindings will create a significant shift in refractive index and remain the dominant phenomena that affects the performance of the sensor. By looking at the case of single cell detection, we have analyzed the most taxing case, and additional cell bindings will serve to further increase the signal-to-noise ratio of the sensor.

7.3. Potential future directions and improvements

7.3.1. Integration with chemical functionalization and optimized microfluidics

It would be desirable to determine the minimum detection limit of an optimized ring in a full lab-on-chip demonstration, with optimized chemical functionalization and optimized microfluidics. It would also be helpful to include one of the ring identification methods described in section 6.4.3.

7.3.2. Solution to water etching the exposed silicon limiting the sensor lifetime

Throughout testing in aqueous solutions (18 MΩ reverse osmosis deionized water, potentially with the addition of diluted *E. coli*), a small but persistent blueshift (towards smaller wavelengths) in the resonance spectra of the rings was observed. It was initially assumed that this was due to evaporation, as initial testing was done with drops of liquid on the surface of the chip, and as the water evaporated it had to be replenished. However, the thermo-optic coefficient of silicon results in a shift of only ~50 pm/K for TM O-band rings, as seen in Table 3.1, much smaller than the observed shift. Longer exposure to water in closed microfluidics channels revealed a similar drift, even though evaporated was eliminated.

Exposure of the chip in chapter 6 to the microfluidic environment for 72 hours rendered the rings completely unusable, despite the waveguides still being visible under the microscope camera. This was determined to be a result of the etching of the unprotected silicon waveguides by the aqueous solution, which apparently increased loss or changed the coupling gap enough that resonances were no longer visible in the wavelength spectrum. Recent work [145] has explored this effect more thoroughly and demonstrated that a thin (~10 nm) layer of silicon dioxide is sufficient to protect silicon devices from etching by water for substantial periods of time. This would require thermal oxidation of the fabricated ring structures, which would require a revisit of the waveguide design, but should not otherwise negatively impact the use of the rings or substantially degrade their performance. However, this would need to be confirmed experimentally, especially to see if any negative consequence exists for the coupling gap.

7.3.3. Radius and waveguide dimension could be more rigorously optimized for finesse

The optimization in chapter 4 relied on a relatively rough method of optimizing finesse with radius. As was seen in Figure 4.8, bend limited finesse for the 220 nm by 350 nm silicon TM O-band ring peaks around 4 μm. However, rings in chapter 5 were only fabricated at relatively spaced out values: 1.25 μm, 2.5 μm, and 3.75 μm. It was seen in chapter 6 (especially Figure 6.2) that, for a 2.5 μm resonator, finesse values depended heavily on wavelength and mode number. In Figure 6.11, it was seen that a slight radius increase from 2.5 μm to 2.6 μm did not affect finesse strongly. However, a more thorough search in the range of 1.25 μm to 3.75 μm could be done to see if a

"more" optimal radius exists for high finesse operation. Finesse is heavily dependent on mode number and working at a slightly higher mode number at the low end of the wavelength spectrum (1260 - 1280 nm) may be able to increase beyond the limiting value of ~450 observed here.

Additionally, the choice of a 220 nm by 350 nm waveguide was due to it offering a good balance of sensitivity for the TE and TM modes and showing roughly optimal sensitivity. However, it may be the case that a slightly larger waveguide may increase finesse far more than it decreases sensitivity. The same may be true for a slightly higher waveguide height. Either of these changes would necessitate re-looking at optimal radius as well as coupling gap.

It would be relatively straight forward to start with a particular chip height and fabricate waveguides of varying width, coupling gap, and radius. It would be more difficult, but still doable, to also start with a thicker initial silicon thickness (e.g. 300 nm) and etch this down progressively with either ICP RIE or alternating Piranha cleans and BOE strips to thin the top. This could then give a fuller optimization of finesse.

7.3.4. Reduction in fabrication loss and waveguide roughness

As seen in Figure 5.2, the fabricated microrings had relatively rough sidewalls. This could be due to the 5 nm beam step size used for EBL exposure, or to the particular recipe of ICP RIE etch. Sidewall roughness will generally degrade finesse, and it would be useful to optimize the fabrication process to minimize this.

7.3.5. Exploration of more sensitive geometries with smaller analytes

The strip waveguide used here is convenient for fabrication and useful for cellular sensing, but more sensitive fabrication geometries such as slot rings [147] and subwavelength grating rings [148] would be interesting to explore with nanoscale analytes such as viruses [32]. These more sensitive geometries will enhance the sensed analyte optical size compared to a strip waveguide but will also result in decreased finesse. A full exploration would be required to determine if single virus resolution sensing would be possible in a ring with a more sensitive waveguide geometry.

7.3.6. Exploration of the visible range

Similar to how the O-band was desirable compared to the C-band due to lower water absorption, the visible range offers still lower absorption. Silicon strongly absorbs light in this range, but silicon nitride is transparent. It could be useful to explore the achievable finesse of silicon nitride resonators in the visible range, whether this finesse is higher than that shown here, and what the sensed analyte optical size would be. If the finesse can be substantially increased, the relatively lower sensitivity of silicon nitride may still result in a higher discrete analyte figure of merit. Additionally, the visible range offers interesting opportunities for directly seeing which ring is being probed, viewing scattering off cells, etc.

7.3.7. Demonstration of a high dynamic range sensor

As discrete analyte sensitivity, via the free spectral range, in inversely proportional to ring radius, it is possible to decrease the sensitivity of a ring by increasing its radius. A chip with a series of device arrays, each varying the radii of rings and the number of rings, could be fabricated to experimentally demonstrate high dynamic range behavior. It would be desirable to keep the total sensing volume of the array constant, so a doubling of the radius should be accompanied by a halving of the number of rings in the array. This would be particularly interesting if an array of ~200 rings (per Table 6.1) could be achieved with an EBL tool with 0.5 nm beam step size, as two orders of magnitude of dynamic range could potentially be achieved.

7.3.8. Chemical functionalization, limiting the “active” area

As the chemical functionalization in a full sensor implementation relies on binding to surface hydroxide groups present in the native oxide of silicon (typically proceeding via silanization), binding will also occur for areas of exposed oxide substrate [35]. This could be potentially avoided through deposition of an anoxic surface layer on the exposed area of the chip, aside from the sensing rings. The usefulness of materials such as gold or anoxic dielectrics could be considered for this purpose.

LIST OF REFERENCES

[1] "Outbreak of E. coli Infections Linked to Romaine Lettuce (Final Update)," Centers for Disease Control and Prevention. https://www.cdc.gov/ecoli/2018/o157h7-11-18/index.html

[2] "E. coli O157:H7 Infections Linked to Romaine Lettuce," Centers for Disease Control and Prevention. https://www.cdc.gov/ecoli/2018/o157h7-04-18/index.html

[3] J. P. S. Cabral, "Water Microbiology. Bacterial Pathogens and Water," Int. J. Res. Public Health **7**(10), 3657-3703 (2010). https://doi.org/10.3390/ijerph7103657

[4] E. M. Marlowe and M. J. Bankowski, "Conventional and Molecular Methods for the Detection of Methicillin-Resistant *Staphlococcus aureus*," J. Clin. Mocrobiol. **49**(9), S53-S56 (2011). https://doi.org/10.1128/jcm.00791-11

[5] R. Quintiliani Jr and R. Quintiliani, "Inhalational anthrax and bioterrorism," Curr. Opin. Pulm. Med. **9**(3), 221-226 (2003). https://www.ncbi.nlm.nih.gov/pubmed/12682568

[6] J. E. Sheridan, J. Nelson, and Y. L. Tan, "Studies on the 'Kerosine Fungus' *Cladosporium resinae* (Lindau) De Vries Part I. The Problem of Microbial Contamination of Aviation Fuels," Tuatara **19**(1), 21-40 (1971).

[7] X. Zhao, C.-W. Lin, J. Wang, and D. H. Oh, "Advances in Rapid Detection Methods for Foodborne Pathogens," J. Microbiol. Biotechnol. **24**(3), 297-312 (2014). https://www.ncbi.nlm.nih.gov/pubmed/24375418

[8] A. Ahmed, J. V. Rushworth, N. A. Hirst, and P. A. Millner, "Biosensors for Whole-Cell Bacterial Detection," Clinical Microbiology Reviews **27**(3), 631-645 (2014). https://doi.org/10.1128/cmr.00120-13

[9] W. Bogaerts, P. De Heyn, T. Van Vaerenbergh, K. De Vos, S. K. Selvaraja, T. Claes, P. Dumon, P. Bienstman, D. Van Thourhout, and R. Baets, "Silicon microring resonators," Laser Photonics Rev. **6**(1), 47–73 (2012). https://doi.org/10.1002/lpor.201100017

[10] P. De Heyn, B. Kuyken, D. Vermeulen, W. Bogaerts, and D. Van Thourhout, "High-performance low-loss silicon-on-insulator microring resonators using TM-polarized light," in *Optical Fiber Communication Conference*, Technical Digest (CD) (Optical Society of America, 2011), paper OThV2. https://doi.org/10.1364/ofc.2011.othv2

[11] J. Niehusmann, A. Vörckel, P. H. Bolivar, T. Wahlbrink, W. Henschel, and H. Kurz, "Ultrahigh-quality-factor silicon-on-insulator microring resonator," Opt. Lett. **29**(24), 2861-2863 (2004). https://doi.org/10.1364/ol.29.002861

[12] S. Xiao, M. H. Khan, H. Shen, and M. Qi, "Compact silicon microring resonators with ultra-low propagation loss in the C band," Opt. Express **15**(22), 14467-14475 (2007). https://doi.org/10.1364/oe.15.014467

[13] A. Gondarenko, J. S. Levy, and M. Lipson, "High confinement micron-scale silicon nitride high Q ring resonator," Opt. Express **17**(14), 11366-11370 (2009). https://doi.org/10.1364/oe.17.011366

[14] S. Xiao, M. H. Khan, H. Shen, and M. Qi, "Modeling and measurement of losses in silicon-on-insulator resonators and bends," Opt. Express **15**(17), 10553-10561 (2007). https://doi.org/10.1364/oe.15.010553

[15] Q. Xu, D. Fattal, and R. G. Beausoleil, "Silicon microring resonators with 1.5-μm radius," Opt. Express **16**(6), 4309-4315 (2008). https://doi.org/10.1364/oe.16.004309

[16] J. Song, X. Luo, J. S. Kee, K. Han, C. Li, M. K. Park, X. Tu, H. Zhang, Q. Fang, L. Jia, Y.-J. Yoon, T.-Y. Liow, M. Yu, and G.-Q. Lo, "Silicon-based optoelectronic integrated circuit for label-free bio/chemical sensor," Opt. Express **21**(15), 17931-17940 (2013). https://doi.org/10.1364/oe.21.017931

[17] K. De Vos, I. Bartolozzi, E. Schacht, P. Bienstman, and R. Baets, "Silicon-on-Insulator microring resonator for sensitive and label-free biosensing," Opt. Express **15**(12), 7610–7615 (2007). https://doi.org/10.1364/oe.15.007610

[18] K. De Vos, J. Girones, S. Popelka, E. Schacht, R. Baets, and P. Bienstman, "SOI optical microring resonator with poly(ethylene glycol) polymer brush for label-free biosensor applications," Biosens. Bioelectron. **24**(8), 2528–2533 (2009). https://doi.org/10.1016/j.bios.2009.01.009

[19] M. Iqbal, M. A. Gleeson, B. Spaugh, F. Taybor, W. G. Gunn, M. Hochberg, T. Baer-Jones, R. C. Bailey, and L. C. Gunn, "Label-free biosensor arrays based on silicon ring resonators and high-speed optical scanning instrumentation," IEEE J. Sel. Top. Quant. Electron. **16**(3), 654–661 (2010). https://doi.org/10.1109/jstqe.2009.2032510

[20] K. De Vos, "Label-free silicon photonics biosensor platform with microring resonators," Ph.D. dissertation (Univ. Gent, Gent, Belgium, 2010).

[21] D.-X. Xu, M. Vachon, A. Densmore, R. Ma, S. Janz, A. Delâge, J. Lapointe, P. Cheben, J. H. Schmid, E. Post, S. Messaoudène, and J.-M. Fédéli, "Real-time cancellation of temperature induced resonance shifts in SOI wire waveguide ring resonator label-free biosensor arrays," Opt. Express **18**(22), 22867–22879 (2010). https://doi.org/10.1364/oe.18.022867

[22] M. S. Luchansky and R. C. Bailey, "High-Q optical sensors for chemical and biological analysis," Anal. Chem. **84**(2), 793-821 (2012). https://doi.org/10.1021/ac2029024

[23] C. Ciminelli, C. M. Campanella, F. Dell'Olio, C. E. Campanella, and M. N. Armenise, "Label-free optical resonant sensors for biochemical applications," Prog. Quant. Electron. **37**(2), 51-107 (2013). https://doi.org/10.1016/j.pquantelec.2013.02.001

[24] H.-C. Ren, F. Vollmer, S. Arnold, and A. Libchaber, "High-Q microsphere biosensor – analysis for adsorption of rodlike bacteria," Opt. Express **15**(25), 17410-17423 (2007). https://doi.org/10.1364/oe.15.017410

[25] E. Kim, M. D. Baaske, and F. Vollmer, "Towards next-generation label-free biosensors: recent advances in whispering gallery mode sensors," Lab Chip **17**, 190-1205 (2017). https://doi.org/10.1039/c6lc01595f

[26] S. Wang, A. Ramachandran, and S.-J. Ja, "Integrated microring resonator biosensors for monitoring cell growth and detection of toxic chemicals in water," Biosens. Bioelectron. **24**(10), 3061-3066 (2009). https://doi.org/10.1016/j.bios.2009.03.027

[27] M. S. Luchansky, A. L. Washburn, T. A. Martin, M. Iqbal, L. C. Gunn, and R. C. Bailey, "Characterization of the evanescent field profile and bound mass sensitivity of a label-free silicon photonic microring resonator biosensing platform," Biosens. Bioelectron. **26**(4), 1283-1291 (2010). https://doi.org/10.1016/j.bios.2010.07.010

[28] J. Escorihuela, M. J. Bañuls, J. G. Castelló, V. Toccafondo, J. García-Rupérez, R. Puchades, and Á. Maquieira, "Chemical silicon surface modification and bioreceptor attachment to develop competitive integrated photonic biosensors," Anal. Bioanal. Chem. **404**(10), 2831-2840 (2012). https://doi.org/10.1007/s00216-012-6280-4

[29] R. C. Bailey, A. L. Washburn, A. J. Qavi, M. Iqbal, M. Gleeson, F. Taybor, and L. C. Gunn, "A robust silicon photonic platform for multiparameter biological analysis," Proc. SPIE 7220, Silicon Photonics IV, 72200N (2009). https://doi.org/10.1117/12.809819

[30] S. Mudumba, S. de Alba, R. Romero, C. Cherwien, A. Wu, J. Wang, M. A. Gleeson, M. Ibbal, and R. W. Burlingame, "Photonic ring resonance is a versatile platform for performing multiplex immunoassays in real time," J. Immunological Methods **448**, 34-43 (2017). http://dx.doi.org/10.1016/j.jim.2017.05.005

[31] "Genalyte." https://www.genalyte.com/

[32] M. S. McClellan, L. L. Domier, and R. C. Bailey, "Label-free virus detection using silicon photonic microring resonators," Biosens. Bioelectron. **31**(1), 388-392 (2012). https://doi.org/10.1016/j.bios.2011.10.056

[33] Genalyte, "Rapid Multiplex Biomarker Assay Platform - Maverick Detection System," Video, Published Feb. 12, 2013. https://www.youtube.com/watch?v=dn2whgucc5o

[34] E. Court, "How blood-testing startups are pitching themselves after the Theranos scandal," MarketWatch, via Genalyte, published June 25, 2018. https://www.genalyte.com/how-blood-testing-startups-are-pitching-themselves-after-the-theranos-scandal/

[35] A. Ramachandran, S. Wang, J. Clarke, S. J. Ja, D. Goad, L. Wald, E. M. Flood, E. Knobbe, J. V. Hryniewicz, S. T. Chu, D. Gill, W. Chen, O. King, and B. E. Little, "A universal biosensing platform based on optical micro-ring resonators," Biosens. Bioelectron. **23**(7), 939-944 (2008). https://doi.org/10.1016/j.bios.2007.09.007

[36] S. Janz, D.-X. Xu, M. Vachon, N. Sabourin, P. Cheben, H. McIntosh, H. Ding, S. Wang, J. H. Schmid, A. Delâge, J. Lapointe, A. Densmore, R. Ma, W. Sinclair, S.M. Logan, R. MacKenzie, Q.Y. Liu, D. Zhang, G. Lopinski, O. Mozenson, M. Gilmour, and H. Tabor, "Photonic wire biosensor microarray chip and instrumentation with application to serotyping of *Escherichia coli* isolates," Opt. Express, **21**(4), 4623-4637 (2013). https://doi.org/10.1364/oe.21.004623

[37] J. W. Chamberlain, "Biosensor Platform Development for Studying Carbohydrate-Mediated Bacterial Adhesion," Ph.D. dissertation (University of Washington, Seattle, WA, 2012).

[38] E. Thompson, "Label-Free Detection of *Escherichia coli* using Silicon Nanophotonic Biosensors," 2014 NNIN REU Research Accomplishments (2014). http://www.nnin.org/sites/default/files/2014_NNIN_REU_RA/2014nninREUra/2014NNINreuRA_Thompson.pdf

[39] D. J. Griffiths, *Introduction to Electrodynamics*. Upper Saddle River, NJ: Prentice Hall, 1999.

[40] L. Novotny and B. Hecht, *Principles of Nano-Optics*. Cambridge: Cambridge University Press, 2006.

[41] M. J. Deen and P. K. Basu, *Silicon Photonics: Fundamentals and Devices*. Chichester, UK: John Wiley & Sons, Ltd, 2012. https://doi.org/10.1002/9781119945161

[42] W. J. Westerveld, S. M. Leinders, K. W. A. van Dongen, H. P. Urbach, and M. Yousefi, "Extension of Marcatili's Analytical Approach for Rectangular Silicon Optical Waveguides," J. Light. Tech. 30(14), 2388-2401 (2012). https://doi.org/10.1109/jlt.2012.2199464

[43] J. D. Joannopoulos, S. G. Johnson, J. N. Winn, and R. D. Meade, *Photonic Crystals: Molding the Flow of Light*. Princeton, NJ: Princeton University Press, 2008. http://jdj.mit.edu/book/photonic-crystals-book.pdf

[44] COMSOL Multiphysics. https://www.comsol.com/

[45] I. N. Court and F. K. von Willisen, "Frustrated Total Internal Reflection and Application of Its Principle to Laser Cavity Design," Applied Optics **3**(6), 719-725 (1964). https://doi.org/10.1364/ao.3.000719

[46] Y. A. Vlasov and S. J. McNab, "Losses in single-mode silicon-on-insulator strip waveguides and bends," Opt. Express **12**(8), 1622-1631 (2004). https://doi.org/10.1364/opex.12.001622

[47] P. Dumon, G. Priem, L. Romeu Nunes, W. Bogaerts, D. Van Thourhout, P. Bienstman, T. K. Liang, M. Tsuchiya, P. Jaenen, S. Beckx, J. Wouters, and R. Baets, "Linear and Nonlinear Nanophotonic Devices Based on Silicon-on-Insulator Wire Waveguides," Jpn. J. Appl. Phys., **45**(8B), 6589-6602 (2006). https://doi.org/10.1143/jjap.45.6589

[48] T. Barwicz and H. A. Haus, "Three-Dimensional Analysis of Scattering Losses Due to Sidewall Roughness in Microphotonic Waveguides," J. of. Light. Tech., **23**(9), 2719-2732 (2005). https://doi.org/10.1109/jlt.2005.850816

[49] F. Grillot, L. Vivien, S. Laval, and E. Cassan, "Propagation Loss in Single-Mode Ultrasmall Square Silicon-on-Insulator Optical Waveguides," J. of Light. Tech. **24**(2), 891-896 (2006). https://doi.org/10.1109/jlt.2005.861939

[50] F. Grillot, L. Vivien, S. Laval, D. Pascal, and E. Cassan, "Size Influence on the Propagation Loss Induced by Sidewall Roughness in Ultrasmall SOI Waveguides," IEEE Phot. Tech. Lett., **16**(7), 1661-1663 (2004). https://doi.org/10.1109/lpt.2004.828497

[51] S. K. Selvaraja, W. Bogaerts, D. Van Thourhout, "Loss reduction in silicon nanophotonic waveguide micro-bends through etch profile improvement," Opti. Comm. 284, 2141–2144 (2011). https://doi.org/10.1016/j.optcom.2010.12.086

[52] D. Van Thourhout, W. Bogaerts, P. Dunon, "Submicron Silicon Strip Waveguides," in: L. Pavesi, G. Guillot (eds), *Optical Interconnects*. Springer, Berlin, Heidelberg. (2006). https://doi.org/10.1007/978-3-540-28912-8_8

[53] J. S. Orcutt, S. D. Tang, S. Kramer, K. Mehta, H. Li, V. Stojanović, and R. J. Ram, "Low-loss polysilicon waveguides fabricated in an emulated high-volume electronics process," Opt. Exp. **20**(7), 7243-7254 (2012). https://doi.org/10.1364/oe.20.007243

[54] Z. Sheng, D. Dai, S. He, "Comparative Study of Losses in Ultrasharp Silicon-on-Insulator Nanowire Bends," IEEE J. of Sel. Top. In Quant. Elec. **15**(5), 1406-1412 (2009). https://doi.org/10.1109/jstqe.2009.2013360

[55] K. Kakihara, N. Kono, K. Saitoh, and M. Koshiba, "Full-vectorial finite element method in a cylindrical coordinate system for loss analysis of photonic wire bends," Opt. Exp. **14**(23), 11128-11141 (2006). https://doi.org/10.1364/oe.14.011128

[56] C.-H. Tseng, C.-W. Tsai, K.-C. Lin, M.-C. Lee, and Y.-J. Chen, "Study of coupling loss on strongly-coupled, ultra compact microring resonators," Opt. Exp. **21**(6), 7250-7257 (2013). https://doi.org/10.1364/oe.21.007250

[57] D. Melati, A. Melloni, and F. Morichetti, "Real photonic waveguides: guiding light through imperfections," Adv. Opt. Photon. 6, 156-224 (2014). https://doi.org/10.1364/aop.6.000156

[58] M. Ostrowski, P. Pignalosa, H. Smith, and Y. Yi, "Higher-order optical resonance node detection of integrated disk microresonator," **36**(16), 3042-3044 (2011). https://doi.org/10.1364/ol.36.003042

[59] B. Koch, Y. Yi, J.-Y. Zhang, S. Znameroski, and T. Smith, "Reflection-mode sensing using optical microresonators," App. Phys. Lett. **95**(20), 201111 (2009). https://doi.org/10.1063/1.3263143

[60] M. L. Gorodetsky and A. D. Pryamikov, "Rayleigh scattering in high-Q microspheres," J. Opt. Soc. Am. B **17**(6), 1051-1057 (2000). https://doi.org/10.1364/josab.17.001051

[61] B. E. Little, S. T. Chu, H. A. Haus, "Second-order filtering and sensing with partially coupled traveling waves in a single resonator," Opt. Lett. **23**(20), 1570-1572 (1998). https://doi.org/10.1364/ol.23.001570

[62] A. Mazzei, S. Go¨tzinger, L. de S. Menezes, G. Zumofen, O. Benson,1, and V. Sandoghdar, "Controlled Coupling of Counterpropagating Whispering-Gallery Modes by a Single Rayleigh Scatterer: A Classical Problem in a Quantum Optical Light," Phys. Rev. Lett. **99**(17), 173603 (2007). https://doi.org/10.1103/physrevlett.99.173603

[63] F. Morichetti, "Roughness Induced Backscattering in Optical Silicon Waveguides," Phys. Rev. Lett. **104**(3), 33902 (2010). https://doi.org/10.1103/physrevlett.104.033902

[64] G. C. Ballesteros, J. Matres, J. Marti, and C. J. Oton, "Characterizing and modeling backscattering in silicon microring resonators," Opt. Exp. **19**(25), 24980-24985 (2011). https://doi.org/10.1364/oe.19.024980

[65] R. Mansoor, H. Sasse, S. Ison and A. Duffy, "Modelling of back reflection in optical ring resonators," 2014 International Conference on Numerical Electromagnetic Modeling and Optimization for RF, Microwave, and Terahertz Applications (NEMO), Pavia, 1-4 (2014). http://doi.org/10.1109/nemo.2014.6995681

[66] M. Moresco, M. Romagnoli, S. Boscolo, M. Midrio, M. Cherchi, E. S. Hosseini, D. Coolbaugh, M. R. Watts and B. Dutt, "Method for characterization of Si waveguide propagation loss," Opt. Exp. **21**(5), 5391-5400 (2013). https://doi.org/10.1364/oe.21.005391

[67] Z. Zhang, M. Dainese, L. Wosinski, and M. Qiu, "Resonance-splitting and enhanced notch depth in SOI ring resonators with mutual mode coupling," Opt. Exp. **16**(7), 4621-4630 (2008). https://doi.org/10.1364/oe.16.004621

[68] J. Matres and W. V. Sorin, "Simple model for ring resonators backscatter," Opt. Exp. **25**(4), 3242-3251 (2017). https://doi.org/10.1364/oe.25.003242

[69] A. Li and W. Bogaerts, "Fundamental suppression of backscattering in silicon microrings," Opt. Exp. **25**(3), 2092-2099 (2017). http://dx.doi.org/10.1364/oe.25.002092

[70] M. Á. Guillén-Torres, K. Murray, H. Yun, M. Caverley, E. Cretu, L. Chrostowski, and N. A. F. Jaeger, "Effects of backscattering in high-Q, large-area silicon-on-insulator ring resonators," Opt. Lett. 41, 1538-1541 (2016). https://doi.org/10.1364/ol.41.001538

[71] R. Mansoor, H. Sasse, S. Ison, and A. Duffy, "Crosstalk bandwidth of grating-assisted ring resonator add/drop filter," Opt Quant Electron. **47**(5), 1127-1137 (2015). https://doi.org/10.1007/s11082-014-9969-0

[72] A. Li, T. Van Vaerenbergh, P. De Heyn, P. Bientsman, W. Bogaerts, "Backscattering in silicon microring resonators: a quantitative analysis," Laser and Phot. Rev. **10**(3), 420-431 (2016). https://doi.org/10.1002/lpor.201500207

[73] S. Kedenburg, M. Vieweg, T. Gissibl, and H. Giessen, "Linear refractive index and absorption measurements of nonlinear optical liquids in the visible and near-infrared spectral region," Opt. Mat. Exp. **2**(11), 1588-1611 (2012). https://doi.org/10.1364/ome.2.001588

[74] G. M. Hale and M. R. Querry, "Optical constants of water in the 200-nm to 200-µm wavelength region," Appl. Opt. **12**(3), 555-563 (1973). https://doi.org/10.1364/ao.12.000555

[75] S. M. Grist, S. A. Schmidt, J. Flueckiger, V. Donzella, W. Shi, S. T. Fard, J. T. Kirk, D. M. Ratner, K. C. Cheung, and L. Chrostowski, "Silicon photonic micro-disk resonators for label-free biosensing," Opt. Express **21**(7), 7994-8006 (2013). https://doi.org/10.1364/oe.21.007994

[76] M. Suter and P. Dietiker, "Calculation of the finesse of an ideal Fabry-Perot resonator," Appl. Opt. **53**(30), 7004-7010 (2014). https://doi.org/10.1364/ao.53.007004

[77] M. Soltani, S. Yegnanarayanan, Q. Li, and A. Adibi, "Systematic engineering of waveguide-resonator coupling for silicon microring/microdisk/racetrack resonators: theory and experiment," IEEE J. Quant. Electron. **46**(8), 1158-1169 (2010). https://doi.org/10.1109/jqe.2010.2044633

[78] V. R. Dantham, S. Holler, C. Barbre, D. Keng, V. Kolchenko, and S. Arnold, "Label-free detection of single protein using a nanoplasmonic-photonic hybrid cavity," Nano Lett. **13**(7), 3347-3351 (2013). https://doi.org/10.1021/nl401633y

[79] J. Zhu, S. K. Ozdemir, Y.-F. Xiao, L. Li, L. He, D.-R. Chen, and L. Yang, "On-chip single nanoparticle detection and sizing by mode splitting in an ultrahigh-Q microresonator," Nat. Photonics **4**(1), 46-49 (2010). https://doi.org/10.1038/nphoton.2009.237

[80] I. M. White and X. Fan, "On the performance quantification of resonant refractive index sensors," Opt. Express **16**(2), 1020-1028 (2008). https://doi.org/10.1364/oe.16.001020

[81] C.-Y. Chao and L. J. Guo, "Design and optimization of microring resonators in biochemical sensing applications," J. Lightwave Technol. **24**(3), 1395-1402 (2006). https://doi.org/10.1109/jlt.2005.863333

[82] J. Hu, X Sun, A. Agarwal, and L. C. Kimerling, "Design guidelines for optical resonator biochemical sensors," J. Opt. Soc. Am. B, **26**(5), 1032-1041 (2009). https://doi.org/10.1364/josab.26.001032

[83] J. N. Anker, W. P. Hall, O. Lyandres, N. C. Shah, J. Zhao ,and R. P. Van Duyne, "Biosensing with plasmonic nanosensors," Nat. Mater. **7**, 442 - 453 (2008). https://doi.org/10.1038/nmat2162

[84] T. J. Kippenberg, S. M. Spillane, and K. J. Vahala, "Demonstration of ultra-high-Q small mode volume toroid microcavities on a chip," Appl. Phys. Lett. **85**(25), 6113-6115 (2004). https://doi.org/10.1063/1.1833556

[85] E. S. Hosseini, S. Y. Yegnanarayanan, A. H. Atabaki, M. Soltani, and A. Adibi, "High Quality Planar Silicon Nitride Microdisk Resonators for Integrated Photonics in the Visible Wavelength Range," Opt. Express, **17**(17), 2009. https://doi.org/10.1364/oe.17.014543

[86] A. E. Balaev, K. N. Dvoretski, V. A. Doubrovski, and V. V. Tuchin, "Determination of refractive index of rod-shaped bacteria from spectral extinction measurements," Proc. SPIE 5068, 375–380 (2003). http://doi.org/10.1117/12.518853

[87] A. Densmore, D.-X. Xu, P. Waldron, S. Janz, P. Cheben, J. Lapointe, A. Delâge, B. Lamontagne, J. H. Schmid, and E. Post, "A silicon-on-insulator photonic wire based evanescent field sensor," IEEE Photon. Technol. Lett. **18**(23), 2520–2522 (2006). https://doi.org/10.1109/lpt.2006.887374

[88] A. Arbabi and L. L. Goddard, "Measurements of the refractive indicies and thermos-optic coefficients of Si_3N_4 and SiO_x using microring resonances," Opt. Lett. **38**(19), 3878-3881 (2013). https://doi.org/10.1364/ol.38.003878

[89] B. J. Frey, D. B. Leviton, and T. J. Madison, "Temperature dependent refractive index of silicon and germanium," Proc. SPIE 6273, 62732J (2006). http://doi.org/10.1117/12.672850

[90] Y. H. Kim, S. J. Park, S.-W. Jeon, S. Ju, C.-S. Park, W.-T. Han, and B. H. Lee, "Thermo-optic coefficient measurement of liquids based on simultaneous temperature and refractive index sensing capability of a two-mode fiber interferometric probe," Opt. Express **20**(21), 23744-23754 (2012). https://doi.org/10.1364/oe.20.023744

[91] S. Schmidt, J. Flueckiger, W. X. Wu, S. M. Grist, S. T. Fard, V. Donzella, P. Khumwan, E. R. Thompson, Q. Wang, P. Kulik, X. Wang, A. Sherwali, J. Kirk, K. C. Cheung, L. Chrostowski, and D. Ratner, "Improving the performance of silicon photonic rings, disks, and Bragg gratings for use in label-free biosensing," Proc. SPIE 9166, 91660M (2014). https://doi.org/10.1117/12.2062389

[92] T. Reynolds, M. R. Henderson, A. Francois, N. Riesen, J. M. M. Hall, S. V. Afshar, S. J. Nicholls, and T. M. Monro, "Optimization of whispering gallery resonator design for biosensing applications," Opt. Exp. **23**(13), 17067-17076 (2015). https://doi.org/10.1364/oe.23.017067

[93] A. B. Dahlin, "Size Matters: Problems and Advantages Associated with Highly Miniaturized Sensors," Sensors **12**(3), 3018-3036 (2012). https://doi.org/10.3390/s120303018

[94] H. H. Li, "Refractive index of silicon and germanium and its wavelength and temperature derivatives," J. Phys. Chem. Ref. Data, **9**(3), 561-658 (1980). https://doi.org/10.1063/1.555624

[95] T. Bååk, "Silicon oxynitride; a material for GRIN optics," Appl. Opt. **21**(6), 1069-1072 (1982). https://doi.org/10.1364/ao.21.001069

[96] I. H. Malitson, "Interspecimen comparison of the refractive index of fused silica," J. Opt. Soc. Am. **55**(10), 1205-1209 (1965). https://doi.org/10.1364/josa.55.001205

[97] Y. Coello, B. Xu, T. L. Miller, V. V. Lozovoy, and M. Dantus, "Group-velocity dispersion measurements of water, seawater, and ocular components using multiphoton intrapulse interference phase scan," Appl. Opt. **46**(35), 8394-8401 (2007). https://doi.org/10.1364/ao.46.008394

[98] W. C. Tan, K. Koughia, J. Singh, and S. O. Kasap, "Fundamental optical properties of materials I," in *Optical Properties of Condensed Matter and Applications*, J. Singh, ed. (John Wiley & Sons Ltd, Hoboken, NJ, 2006). https://doi.org/10.1002/0470021942.ch1

[99] M. Morita, T. Ohmi, E. Hasegawa, M. Kawakami, and M. Ohwada, "Growth of native oxide on a silicon surface," J. Appl. Phys. **68**(3), 1272-1281 (1990). https://doi.org/10.1063/1.347181

[100] G. Reshes, S. Vanounou, I. Fishov, and M. Feingold, "Cell Shape Dynamics in *Escherichia coli*," Biophys. Journ. **94**, 251-264 (2008). https://doi.org/10.1529/biophysj.107.104398

[101] B. Volkmer and M. Heinemann, "Condition-Dependent Cell Volume and Concentration of *Escherichia coli* to Facilitate Data Conversion for Systems Biology Modeling," PLos ONE **6**(7), e23126 (2011). https://doi.org/10.1371/journal.pone.0023126

[102] A. I. Konokhova, A. A. Gelash, M. A. Yurkin, A. V. Chernyshev, and V. P. Maltsev, "High-Precision Characterization of Individual *E. coli* Morphology by Scanning Flow Cytometry," Cytometry Part A **83A**(6), 568-575 (2013). https://doi.org/10.1002/cyto.a.22294

[103] A. C. S. Yu, J. F. C. Loo, S. Yu, S. K. Kong, T.-F. Chan, "Monitoring bacterial growth using tunable resistive pulse sensing with a pore-based technique," Appl. Microbiol. Biotechnol. **98**(2), 855-862 (2014). https://doi.org/10.1007/s00253-013-5377-9

[104] G. M. Cooper and R. E. Hausmann, *The Cell: A Molecular Approach, 2nd Ed.* (Sinauer Associates, 2000).

[105] V. R. Stull, "Size Distribution of Bacterial Cells," Journ. Of Bacteriology **109**(3), 1301-1301 (1972). https://www.ncbi.nlm.nih.gov/pmc/articles/pmc247356/

[106] J. Wesolowski, V. Alzogaray, J. Reyelt, M. Unger, K. Juarez, M. Urrutia, A. Cauerhff, W. Danquah, B. Rissiek, F. Scheuplein, N. Schwarz, S. Adriouch, O. Boyer, M. Seman, A. Licea, D. V. Serreze, F. A. Goldbaum, F. Haag, and F. Koch-Noite, "Single domain antibodies: promising experimental and therapeutic tools in infection and immunity," Med. Microbio. Immunol. **198**(3), 157-174 (2009). https://doi.org/10.1007/s00430-009-0116-7

[107] D. Saerens, L. Huang, K. Bonroy, and S. Muyldermans, "Antibody Fragments as Probe in Biosensor Development," Sensors **8**(8), 4669-4686 (2008). https://doi.org/10.3390/s8084669

[108] A. J. Haes, S. Zou, G. C. Schatz, and R. P. Van Duyne, "A Nanoscale Optical Biosensor: The Long Range Distance Dependence of the Localized Surface Plasmon Resonance of Noble Metal Nanoparticles," J. Phys. Chem. B **108**(1), 109-116 (2004). https://doi.org/10.1021/jp0361327

[109] S. Arnold, R. Ramjit, D. Keng, V. Kolchenki, and I. Teraoka, "MicroParticle photophysics illuminates viral bio-sensing," Faraday Discuss. **137**, 65-83 (2008). https://doi.org/10.1039/b702920a

[110] H. Elsner, and H. G. Meyer, "Nanometer and high aspect ratio patterning by electron beam lithography using a simple DUV negative tone resist," Microelectron. Eng. **57/58**, 291-296 (2001). https://doi.org/10.1016/s0167-9317(01)00498-1

[111] Micro Resist Technology, "Processing guidelines – Negative Tone Photoresist Series ma-N 2400". http://www.microresist.de

[112] G. Ren, S. Chen, Y. Cheng, and Y. Zhai, "Study on inverse taper based mode transformer for low loss coupling between silicon wire waveguide and lensed fiber," Opt. Comm. **284**(19), 4782-4788 (2014). https://doi.org/10.1016/j.optcom.2011.05.072

[113] Justin C. Wirth, "Silicon grating couplers for low loss coupling between optical fiber and silicon nanowires," Master's Thesis, Purdue University (2011). https://docs.lib.purdue.edu/dissertations/aai1510029/

[114] OZ Optics, "Single Mode Tapered/Lensed Fibers". http://shop.ozoptics.com/single-mode-taperedlensed-fibers

[115] H. Jansen, H. Gardeniers, M. de Boer, M. Elwenskoek, and J. Fluitman, "A survey on the reactive ion etching of silicon in microtechnology," J. Micromech. Microeng. **6**(1), 14-28 (1996). https://doi.org/10.1088/0960-1317/6/1/002

[116] C.-C. Hsu, N. Marchack, R. M. Martin, C. Pham, J. Joang, and J. P. Chang, "Feature profile evolution during shallow trench isolation etching in chlorine-based plasmas. III. The effect of oxygen addition," J. Vac. Sci. Technol. B **31**(4), 042201 (2013). https://doi.org/10.1116/1.4810908

[117] D. Taillaert, F. Van Laere, M. Ayre, W. Bogaerts, D. Van Thourhout, P. Bienstman, and R. Baets, "Grating Couplers for Coupling between Optical Fibers and Nanophotonic Waveguides," J. J. App. Phys **45**(8A), 6071-6077 (2006). https://doi.org/10.1143/jjap.45.6071

[118] Y. Wang, H. Yun, Z. Lu, R. Bojko, W. Shi, X. Wang, J. Flueckiger, F. Zhang, M. Caverley, N. A. F. Jaeger, and L. Chrostowski, "Apodized Focusing Fully Etched Subwavelength Grating Couplers," IEEE Phot. Journ. **7**(3), 2400110 (2015). https://doi.org/10.1109/jphot.2015.2426879

[119] D. Yang, H. Tian, Y. Ji, and Q. Quan, "Design of simultaneous high-Q and high-sensitivity photonic crystal refractive index sensors," J. Opt. Soc. Am. B **30**(8), 2027-2031 (2013). https://doi.org/10.1364/josab.30.002027

[120] E. S. Hosseini, "High quality integrated silicon nitride nanophotonic structures for visible light applications," Ph.D. dissertation (Georgia Inst. Of Tech., Atlanta, GA, 2011).

[121] MicroChemicals GmbH, "Surface Cleaning Adhesion Promotion" http://www.microchemicals.com/downloads/application_notes.html

[122] K. W. Kolasinski, "Photochemical and nonthermal chemical modification of porous silicon for biomedical applications," in *Porous Silicon for Biomedical Applications*, H. A. Santos, ed. (Elsiver, 2014). https://doi.org/10.1533/9780857097156.1.52

[123] H. Angermann, "Conditioning of Si-interfaces by wet-chemical oxidation: Electronicinterface properties study by surface photovoltage measurements," Appl. Surf. Sci. **312**, 3-16 (2014). https://doi.org/10.1016/j.apsusc.2014.05.087

[124] X. Xi, J. Shi, S. MaghsoudyLouyeh, and B. R. Tittmann, "Characterization of silicon wafer surfaces after hydrophilic and hydrophobic treatments by atomic force microscopy," AIP Conference Proceedings **1211**, 1493 (2010). https://doi.org/10.1063/1.3362245

[125] MicroChemicals GmbH, "Baking Steps in Photoresist Processing". http://www.microchemicals.com/downloads/application_notes.html

[126] MicroChemicals GmbH, "Resists, Developers and Removers". http://www.microchemicals.com/downloads/application_notes.html

[127] L.-W. Luo, G. S. Wiederhecker, J. Cardenas, C. Poitras, and M. Lipson, "High quality factor etchless silicon photonic ring resonators," Opt. Express **19**(7) 6284-6289 (2011). https://doi.org/10.1364/oe.19.006284

[128] T. Baehr-Jones, M. Hochberg, C. Walker, E. Chan, D. Koshinz, W. Krug, and A. Scherer "Analysis of the Tuning Sensitivity of Silicon-on-Insulator Optical Ring Resonators," J. of Light. Tech. **23**(12), 4215-4221 (2005). https://doi.org/10.1109/jlt.2005.853147

[129] K. Padmaraju and K. Bergman "Resolving the thermal challenges for silicon microring resonator devices," Nanophotonics **3**(4-5), 269-281 (2013). https://doi.org/10.1515/nanoph-2013-0013

[130] P. Dong, "Silicon Photonic Integrated Circuits for Wavelength-Division Multiplexing Applications," IEEE J. of Sel. Top. in Quant. Elec. **22**(6), 370-378 (2016). https://doi.org/10.1109/jstqe.2016.2575358

[131] D. Bachman, Z. Chen, R. Fedosejevs, Y. Y. Tsui, and V. Van, "Permanent fine tuning of silicon microring devices by femtosecond laser surface amorphization and ablation," Opt. Express 21(9), 11048-11056 (2013). https://doi.org/10.1364/oe.21.011048

[132] F. Wu and C. Dekker, "Nanofabricated structures and microfluidic devices for bacteria: from techniques to biology," Chem. Soc. Rev. **45**(2), 268-280 (2016). https://doi.org/10.1039/c5cs00514k

[133] L. E. Eland, A. Wipat, S. Lee, S. Park, and L. J. Wu, "Chapter 3 – Microfluidics for bacterial imaging," Methods in Microbiology **43**, 69-111 (2016). https://doi.org/10.1016/bs.mim.2016.10.002

[134] X. Wang, X. Guan, Q. Huang, J. Zheng, Y. Shi, and D. Dai, "Suspended ultra-small disk resonator on silicon for optical sensing," Opt. Lett. **38**(24), 5405. (2013). https://doi.org/10.1364/ol.38.005405

[135] W. C. Jiang, J. Zhang, and Q. Lin, "Compact suspended silicon microring resonators with ultrahigh quality," Opt. Exp. **22**(1), 1187-1192 (2014). https://doi.org/10.1364/oe.22.001187

[136] S. Groblacher, K. Hammerer, M. R. Vanner, and M. Aspelmeyer, "Observation of strong coupling between a micromechanical resonator and an optical cavity field," Nat. **460**, 724-727 (2009). https://doi.org/10.1038/nature08171

[137] M. Stocker and R. Stocker, "Microorganisms in vortices: a microfluidic setup," Limnol. Oceanogr.: Methods **4**(10), 392-398 (2006). https://doi.org/10.4319/lom.2006.4.392

[138] J. Mannik, R. Driessen, P. Galajda, J. E. Keymer, and C. Dekker, "Bacterial growth and motility in sub-micron constrictions," Proc. Natl. Acad. Sci. USA **106**(35), 14861-14866 (2009). https://doi.org/10.1073/pnas.0907542106

[139] Y. Wang, X. Wang, J Flueckiger, H. Yun, W. Shi, R. Bojko, N. A. F. Jaeger, and L. Chrostowski, "Focusing sub-wavelength grating couplers with low back reflections for rapid prototyping of silicon photonic circuits," Opt. Exp. **22**(17), 20652-20662 (2014). https://doi.org/10.1364/oe.22.020652

[140] J. C. Wirth, "Birck Nanotechnology Center Wiki". https://wiki.itap.purdue.edu/display/bncwiki

[141] Thermo Fisher Scientific, "Intrivogen One Shot TOP10 Chemically Competent *E. coli*, Catalog number: C404010" https://www.thermofisher.com/order/catalog/product/c404010

[142] T. Durfee, R. Nelson, S. Baldwin, G. Plunkett III, V. Burland, B. Mau, J. F. Petrosino, X. Qin, D. M. Muzny, M. Ayele, R. A. Gibbs, B. Csorgo, G. Posfai, G. M. Weinstock, and F. R. Blattner, "The Complete Genome Sequence of *Escherichia coli* DH10B: Insights into the Biology of a Laboratory Workhouse," J. Bacteriology **190**(7), 2597-2606 (2008). https://doi.org/10.1128/jb.01695-07

[143] D. Rafizadeh, J. P. Zhang, R. C. Tiberio, and S. T. Ho, "Propagation Loss Measurements in Semiconductor Microcavity Ring and Disk Resonators," J. Lightwave Technol. **16**(7), 1308-1314 (1998). https://doi.org/10.1109/50.701410

[144] W. D. Sacher, W. M. J. Green, S. Assefa, T. Barwicz, H. Pan, S. M. Shank, Y. A. Vlasov, and J. K. S. Poon, "Coupling modulation of microrings at rates beyond the linewidth limit," Opt. Express **21**(8), 9722-9733 (2013). https://doi.org/10.1364/oe.21.009722

[145] G. J. Triggs, G. J. O. Evans, and T. F. Krauss, "Degradation of silicon photonic biosensors in cell culture media: analysis and prevention," Biomed. Opt. Exp. **8**(6), 2924-2931 (2017). https://doi.org/10.1364/boe.8.002924

[146] Y.-C. Kim, "Diffusivity of Bacteria", Korean J. of Chem. Eng., 13(3), 282-287 (1996). https://doi.org/10.1007/bf02705951

[147] K. Han, S. Kim, J. Wirth, M. Teng, Y. Xuan, B. Niu, and M. Qi, "Strip-slot direct mode coupler," Opt. Express **24**(6), 6532-6541 (2016). https://doi.org/10.1364/oe.24.006532

[148] J. Flueckiger, S. Schmidt, V. Donzella, A. Sherwali, D. M. Ratner, L. Chrostowski, and K. C. Cheung, "Sub-wavelength grating for enhanced ring resonator biosensor," Opt. Express **24**(14), 15672-15686 (2016). https://doi.org/10.1364/oe.24.015672

PUBLICATIONS

Journal Articles

1) **Justin C. Wirth**, Brett R. Wenner, Monica S. Allen, Jeffery W. Allen, Kyunghun Han, Ben Niu, Yi Xuan, and Minghao Qi, "Optimizing microring resonators for single cell resolution label-free whole bacteria sensing," (The work contained herein, to be submitted).

2) Saman Jahani, Sangsik Kim, Jonathan Atkinson, **Justin C. Wirth**, Farid Kalhor, Abdullah Al Noman, Ward D. Newman, Prashant Shekhar, Kyunghun Han, Vien Van, Raymond G. Decorby, Lukas Chrostowski, Minghao Qi, and Zubin Jacob, "Controlling evanescent waves using silicon photonic all-dielectric metamaterials for dense integration," Nat. Communications **9**, 1893 (2018). https://doi.org/10.1038/s41467-018-04276-8

3) Kyunghun Han, Sangsik Kim, **Justin C Wirth**, Min Teng, Yi Xuan, Ben Niu, and Minghao Qi, "Strip-slot direct mode coupler," Opt. Express **24**(6), 6532-6541 (2016). https://doi.org/10.1364/oe.24.006532

4) Jian Wang, **Justin C. Wirth**, Yi Xuan, Daniel E. Leaird, Andrew M. Weiner, and Minghao Qi, "Far-field polarization characterization of the fundamental modes of a strip silicon waveguide," Opt. Lett. **38**, 4785-4788 (2013). https://doi.org/10.1364/ol.38.004785

5) Hao Shen, Li Fan, Jian Wang, **Justin C. Wirth**, and Minghao Qi, "A Taper to Reduce the Straight-to-Bend Transition Loss in Compact Silicon Waveguides" IEEE Photonics Technology Letters **22**(15), pp. 1174-1176 (2010). https://doi.org/10.1109/lpt.2010.2050681

Conference Proceedings

6) Sangsik Kim, Saman Jahani, Jonathan Atkinson, **Justin C. Wirth**, Farid Kalhor, Abdullah Al Noman, Ward D. Newman, Prashant Shekhar, Kyunghun Han, Vein Van, Raymond G. Decorby, Lukas Chrostowski, Minghao Qi, and Zubin Jacob, "High-Density Photonic Chip with All-Dielectric Metamaterials," *Conference on Lasers and Electro-Optics 2018*, paper STh4A.1 (2018). https://doi.org/10.1364/cleo_si.2018.sth4a.1

7) **Justin C. Wirth**, Brett R. Wenner, Monica S. Allen, Jeffery W. Allen, and Minghao Qi, "Design and Optimization of Microring Resonators for Label-free Cellular Biosensing and Integrated Photonic Lab-on-Chip Applications," accepted for presentation at *Government Microcircuit Applications & Critical Technology Conference (GOMACtech)* (2014).

8) Minghao Qi, Leo T. Varghese, Jian Wang, Li Fan, Yi Xuan, Ben Niu, Chookiat Tansarawiput, **Justin C. Wirth**, Andrew M. Weiner, Fuwan Gan, and Xi Wang, "Optical Diodes and Transistors on a Silicon Chip," *Conference on Lasers and Electro-Optics 2013*, paper QF1D.1 (2013). https://doi.org/10.1364/cleo_qels.2013.qf1d.1

9) Jian Wang, **Justin C. Wirth**, Yi Xuan, Daniel E. Leaird, Andrew M. Weiner, and Minghao Qi, "Characterization of the Fundamental Polarization Modes of a Silicon Waveguide in the Far Field," *Conference on Lasers and Electro-Optics 2013*, paper JTu4A.54 (2013). https://doi.org/10.1364/cleo_at.2013.jtu4a.54

10) **Justin C. Wirth**, Brett R. Wenner, Monica S. Allen, Jeffery W. Allen, and Minghao Qi, "A computational approach to optimize microring resonators for biosensing applications", *Proc. SPIE* 8570, paper 857001 (2013). https://doi.org/10.1117/12.2001820

11) Jian Wang, Li Fan, Leo T. Varghese, Fuwan Gan, Xi Wang, **Justin C. Wirth**, Ben Niu, Yi Xuan, Daniel E. Leaird, and Andrew M. Weiner, "Nonreciprocal transmission of 10 Gbps OOK data through an all-silicon passive optical diode," *IEEE Photonics Conference 2012*, pp. 703-704 (2012). https://doi.org/10.1109/ipcon.2012.6358816

12) Leo T. Varghese, Li Fan, Jian Wang, Fuwan Gan, Xi Wang, **Justin C. Wirth**, Ben Niu, Chookiat Tansarawiput, Yi Xuan, and Andrew M. Weiner, "A Silicon Optical Transistor," *Frontiers in Optics 2012*, paper FW6C.6 (2012). https://doi.org/10.1364/fio.2012.fw6c.6

13) Li Fan, Jian Wang, Leo T. Varghese, **Justin C. Wirth**, Ben Niu, Yi Xuan, Andrew M. Weiner, and Minghao Qi, "40 dB Optical Nonreciprocal Transmission on a Silicon Chip," *Frontiers in Optics 2012*, paper FTu1A.3 (2012). https://doi.org/10.1364/fio.2012.ftu1a.3

14) **Justin C. Wirth**, Jian Wang, Ben Niu, Yi Xuan, Li Fan, Leo T. Varghese, Daniel E. Leaird, and Andrew M. Weiner, "Efficient Silicon-on-Insulator Polarization Rotator based on Mode Evolution," *Conference on Lasers and Electro-Optics 2012*, paper JW4A.83 (2012). https://doi.org/10.1364/cleo_at.2012.jw4a.83

Master's Thesis

15) **Justin C. Wirth**, "Silicon grating couplers for low loss coupling between optical fiber and silicon nanowires," Master's Thesis, Purdue University (2011). https://docs.lib.purdue.edu/dissertations/aai1510029/

Patents

16) Min Teng, Minghao Qi, Ben Niu, **Justin Christopher Wirth**, Sangsik Kim, Kyunghun Han, Yi Xuan, Yun Jo Lee, "Optical Coupler," U.S. patent 10,197,731 (Feb. 5, 2019).